



Fiber Optical Tweezers for Brain Property Measurements

A Major Qualifying Project Report:

Submitted to the Faculty of

WORCESTER POLYTECHNIC INSTITUTE

in partial fulfillment of the requirements for the

Degree of Bachelor of Science

in Mechanical Engineering

By:

Li-Yang Chiang

Matthew DeBenedictis

Qindong Zhang

April 25, 2019

Professor Yuxiang Liu, Advisor

Abstract

Traumatic brain injury (TBI) affects nearly ten million people globally per year and is largely linked to sporting accidents. Knowing mechanical properties of brain tissues is imperative to diagnosis and prevention of TBIs. Yet, past and current methods yield a wide spectrum of brain tissue stiffness measurements with no clear convergence. Fiber optical tweezers (FOTs) have the potential to bridge this gap. Optical tweezers (OTs) are a Nobel-Prize-winning technique routinely used in various biomechanics studies, but have not been used for brain measurements due to its bulky size. As the next generation of OTs, the FOTs are small, modular tools capable of trapping microspheres via laser illumination, allowing for mechanical interrogation of the local medium. The team fabricated the FOTs to realize brain white matter stiffness measurements, which are comparable to those seen in literature. This work can find potential applications in understanding TBI and designing sports equipment.

Executive Summary

In this year-long research project, the team worked in the Optomechanics Laboratory at Worcester Polytechnic Institute to investigate the application of fiber optical tweezers as a tool to measure mechanical properties of biological samples. Previous research has shown that Traumatic Brain Injuries (TBIs) is one of the most common injuries in the United States with 1.5 million patients yearly and more than 5.3 million disabled patients. However, properties of brain tissues have not been investigated as comprehensively as other parts of the body. Numerous experiments have measured the brain mechanical properties with wide divergence. Hence, a new tool is needed to offer another perspective to address this issue.

In order to tackle the current problems of data divergence, the team investigated the possibility of a novel application using fiber optical tweezers (FOTs) to measure mechanical properties on brain samples. The goal of the MQP was to design a Modular Fiber Optical Tweezers (MFOTs) system that is portable and can robustly trap microspheres, allowing for calibration of brain mechanical properties. The MFOTs generate 3-dimensional optical traps using similar trapping principles to traditional objective-lens-based optical tweezers.

The fundamentals of optical trapping have been studied because the experiments depend on robust traps to get meaningful calibration measurements of mechanical stiffness. The power spectrum analysis method for optical tweezer calibration and data collection using various computer programs was carried out to characterize the optical trap generated by the optical tweezers. The programs processed the power spectrum data and fit them to a Lorentzian fitting, providing integral information about the optical trap. The governing equations for the optical trap describe the Brownian motion of the microspheres and the stiffness of the medium.

As the team refined the design and manufacturing procedures of the MFOTs, a MFOTs fabrication guide was developed for future lab users. After fabrication, the team first trapped 15.45 micron silica beads to collect datasets in water as medium to verify the reliable performance of the MFOTs. These trials were done under an inverted microscope setup. When designing the experimental setup for trapping in brain sample, an upright microscope configuration was utilized to address lighting issue with the brain sample.

The team collected data from well over a hundred brain experiments. The data we collected was on the same magnitude to those in published literature, proving the accuracy of our MFOTs. This was a milestone for the project because this was the first time the mechanical properties of brain samples were measured using the fiber optical tweezers. This project extends the horizon on potential applications of the MFOTs in the field of biomedical engineering and expands the fundamental understanding of brain mechanical properties.

The team suggests more data should be gathered through experimentation and compared in order to prove the repeatability of the MFOTs. In terms of potential modifications to the setup that could yield more accuracy, using a better objective lens with higher working distance and magnification should be considered. The team also recommends that future efforts should experiment with using tapered fiber tips in the MFOTs to provide stronger optical trapping capabilities. Lastly, thermal effects caused by microscope illumination and laser from fiber tips should be considered in obtaining more accurate results that do not have influence from thermal loads. That being said, since this is the first time fiber optical tweezers have calibrated mechanical stiffness of brain tissue, using the tool for this sort of application has been confirmed.

Table of Contents

Abstract.....	i
Executive Summary	ii
Table of Contents	iv
Table of Figures.....	viii
Table of Tables	x
Table of Equations	xi
<i>1.0 Background</i>	1
<i>1.1 Brain Mechanical Properties</i>	2
<i>1.1.1 Existing Knowledge of Brain Properties</i>	3
<i>1.1.2 Methods for Brain Property Measurement</i>	5
<i>1.1.3 Challenges of Existing Brain Measurements and the Need of New Tools</i>	9
<i>1.2 Optical Tweezers (OTs)</i>	11
<i>1.2.1 Optical Trapping</i>	12
<i>1.2.2 Traditional (Objective-based) Optical Tweezers</i>	13
<i>1.2.3 Limitations of Objective-lens-based Optical Tweezers</i>	16
<i>1.3 Fiber Optical Tweezers</i>	17
<i>1.3.1 Optical Fibers</i>	17
<i>1.3.2 Working Principles of Optical Fiber Light Transmission</i>	19
<i>1.3.3 Applications of Optical Fibers</i>	20
<i>1.3.4 Optical Fiber Tweezers</i>	27
<i>1.3.5 Limitations of Optical Fiber Tweezers</i>	30
<i>1.4 Motivation</i>	31
<i>1.5 Summary</i>	32
Chapter 2. Design and Fabrication of Modular Fiber Optical Tweezers	33

<i>2.1 Design of Modular Fiber Optical Tweezers</i>	33
<i>2.2 Optimization of the Existing Fabrication Method of Modular Fiber Optical Tweezers</i> .	34
<i>2.2.1 Clamping Mechanisms for Fiber Tubes</i>	35
<i>2.2.2 Rotational Stage</i>	36
<i>2.2.3 Adhesive for Fiber Tubes</i>	37
<i>2.2.4 Common Board Design</i>	38
<i>2.3 Experimental Setup of Modular Fiber Optical Tweezers</i>	40
<i>2.4 Brain Experimental Setup and Working Principles</i>	41
<i>2.4.1 Microscope Module</i>	42
<i>2.4.2 Optical Tweezer Module</i>	44
<i>2.4.3 Sample Platform</i>	44
<i>2.4.4 Assembly</i>	46
Chapter 3. Optical Trapping Experiments: Fundamentals, Procedure, and Data Analysis	48
<i>3.1 Governing Equations of Power Spectrum Analysis</i>	48
<i>3.2 Elastic and Shear Moduli Calculation</i>	50
<i>3.3 Data Processing</i>	51
<i>3.4 Brain Sample Preparation</i>	52
<i>3.5 Summary</i>	52
Chapter 4. Results and Discussion	54
<i>4.1 Criteria to Determine Good Trapping Experiments and Faithfulness of Measured Data</i>	54
<i>4.2 Experimental Results of Polystyrene Bead Trapping in Water</i>	58
<i>4.2.1 Meaningful Results from Water Experiments</i>	58
<i>4.2.2 Discussion</i>	61
<i>4.3 Results Obtained from the White Matter in Brain Sample Experiments</i>	65

4.3.1 <i>Type I Results from Beads-in-Water Experiments</i>	65
4.3.2 <i>Type II Results from Beads-on-Brain Experiment</i>	67
4.4 <i>Comparison of Elastic and Shear Moduli Results Obtained by this Work to Published Results</i>	70
4.4.1 <i>Elastic Modulus Measurements in this Work</i>	71
4.4.2 <i>Comparison to Published Work and Discussion</i>	72
4.4.3 <i>Shear Modulus Measurements in this Work</i>	74
4.4.4 <i>Comparison to Published Work and Discussion</i>	74
4.5 <i>Conclusions</i>	76
Chapter 5. System Limitations and Future Development	77
5.1 <i>Location of the Sample and its Preparation</i>	77
5.2 <i>Impaired Vision during Experimentation</i>	79
5.3 <i>Limitations of the Polystyrene Beads</i>	81
5.4 <i>Thermal Effects on Brain Mechanical Properties during Measurement</i>	83
5.4.1 <i>Sample Thermo-deformation</i>	83
5.4.2 <i>Sample Moisture Loss</i>	84
5.4.3 <i>Evaporation of Bead Solution</i>	85
5.4.4 <i>Thermal Effects Summary</i>	86
Chapter 6. Conclusion	88
Acknowledgments	90
References	91
Appendix A: Protocol for MFOTs Fabrication	103
I. <i>Fiber end face processing</i>	103
II. <i>Installation of prepared fibers onto the alignment system</i>	106
III. <i>Fiber and light spot alignment to enable the optical trap</i>	109

IV. Modular system assembly - transition and fixation of the aligned fibers onto a common board	116
Appendix B: Brain Experimental Procedure	121
I. Setting up the System	121
II. Applying the Bead Solution	122
III. Alignment of the Bead on the Brain Surface, the MFOTs, and the Objective Lens	123
IV. Calibrating the Mechanical Stiffness of the Brain Sample	127

Table of Figures

Figure 1-1: Shear Stress Distribution with Different G Values [10].	3
Figure 1-2: Operation of the MRE Experiment for Measuring the Brain Properties [8].	9
Figure 1-3: Fifty Years of Brain Mechanical Stiffness Measurements [21].	10
Figure 1-4: Schematic of Traditional Objective-lens-based Optical Tweezers [41].	14
Figure 1-5: Multimode (A) and Singlemode (B) Fiber Cross-Section [60].	18
Figure 1-6: Classifications of Optical Fibers and Their Characteristics [66].	19
Figure 1-7: Illustration of Total Internal Reflection [68].	20
Figure 1-8: Block Diagram of CH ₄ Monitoring Fiber Optical Sensor [82].	24
Figure 1-9: FBG Aircraft Deformation Monitoring System Schematic [83].	25
Figure 1-10: Intensity-based Optical Fiber Pressure Sensor [89].	26
Figure 1-11: Operation of Fabry-Pérot Pressure Sensor [92].	27
Figure 1-12: Dual-fiber optical tweezers with gradient and scattering force vectors [27].	28
Figure 2-1: Schematic of view from above of DFOTs (left) compared to MFOTs (right).	34
Figure 2-2: Tape holding the fiber tubes.	35
Figure 2-3: V-groove clamp to hold fiber tube.	36
Figure 2-4: Rotational stage on the common board fixation module.	37
Figure 2-5: Fiber tips with creep (left) and without creep (right).	38
Figure 2-6: Schematic of Experimental Set-up of MFOTs [51].	41
Figure 2-7: Microscope configuration A (left), configuration B (right).	42
Figure 2-8: Complete Sample Platform Setup.	45
Figure 2-9: Old system with limited vertical travel range (A); New acrylic adapter piece allows greater vertical travel range (B).	46
Figure 4-1: A) Lorentzian-fitted experimental data with outlier; B) Lorentzian-fitted experimental data with outlier removed.	57
Figure 4-2: Excessive noise in the cropped data.	58
Figure 4-3: Spring constant dependency graph with trendline going through the origin.	61
Figure 4-4: Effects of trapping fiber separation on coupled, reflected light. (Red arrows indicate uncoupled, reflected light; orange arrows indicate coupled, reflected light; the dotted line indicates reference height; the beige rectangular object indicates part).	63

Figure 4-5: A) Dr. Chaoyang Ti's Lorentzian fitting for trapping a 15.45 micron diameter polystyrene bead in deionized water. B) Spring constant calibration as a function of power per fiber for lensed and cleaver fiber MFOTs [51].	64
Figure 4-6: Vision of brain blocked by trapping fiber tips.	67
Figure 4-7: Secondary roll-off point at higher frequency.	68
Figure 5-1: Bovine brain sample as received.	78
Figure 5-2: Brain samples after being cut (A); brain sample in appropriate dimension (B)	79
Figure 5-3: Localized heating during the experiment.	85
Figure 5-4: Moist brain sample before experiment (left); Surface-dehydrated brain sample after experiment (right).	87
Figure B-1: Brain Experiment Experimental Setup.	122
Figure B-2: Beads in the Brain Surface.	123
Figure B-3: Light Shining on the Bead that is in the Brain Surface.	126

Table of Tables

Table 1-1: Brain Properties Comparison from Two Studies.	4
Table 1-2: Average shear moduli of various regions of porcine brain using the indentation method [16].....	6
Table 1-3: Moduli of gray and white matter of brain tissue using the indentation method [17]....	7
Table 1-4: Purpose of Components of Traditional Optical Tweezers.	14
Table 2-1: Comparison between the old and the new common board.....	39
Table 4-1: Results of experiments #1 & #2 in deionized water.....	59
Table 4-2: Comparison to known results.....	64
Table 4-3: Brain sample experiments - 1.....	65
Table 4-4: Corner frequency and spring constant results from Type I data.	66
Table 4-5: Brain sample experiments -2.....	68
Table 4-6: Corner frequency and spring constant results from Type II data.	70
Table 4-7: Elastic modulus of white matter using MFOTs method for experiments 4-6.	72
Table 4-8: Moduli of white matter of brain tissue using the indentation method [17].....	72
Table 4-9: Shear modulus of white matter using MFOTs method from experiments 4-6.....	74
Table 4-10: Average shear moduli of various regions of porcine brain using indentation method [16].....	75

Table of Equations

Equation 1-1 4
Equation 3-1 48
Equation 3-2..... 49
Equation 3-3..... 49
Equation 3-4..... 49
Equation 3-5..... 50
Equation 3-6..... 50
Equation 3-7 50
Equation 3-8..... 51
Equation 4-1 71

Chapter 1. Overview

The mechanical properties of brains and other living tissues, as well as tools for quantifying these properties, are currently poorly understood, but are an important subject in biomechanical studies and applications. According to the United States Center for Disease Control and Prevention (CDC), approximately 1.5 million people suffer from traumatic brain injury (TBI) yearly and more than 5.3 million people live with disabilities caused by TBI [1]. Globally, the number of affected people is estimated to be around 10 million [2]. Traumatic brain injury is described by the CDC as “a disruption in the normal function of the brain...caused by a bump, blow, or jolt to the head”, and is largely linked to sporting accidents. As such, efforts have been carried out to develop safer sports equipment that relieves undesired stress on the brain during collisions and other head-related incidents. Adaptive impact-absorbing helmet systems and supplemental protective pads are a few of these technologies under development that address risk reduction in sport-related TBIs [3, 4]. To best design these technologies and others to help prevent brain injuries, a better understanding of mechanical brain properties and tools for accurately quantifying them must be developed.

1.0 Background

In this chapter of the MQP, we will first review the current state of brain property measurements and the methods used to obtain them. We will follow this review with each methods' limitations. Second, we will introduce both objective-lens-based optical tweezers and fiber optical tweezers and discuss their potential to overcome the limitations presented previously. For the objective-lens system we will analyze the components comprising the system, and how the system itself has paved the way for cutting edge biological research. Limitations of the system will

also be reviewed. Third, we will discuss how novel fiber-based optical tweezers have improved on their objective-based counterparts, and their applications in biological and mechanical research will then be presented. Limitations of the fiber-based system will then be presented. Lastly, we will provide rationale as to why we choose to use optical fiber tweezers in this research.

1.1 Brain Mechanical Properties

The advent of sophisticated technology has not only augmented the living quality of our lives, but has also decreased the potential negative impact caused by such advancement. One of the most pivotal innovations to represent the benefits brought by the technology appears to be in medical treatment. For instance, Alzheimer's disease is the 6th leading cause of death with 5.7 million patients in the United States in 2018 [5]. Patients suffering from Alzheimer's disease have problems remembering and eventually losing their mental and physical functionality, which is ultimately the cause of death [6, 7]. The brain of the patient is found to be softer than the normal brain by 7.2% ~ 20%, as well as the degeneration in the neuro system [8]. To counteract the disease, technology serves as the auxiliary force for early diagnosis. According to the Alzheimer's Association, early and precise diagnosis would help save \$7.9 trillion in medical and health care [5]. Another example to show the importance of brain property measurement is the examination of the Traumatic brain injury (TBI). The injury, depending on its severity, can cause trouble in thinking, sensation, language, and emotions. According to the United States Center for Disease Control and Prevention, TBI remains the major cause of death and disability in the country. In 2013, TBI was the diagnosis in more than 2.5 million emergency department visits and more than 282,000 hospitalizations. In those injuries, nearly 50,000 people lost their lives [9].

1.1.1 Existing Knowledge of Brain Properties

Figure 1-1 below shows the relationship between the short-term Shear Modulus G_0 and the brain tissue injury. G_0 increases with the increase of shear stress, leading to the elevation of brain injury. Depending on setting the criteria for the TBI, the chance of having the injury may vary. For instance, Zhang et al. indicate that the chance of having the TBI will be 50% when the criteria is set to $78e-3$ MPa; and the chance of having the TBI rises up to 80% when the criteria is set to $1.0e-2$ MPa [10].

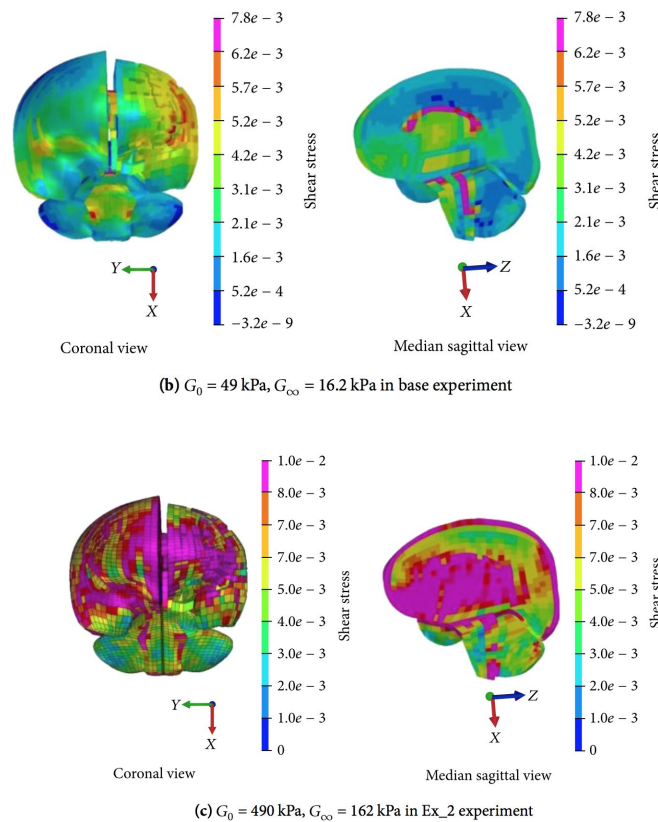


Figure 1-1: Shear Stress Distribution with Different G Values [10].

There are numerous studies on mechanical properties of brain tissue. As brain tissue is highly viscoelastic and goes through stress relaxation over time, researchers have been using the

linear viscoelastic constitutive method in modeling the mechanical properties of brain tissue. The constitutive equation for the shear modulus is:

$$G(t) = G_{\infty} + (G_0 - G_{\infty}) \times e^{-\beta t} \quad \mathbf{1-1}$$

where G_{∞} is the shear modulus after relaxation time long enough and the change in modulus is negligible; G_0 is the initial unrelaxed shear modulus; and beta is the decay coefficient (s^{-1}). Equation 1-1 underlines the change of brain tissue shear properties with respect to time: as time increases, the tissue relaxes and loses its initial shear modulus. This could happen within a very short time - less than 10 seconds [11].

Although researchers used the same mathematical model and similar experimental approach, they tend to generate results in dramatically different magnitudes. Table 1-1 below shows Zhang et al obtained dramatically different results from Finan et al's study [11, 12]. There has not been converged results that are universally agreed upon after many years of studying brain tissue properties. A new perspective could lead to potentially breakthrough results.

Table 1-1: Brain Properties Comparison from Two Studies.

Region	Finan et al [11]		Zhang et al [12]	
	G (Pa) (unrelaxed)	G (Pa) (relaxed)	G (Pa) (unrelaxed)	G (Pa) (relaxed)
Cortex Grey	168.8 ± 30.1	98.46 ± 16.4	34000	6400
Cortex White	957.9 ± 76.7	160.5 ± 12.8	41000	7800
Hippocampus	801.7 ± 63.7	172.4 ± 20.7	Not included	Not included
Brainstem	Not included	Not included	58000	7800

1.1.2 Methods for Brain Property Measurement

The two mainstream methods for measuring the brain properties are *in vitro* methods, meaning taking measurements outside of a living organism, or *in vivo* methods, meaning taking direct measurements in living organisms. Here, we will briefly discuss the differences between these two and the roles they have played in brain property measurement.

1.1.2.1 In Vitro Brain Property Measurement

Another way to examine the brain property is through *in vitro* methods. In early years, brain properties such as creep, recovery behavior and the viscoelasticity of brain tissue, were measured in various ways. For instance, Nickerson in 1964 measured Young's Modulus of human and dog brain tissues under static loading. In 1997, Lynne et al. conducted experiments that measured the rheological property of fresh bovine tissue [13]. Brain tissue samples were placed under the Bohlin VOR shear rheometer. In recent years, integrated Differential Scanning Calorimetry (DSC), a thermoanalytical technique, was integrated to check the thermal behavior of brain tissue slices and the effect in storage of brain tissue under low temperature. The results show a relationship between the behavior of brain tissue and the storage duration. The entropy and the mechanical strength in grey and white matter decreases as the storing period increases. The experiment further determines that the grey matter is proven to be less stiff than the white matter due to differences in composition under uniform compression [14]. Vappou et al. also had integrated MRE in the *in vitro* experiment on porcine brain tissue to make a comparison with reference mechanical measurement techniques, the rotational rheometry. The compared result proved the result from the MRE was in the same order of magnitude as from the conventional method. However, the *in vitro* measurement by the MRE shows a significant deficiency in its

frequency range. Since all soft tissues will have critical frequency value, the utilization of MRE to measure the sample rheological property and size [15].

Other *in vitro* measurements seen involve indentation of brain tissue. The reason this method is used is because the measurements are taken locally, meaning only a small amount of brain tissue must be homogeneous to obtain accurate results [16]. In Van Dommelen et al’s work, a spherical indenter was first used to apply pressure to porcine brain samples with the goal of obtaining the force required for indentation. Once this force was found, the indenter was used three times on each sample. Based on the speed of indentations, the time for a sample to fully relax and the influence of indentation depth was found. This method was then modified to one that creates indentations at different speeds and then carries out a stress relaxation test. The group’s results for different areas of brain samples are shown in Table 1-2 below.

Table 1-2: Average shear moduli of various regions of porcine brain using the indentation method [16].

	G (Pa)	
	White	Gray
Posterior	949 ± 311	669 ± 137
Superior	1209 ± 600	816 ± 213
Anterior	925 ± 354	738 ± 3.2
Thalamus	943 ± 109	
Midbrain	955 ± 137	

Budday et al applied similar experimental concepts to those used by Van Dommelen et al, but with a variation on indentation method to obtain their results [17]. Their method employs a TriboIndenter that applies force electrostatically while simultaneously measuring displacements of the brain sample. From their experiments, variations of Table 1-3 were generated with elastic moduli of different matter brain tissue. All brain tissue samples were from the coronal part of young bovine brain. The table rows indicate different locations that were indented on the brain

sample, and the columns indicate consecutive indentations. Budday et al used indentation depths of 10 μm at increments of 10 μm over 6 hours post mortem. As discussed before, there is quite a bit of variation in the elastic moduli of the brain depending on location, number of indents, and indentation depth. Despite this variation, moduli are consistently between 1-2kPa for gray matter and 1-3kPa for white matter. On top of this, the method seems stable as standard deviations are relatively small compared to the moduli measurements.

Table 1-3: Moduli of gray and white matter of brain tissue using the indentation method [17].

Gray matter moduli (kPa)							White matter moduli (kPa)						
Indent	I1	I2	I3	I4	mean	\pm std	Indent	I1	I2	I3	I4	mean	\pm std
#1	1.386	1.392	1.419	1.428	1.406	\pm 0.020	#1	1.295	1.329	1.347	1.381	1.338	\pm 0.036
#2	1.730	1.780	1.816	1.848	1.794	\pm 0.051	#2	1.594	1.617	1.647	1.676	1.633	\pm 0.036
#3	1.702	1.777	1.820	1.874	1.794	\pm 0.072	#3	2.896	2.996	3.068	3.141	3.025	\pm 0.104
#4	0.948	0.974	1.001	1.028	0.988	\pm 0.035	#4	2.071	2.145	2.148	2.197	2.140	\pm 0.052
#5	1.403	1.431	1.473	1.510	1.454	\pm 0.047	#5	2.390	2.429	2.474	2.504	2.449	\pm 0.050
#6	1.004	1.051	1.087	1.158	1.075	\pm 0.065	#6	1.331	1.369	1.405	1.445	1.387	\pm 0.049
#7	1.194	1.236	1.281	1.304	1.254	\pm 0.049	#7	1.018	1.035	1.055	1.093	1.050	\pm 0.032
#8	1.054	1.057	1.075	1.095	1.070	\pm 0.019	#8	1.883	1.914	1.946	1.970	1.928	\pm 0.038
#9	1.410	1.451	1.499	1.542	1.476	\pm 0.058	#9	1.987	2.058	2.142	2.234	2.105	\pm 0.107
mean	1.314	1.350	1.386	1.421	1.368		mean	1.830	1.877	1.915	1.960	1.895	
\pm std	0.287	0.299	0.304	0.307		\pm 0.289	\pm std	0.590	0.612	0.627	0.638		\pm 0.592

The indentation method, although used by many research groups, has several limitations. First, the method produced data that is often hard to interpret [16]. Van Dommelen et al cite contact conditions between the indenter and sample as an influence of indentation response that can be difficult to quantify. Inconsistencies in structure of the brain sample can also affect brain property responses; obtaining a perfectly isotropic brain sample is very difficult. Probably the

biggest drawback of the indentation method is that it cannot be used on human tissues *in vivo* [17]. Current *in vivo* methods are integrating better tools that aim at improving the quality of brain property data while eliminating some of the aforementioned limitations and drawbacks.

1.1.2.2 In Vivo Brain Property Measurement

In recent years, brain property measurement has been primarily accomplished by using the *in vivo* Magnetic Resonance Elastography (MRE) method. The basic operation of the MRE for brain property measurement is to stick the patient's head into the box in an MRI Scanner which connects to an external actuator that vibrates the head lightly to create shear deformation (see Figure 1-2). The advantage of using the MRE is that it can take the measurement noninvasively, meaning there is no need to take brain sample from a living organism. MRE is useful in taking brain properties such as viscoelasticity, stiffness, and neural microstructure [8]. However, prior MRE experiments lack fine spatial resolution to precisely scrutinize neuroanatomical structure, such as Subcortical Grey Matter (SGM), which is an indication of functional neuro degradation related to aging. This causes loss of measurement accuracy in small regions in the brain, as well as noticeable variance between reported data [18].

Scientists such as Johnson et al., have also started to take the *in vivo* measurement of brain properties, more specifically to the SGM with imaging scheme and inverted algorithm to provide a better spatial resolution [18]. Through the new setup, it is possible to localize a specific region in the brain when measuring the SGM, where the brain is surrounded by a low shear stiffness substance. Nonetheless, even with such novelty in MRE, it is costly to have the brain property measured by sophisticated instruments.

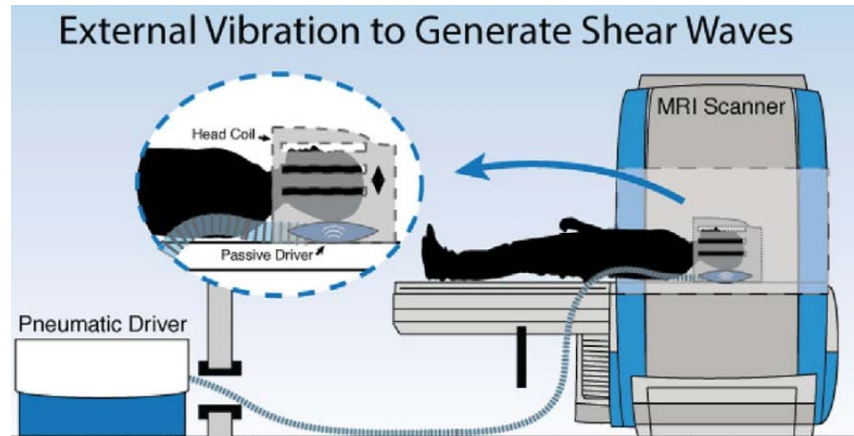


Figure 1-2: Operation of the MRE Experiment for Measuring the Brain Properties [8].

Another *in vivo* brain property measurement method is atomic force microscopy (AFM). AFM is one of the most common methods and uses a tip mounted on a small cantilever. When the tip moves over a surface atomic forces contact and displaces the tip [19]. Changes in the orientation of the tip are measured by a laser beam, which sends a signal to a bicell for position detection. A topographical image of the surface can then be generated by a computer during post-processing of the displacement data. The problems in this method are that physical contact must be made with the particle under investigation and three-dimensional trapping forces become hard to measure. Fiber optical tweezers solve these problems and provide a versatile tool for three-dimensional biomechanical studies. This paper will focus on fiber optical tweezer integration for brain mechanical property measurements.

1.1.3 Challenges of Existing Brain Measurements and the Need of New Tools

Despite the numerous methods employed to characterize the mechanical properties of brains mentioned previously, there is a lack of universal results. As can be seen in Figure 1-3 below that was alluded to earlier in Section 1.1.1, there are many disagreeing brain mechanical stiffness measurements obtained over a 50-year timespan. This figure also highlights that these

results can be orders of magnitudes off from each other. It is suggested by Guertler et al that the significant differences exist between material properties of the same tissue measured *in vivo* and *in vitro* [20]. In addition, Guertler et al propose collecting *in vivo* data would be more helpful, but the amount of data available would be limited.

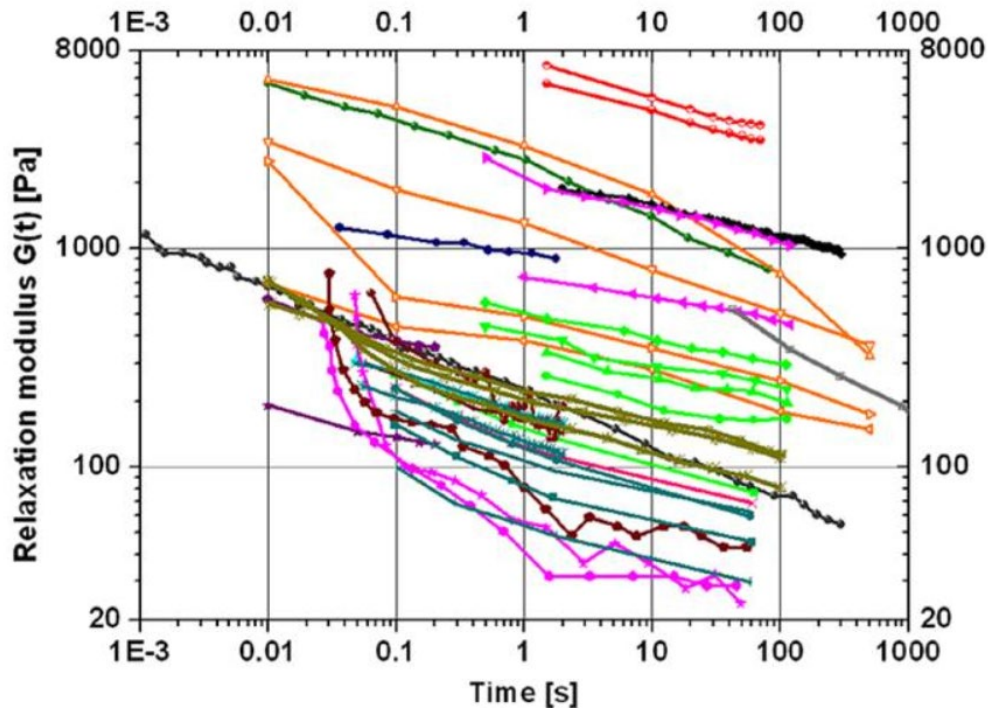


Figure 1-3: Fifty Years of Brain Mechanical Stiffness Measurements [21].

Other than measuring method, variations in data can also be attributed to tissue heterogeneity, brain anisotropy, inter-species variations, age dependence, post-mortem time, and experimental parameters [21]. Under experimental parameters, the method of holding a brain sample in place for shear deformation and temperature changes of the testing environment have been found to strongly influence brain property measurements [22-24]. Control of all of these variables is very difficult. Using a tool that takes measurements *in vivo* and does not make contact with the brain sample or produce local changes in temperature is the first step in eliminating some key experimental parameter influences. The tool that is capable of this is the fiber optical tweezers.

All living tissues display varying degrees of viscoelasticity, that is, their mechanical properties change under different strain rates. The tissues show different mechanical properties *in vivo* and *in vitro*, as suggested by Guertler and his fellow researchers. Using MRE under multiple frequency settings, they performed brain property measurements on the same samples, both *in vivo* and *in vitro*. Their goal is to prevent brain injury or to diagnose diseases, *in vivo* data would be more helpful, but the amount of data available is limited [20]. Optical tweezers, specifically the DFOTs, can address this problem and the many others occurring in more traditional methods. In the following section, we will first review the optical tweezers and their role in biological researches, then we will discuss advantages of the integration of optical fibers with this tool and why it is our tool of choice for obtaining brain property measurements.

1.2 Optical Tweezers (OTs)

Optical tools like the optical tweezers are some of the most important instruments used in cutting-edge biological and physical research. Recently, performance standards of these tools have increased with the integration of optical fibers. In particular, optical fiber tweezers that create optical traps have paved the way for more comprehensive and accurate cell mechanics studies to be conducted, with many more applications being explored. In the following section, the working principles of optical traps will be discussed. The evolutionary path of fiber optical tweezers will also be reviewed. In this review, traditional objective-lens optical tweezers will first be examined, followed by an analysis of novel fiber optical tweezers. Disadvantages of both technologies will be outlined.

1.2.1 Optical Trapping

Optical forces are the product of photon momentum change that light, specifically photons, carry resulting from refraction or scattering [25]. When light shines on a dielectric particle with a greater refractive index than the medium it is in, a scattering force along the light beam path and a gradient force pointing to the region of maximum intensity are generated [26]. These two components enable particle trapping when there is an equilibrium of these forces and other forces, including drag and gravitational forces from the surrounding medium [27]. Stable three-dimensional trapping has, in the past, been a product of single beam light with a large intensity gradient; this provides a strong gradient force necessary for trapping [28, 29]. To obtain a large intensity gradient, a high numerical aperture objective lens is required. A high numerical aperture objective lens strongly focuses the light and provides a strong axial light gradient, enabling highly efficient three-dimensional optical traps to be generated. Devices capable of optical trap generation using a single beam are called optical tweezers, and they have played an important role in biological system studies [29-31].

Optical traps produced by optical tweezers have become powerful tools in biological and physical applications ever since their advent over 30 years ago. These traps were initially capable of basic particle manipulation, but overtime have seen more advanced applications in position detection and mechanical property measurements [28]. Arthur Ashkin, an American recipient of the 2018 Nobel Prize in Physics first demonstrated 3D optical traps - the foundation for the development of more modern single-beam, gradient force optical traps. Under Ashkin's advice, a team in Japan, in 1991, became the first to achieve a 3D trapping by using laser ablation system to trap the polymer latex particle in the water. The goal is to study the effect of photochemical on various particles as well as chemical and physical property of a particle. Today, optical traps can

measure displacement of particles under induced pico-newton level forces with high precision for molecular motor studies [25, 32-34] and mechanical property measurements of polymers [35-37].

1.2.1.1 Nobel Prize for the Optical Tweezers

In 2018, Arthur Ashkin, an American scientist, won the Nobel Prize in Physics for his development of the optical tweezers [38]. The Nobel Prize in Physics is an award that has been given out since 1901 by the Royal Swedish Academy of Sciences for individuals who have made ground-breaking contributions to the world in the field of Physics that will stand the test of time [39]. This award is often considered the pinnacle of scientific achievement as only 209 individuals have received it to date. Ashkin, with his Nobel Prize in Physics, joins the ranks of iconic scientists such as Albert Einstein and Neils Bohr [40]. Prior to Ashkin's Nobel Prize in Physics, optical tweezers were relatively unknown; after being recognized for his landmark innovation, some of the best scientists in the world now acknowledge the massive potential this tool has to revolutionize biological system characterization.

1.2.2 Traditional (Objective-based) Optical Tweezers

Most of the currently used optical tweezers are based on objective lenses. In the rest of this MQP, we will refer to this category of optical tweezers as traditional optical tweezers. To understand how the objective-based optical tweezers and their formation of optical traps have played an important role in biological studies, the system must be reviewed. Figure 1-4 displays a schematic of an objective-lens-based, traditional optical tweezers system. See Table 1-4 for the components of the traditional optical tweezers system and their roles and functions in the system. Each component forms an integral part of the trapping system, allowing for robust optical traps.

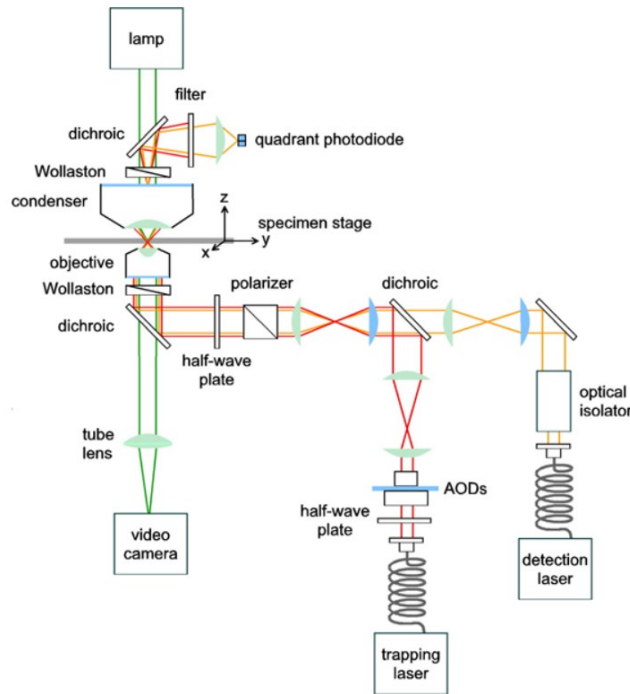


Figure 1-4: Schematic of Traditional Objective-lens-based Optical Tweezers [41].

Table 1-4: Purpose of Components of Traditional Optical Tweezers.

Component	Purpose of Component
Dichroic mirrors	Spectrally transmits a small range of wavelengths while reflecting others. Transmits light used for microscope illumination but reflects light into the optical path of the microscope.
Filter	Spectrally transmits a range of wavelengths.
Wollaston prism	Separates polarized and unpolarized light into two distinct, linearly polarized beams.
Condenser	Provide illumination to a sample; helps minimize image manipulation.

Polarizer	Performs like a Wollaston prism; lets specific polarizations of light waves pass while blocking others.
Quadrant Photodiode	Detects position of laser beams for precise path alignment of them.
Half-wave Plates	Alters polarization state of a light wave traveling through it; rotates the plane of plane polarized light.
Acoustic-optic Deflector (AOD)	“Control both the trap position (through deflection) and stiffness (light level)” [28].
Tube lens	Secondary lens for image generation

One of the most important components of the objective-based OTs in the laser source that is responsible for optical trapping. Without this component no optical trap could be possible. In practice, free space lasers or fiber-coupled laser diodes have been used for optical traps [42-44]. For the trapping laser, the wavelength and output power range parameters must be considered. When dealing with biological samples, transparent wavelengths must be selected, typically either 830 or 970 nanometers [45], to reduce photodamage to the sample [46-48]. Trapping quality and optical force attainability can be determined from the output power of the selected laser source. Possible laser sources include fiber-coupled laser diodes and diode-pumped solid-state lasers, although cost can play a major role in laser source selection.

As the name of the tool suggests, another important component of the objective-based OTs is the objective lens which is responsible for focusing the trapping laser. Much like with the trapping laser, a variety of objective lenses can be used depending on the application; working distance can be an influential factor in objective choice. When deciding the objective lens to use,

the medium of immersion must also be taken into consideration, as it influences the working distance of the trap. For instance, using a medium of water increases the working distance of the trap, as there are fewer peculiarities [28]. Differently, a medium of glycerol has a lower working distance because there are more peculiarities.

Objective-based optical tweezers, as mentioned previously, have the capability to trap and manipulate a large range of particle types in the sub-nanometer to micron scales, including most single-molecule and single cell biological samples [49, 50]. However, limitations of objective-based optical tweezers must be considered and understood before conducting biological experiments.

1.2.3 Limitations of Objective-lens-based Optical Tweezers

As can be seen from Figure 1-4, there are many different components involved in the system, each having the potential to cause problems. All components in the system must be fully functional in order for the optical tweezers to generate stable optical traps. Even if all of the components function properly, the user must be familiar with microscopy, laser techniques, and optical fundamentals to properly realize optical traps. Other drawbacks that limit the system's applications include the system's bulkiness, short working distance, integration difficulty, heat generation, and cost [26].

In terms of the physical size, most objective lenses are around 200 millimeters in diameter and multiple times that in length [51]. To move the optical trap more system components are required. These components include wave plates [52], spatial light modulators [53], and diffractive optical elements [54] among others. The combination of the objective system and the aforementioned elements takes up quite a bit of space and also decreases portability. In addition to being bulky, traditional optical tweezers require an optically homogeneous medium and

transparent substrate. Any optical perturbations within the optical field path or within the medium of trapping will cause a decrease of efficiency in the optical tweezers, as the intensity distribution will be degraded [51]. For this reason, optically homogeneous mediums are preferred. While trapping with objective lenses, heat produced from the laser is another important aspect to consider; at the focus of the trapping laser the intensity spikes to between 10^9 and 10^{12} W/cm [55]. This spike causes local heating which influences the viscosity of the medium of trapping and the mechanical properties of biological samples being trapped, for instance [26, 56]. Due to these limitations, traditional optical tweezers systems are seldom used in confined places or in the field. To overcome these limitations, optical fiber tweezers have been introduced [26-27, 57-58].

1.3 Fiber Optical Tweezers

Fiber optical tweezers are the newest generation of optical tweezers that form optical traps under the same principles outlined in Section 1.2.1, while also providing intrinsic advantages over their objective-lens-based counterparts. Intrinsic advantages of this tool include more flexibility, resistance to EMI, and small size. These advantages are only made possible by the integration of optical fibers. Before going into further detail on fiber optical tweezers, we will first examine optical fibers and provide more detail on their intrinsic advantages; then, we will review some of the optical fiber's most important applications.

1.3.1 Optical Fibers

To understand how DFOTs can be used to improve on current brain property measurement methods, it is important to review optical fibers, how they work, and their various applications. Optical fibers have been widely used in telecommunications to transmit light from one location to another, but to understand how this is possible, the fundamentals and working principles of optical

fibers must be discussed. Optical fibers are very thin, transparent, and flexible fibers normally made of silica or plastic that can guide light over long distances [59]. A typical optical fiber has three layers: the jacket, cladding, and core (see Figure 1-5). The jacket is a protective layer that absorbs shocks and moisture that could damage the cladding, the cladding is a reflective layer that keeps light in the core of the fiber with its lower refractive index, and the core is the guide for light input.

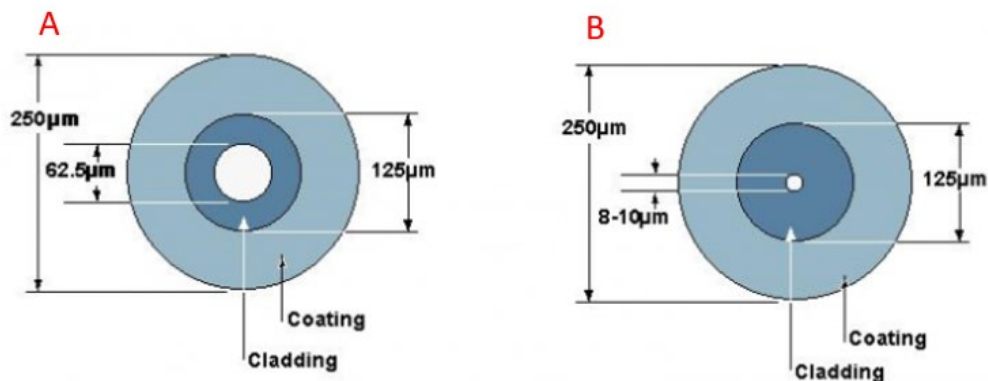


Figure 1-5: Multimode (A) and Singlemode (B) Fiber Cross-Section [60].

The diameter and material of an optical fiber determines the type of light that it can reflect and transmit [61]. In general, there are three classifications of optical fibers: single mode, graded-index multimode, and step-index multimode, where a mode is a path light can travel through the fiber. These classifications are different in indexes of refraction - the bending of light when it passes from one medium to another [62]. Index of refraction is calculated as the ratio of the speed of light in a vacuum to the speed of light in the medium. Singlemode fibers, as the name suggests, has only one path that light can travel down; graded-index multimode fibers have a constant cladding index of refraction and a varying core index of refraction; and step-index multimode fibers have different, but constant, cladding and core indexes of refraction (see Figure 1-6) [63]. Singlemode fibers are best used for longer distance communication and transmission because they

suffer from less attenuation while also having larger bandwidth [64, 65]. Graded-index multimode fibers have higher attenuation than singlemode fibers, but minimize pulse broadening from intermodal dispersion and are limited to medium distance communication and transmission. Step-index multimode fibers are limited to short distances. Each fiber type has its benefits and drawbacks depending on the application.

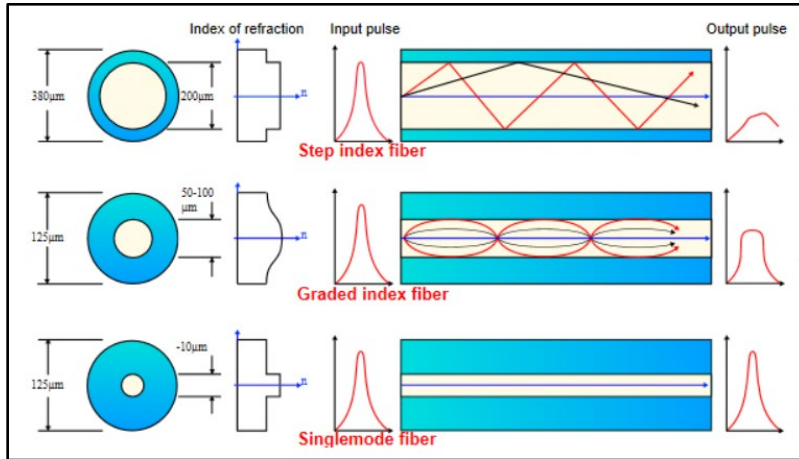


Figure 1-6: Classifications of Optical Fibers and Their Characteristics [66].

1.3.2 Working Principles of Optical Fiber Light Transmission

Optical fibers are used primarily to transmit light, but how is the fiber able to guide light such long distances with little loss? As light passes from a lower index of refraction to a higher index of refraction, light refracts towards the normal. The amount of refraction can be calculated using Snell's Law:

$$n_1 * \sin(\theta_1) = n_2 * \sin(\theta_2) \quad 1-2$$

where n_1 and n_2 are the refractive indices of material one and two respectively, θ_1 is the angle of incidence, and θ_2 is the angle of refraction. Total internal reflection (TIR) is the principle that allows optical fiber transmission to occur; it describes how optical fibers can keep all light inside the fiber, and it is caused by the principles causing refraction. It can only occur if the following

two conditions are met: light is in a denser medium and is traveling towards a less dense medium, and the angle of incidence is greater than the critical angle [64, 67]. The critical angle is the incident angle required to have a refracted angle of 90° and can be calculated using Snell's Law:

$$\theta_c = \arcsin\left(\frac{n_1}{n_2}\right). \quad 1-3$$

Under total internal reflection, light passes from a higher refractive index to a lower refractive index at a large enough angle of incidence such that all light in the fiber is reflected (see Figure 1-7). This principle is the backbone to many applications of optical fibers such as telecommunications and optical fiber sensors.

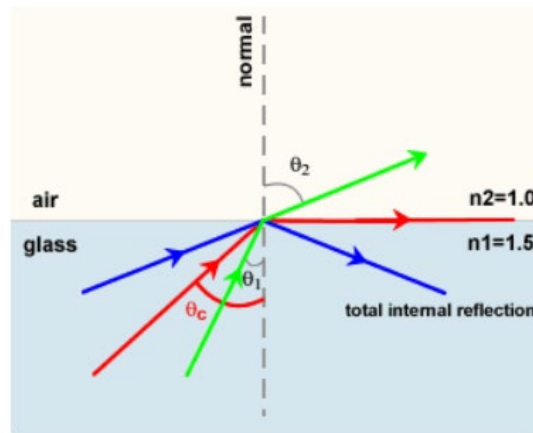


Figure 1-7: Illustration of Total Internal Reflection [68].

1.3.3 Applications of Optical Fibers

Optical fibers are a versatile tool in applications ranging from networking and telecommunications to surgical tools and structural health monitoring sensors. In comparison to traditional electrical cabling, optical fibers are immune to electromagnetic interference while at the same time able to transmit signals much longer distances, making them a more robust method of choice for data transmission. Optical fibers are also used during surgeries as light guides and

imaging tools such as endoscopes. Integration of optical fibers in medicine allows doctors to operate inside a patient's body through microscopic incisions without traditional, invasive surgical methods. Fiber optic cables as sensors have seen use in industrial environments too, allowing engineers to monitor structural health in real time, helping them predict structural performance under certain loads and in the future. In this section, we discuss some of these applications in more depth, along with some of the benefits optical fibers provide over their traditional counterparts.

1.3.3.1 Optical Fibers in Networks and Telecommunications

Optical fibers in signal transmission are different than standard copper cabling media because the signals being transmitted through the fibers are light pulses rather than electrical signals [64]. A light source will pulse in the pattern of the binary encoded signal at a certain wavelength with a high frequency; this pulse will then be decoded by a receiver. Fiber optic cabling for networks has seen an increase of usage over electrical cabling mainly because fiber optic cabling systems are immune to electromagnetic interference (EMI), have longer distances of travel, and can transport data at higher rates [64, 69-70]. These benefits will be explained in detail below.

1) Immunity to Electromagnetic Interference

Standard copper cable media suffer from EMI which negatively interferes with electrical transmission [71, 72]. For instance, if two copper cables with electrical signals running through them are placed next to each other, crosstalk - exchange of power between the copper cables - will occur [73]. Optical fibers do not need to worry about crosstalk because light travels through a glass tube which does not conduct electricity. Crosstalk was the working principle in the development of wiretaps. Wiretapping, in a traditional sense, is a method of monitoring telephone

conversations covertly and was achieved by connecting a listening device to the electrical being sent through phones [74]. Optical cabling neutralizes wiretapping because the cables are immune to crosstalk. As a result, the optical fibers can be used in areas susceptible to EMI such as in machinery and transformers while also serving as a protective mechanism for data transfer, no matter the distance of signal travel.

2) Signal Travel Distance

Typical copper cabling has a distance limit of around 100 meters because after this length serious signal degradation occurs [75]. Because of this, signal repeaters must be used, which add significant cost to the cabling system. Single mode optical fiber cabling has seen regular travel distances of about 75 kilometers without signal boosters, with maximum distances of up to 200 kilometers, and is also significantly cheaper than copper cabling [64, 76].

3) Higher Data Rate Transfer

With virtually no interference loss or distance attenuation, and because light travels quickly, larger data transfer rates are seen over long distances with optical fiber cabling. The throughput of data is determined by the frequency range capable by a cable; a higher frequency range correlates to a larger bandwidth and thus more data transferred [28]. Optical fiber cables can carry larger frequency ranges while copper cabling attenuates at higher frequencies, therefore optical cables have significantly higher bandwidth than those of copper cables. Data rates upwards of tens of gigabits per second are possible with optical fibers, where their copper cable counterparts are just breaking the gigabit per second mark [77, 78]. When hearing the term “fiber optics” the general audience turns to fiber optic networks and telecommunications, but fiber optical sensors

are another important application of optical fibers that have made many noteworthy breakthroughs since their advent.

1.3.3.2 Fiber Optical Sensors (FOS)

Fiber optical sensors are at the forefront of recent sensing technology because they offer numerous advantages over existing sensors, including increased sensitivity, flexibility, and large bandwidth [79]. Generally, optical sensors take light and convert it into an electrical signal such that it can be read by an integrated measuring tool or device. Some fiber optical sensors use the physical optical fiber as a sensor - intrinsic sensor - or the transport medium for a signal to a remote sensor - extrinsic sensor. Some key applications of optical sensors are in hazardous gas monitoring, structural health monitoring, and pressure sensing, however, for the scope of this MQP, we will only briefly discuss their working principles. Several optical sensors that have wide applications will be introduced in detail below.

1.3.3.2.1 Hazardous Gas Monitoring

With the advantages of long traveling distance with little loss or corruption and fast response time, optical fibers have also been implemented in environment monitoring system for remote locations. One important field is the coal industry, where the concentration of Methane (CH₄) gas and Carbon Monoxide (CO) in air is crucial for preventing a catastrophic explosion in a coal mine. Traditional gas sensors consist of a sensing resistor and an inert resistor configured in a Wheatstone bridge to monitor the ratio of the two resistors, and ultimately, the combustible gas concentration. They have small sensing range typically within 4% and requires frequent recalibration. An example of a gas monitoring fiber optical sensor schematic can be seen in Figure 1-8. The ideation of fiber optics methane detector was realized by Culshaw and his colleagues in

1998. The remote methane gas monitoring system based on Near Infrared (NIR) in optical fiber was built and tested to be successful [80]. As studied by Liu et al, fiber optical sensors in gas detection can reach 0-100% full detection range without recalibration. They further built up the concept of overall coal mine hazard detection based on FOS. By adopting FOS to monitor other gases, water levels, and micro-seismic motion, parameters in the coal mine environment can be gathered accurately, then analyzed to prevent hazardous conditions to the mine workers [81].

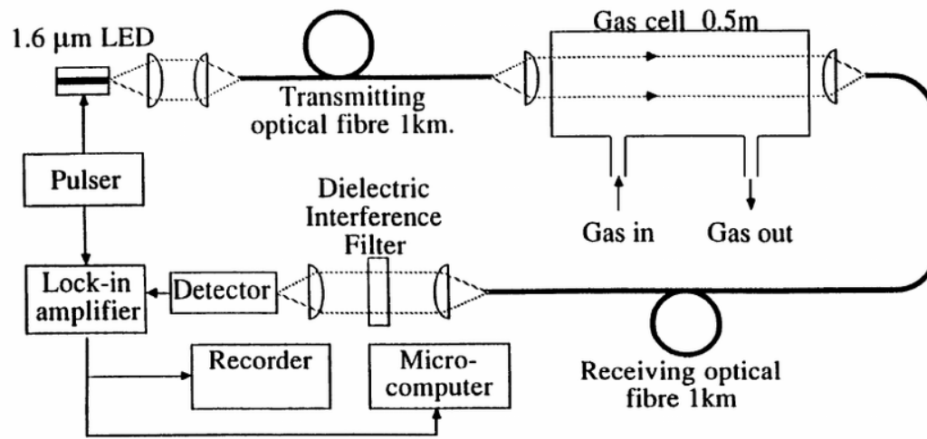


Figure 1-8: Block Diagram of CH₄ Monitoring Fiber Optical Sensor [82].

1.3.3.2.2 Structural Health Monitoring

Optical sensors, both with or without fibers, have been studied for structural health monitoring (SHM). Structural health is crucial, especially in the aerospace industry, in which metallic fatigue and crack propagation could turn into fatal accidents. In 2018, Choi et al. showed their experiments in using optical sensors to monitor aircraft structure both in a hangar and in motion [83]. Traditional health monitoring systems typically include piezoelectric sensors in critical locations where fatigue is most likely to develop. However, multisite cracks are not monitored in this method and their propagation to bigger crack could lead to catastrophic results. To overcome the drawback of previous monitoring scheme being discontinuous, Choi's team used

guided laser ultrasonic wave propagation imaging to monitor the global damage on the airframe continuously. This could increase efficiency and accuracy in a hangar to service aircraft.

The researchers also worked on fiber Bragg grating (FBG) sensors to monitor real-time deformation along the airframe. They suggested this would be helpful in evaluating the health of the structure or even the extent of damage on airframe upon minor collision. This would give the pilot or the computer, in the case of an unmanned aircraft, a better picture in terms of operability of the damaged aircraft [83]. A typical structure monitoring sensor schematic can be seen in Figure 1-9 below.

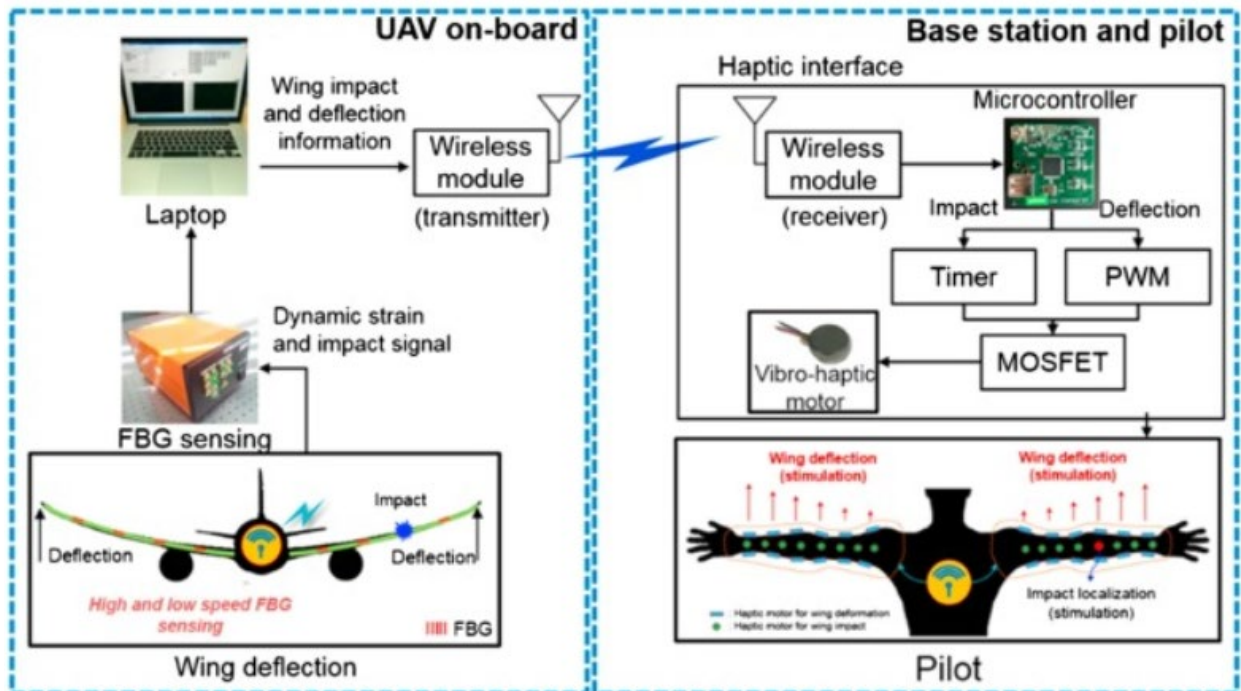


Figure 1-9: FBG Aircraft Deformation Monitoring System Schematic [83].

1.3.3.2.3 Fiber Optical Pressure Sensors

Fiber optical pressure sensors are some of the most popular devices currently used alongside medical catheters and guidewires for in vivo, non-invasive pressure measurements, for instance [84, 85]. Two of the most common optical fiber pressure sensors are intensity-based and

Fabry-Pérot. In intensity-based optical fiber pressure sensors, light is collected by a multimode fiber after reflecting on a diaphragm that deflects under an applied pressure (see Figure 1-10) [86, 87]. The collected light's intensity is directly related to the distance separating the diaphragm and fiber tip. Light intensity increases as the diaphragm moves closer to the fiber tip as there is more light reflection close to the fiber end, but decreases as the diaphragm moves away from the fiber tip because there is more space for light scattering. This decreases the amount of light entering the fiber, thus lowering its intensity. These sensors are typically designed based on a desired pressure range to be analyzed and can be modified to fit the needs of the application. Optical fiber pressure sensors do not need expensive optical equipment to be effective; in fact, an LED and photodiode could be used simultaneously to give off and collect light into a multimode fiber providing the desired pressure measurements [86]. Although exhibiting advantages noted in Section 1.1.2, intensity-based sensors have their drawbacks mainly resulting from errors in fiber alignment, system vibration, and fiber end face contamination [88].

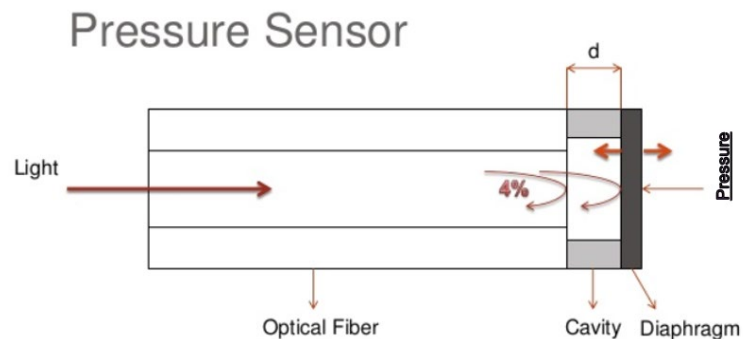


Figure 1-10: Intensity-based Optical Fiber Pressure Sensor [89].

Fabry-Pérot interferometric pressure sensors are another common variant of optical fiber pressure sensor that uses two partial reflectors sandwiching a medium of optical transparency to create a resonance cavity [87]. This cavity is typically located at the end of an optical fiber (see Figure 1-11) [84]. A laser source shoots a light beam to the first mirror which reflects and transmits

fractions of the beam through to the second mirror. One of the advantages of the Fabry-Pérot pressure sensor is that it can be used with “...low coherence light sources, such as light emitting diodes (LEDs)...since the optical length of the miniature cavity is of the same order as the wavelength of the light” [90]. Coherence is a way to measure the interference between wave functions produced from light sources [91]. Fabry-Pérot pressure sensors are some of the most preferred optical fiber sensors commercially available because they not only measure a variety of parameters like pressure, temperature, and strain, but they also provide the greatest size and pressure range flexibility [86].

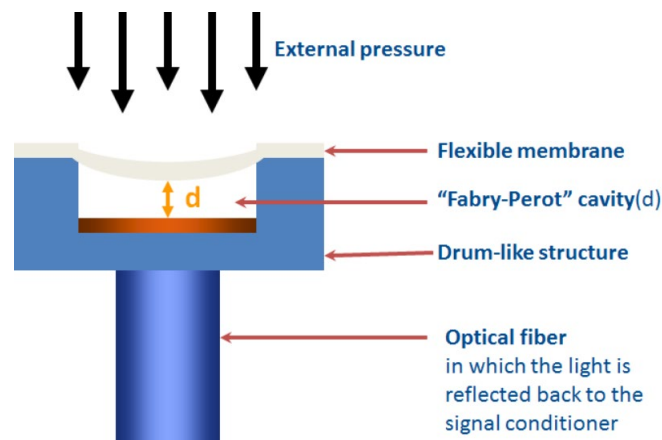


Figure 1-11: Operation of Fabry-Pérot Pressure Sensor [92].

1.3.4 Optical Fiber Tweezers

The optical fiber tweezers platform allows one to deliver a miniaturized, self-sustaining fiber optical trapping system, in which a three-dimensional optical trap is created and calibrated *in situ* without the need of an objective lens. Optical fiber tweezers are also much lower in cost, have larger working distances, and are much more integratable [26]; we will go into more detail on these later in this section. A common optical fiber tweezers setup that can obtain three-dimensional trapping is the counter-propagating dual-fiber optical tweezers (DFOTs) [26-27, 93-94]. See

Figure 1-12 for a schematic of the counter-propagating DFOTs. The optical fibers used in this arrangement are normally either cleaved or lensed. Other fiber-based optical tweezer variants exist, such as the single-fiber-based optical tweezers [95] and fiber-bundles-based optical tweezers [96, 97], but for the purposes of this MQP, we will only discuss the counter-propagating DFOTs and their applications, as they will be our choice method for optical trapping and mechanical property characterization.

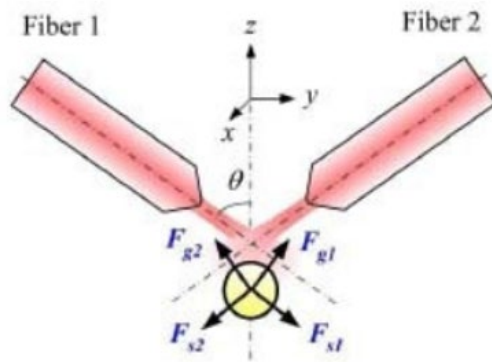


Figure 1-12: Dual-fiber optical tweezers with gradient and scattering force vectors [27].

Perhaps one of the biggest advantages fiber optical tweezers have over objective-lens-based optical tweezers is their cost. The price of bare optical fibers ranges between a few cents to a few dollars per meter of fiber, whereas the objective used in the objective-lens system alone can cost hundreds of thousands of dollars. To put more context to these numbers, Corning brand SMF-28 Ultra Optical bare fiber costs eight cents per meter [51]; an “inexpensive” objective-based optical tweezers system built entirely of commercially available optical equipment costs around \$6500, excluding time taken to put the system together [98]. Comparing the optical fiber tweezer system to the objective-lens system, it is clear the optical fiber is more cost effective and affordable for lab and industry use.

Another benefit of the optical fiber tweezers is that unlike traditional objective-based OTs where a beam from a laser must pass through the base of a sample, the fiber optical tweezers can generate optical traps from the light emitted from the fiber tips [51]. Because of this, fiber OTs can be inserted from the top of the medium with more flexibility than that of the traditional OTs. Based on these principles, fiber-based OTs are not as limited to working distance inherent in objective lenses. Fiber-based OTs, using the counter-propagating setup, also have the capability to measure the deformation of micron-scale biological samples of red blood cells, which is something objective lens-based systems cannot [99].

In addition to increased working distance, fiber-based OTs are able overcome the problem of heat generation seen in the objective-based OTs that can introduce data accuracy complications in biological system experiments [51]. The diffraction-limited spot from objective-based OTs is much smaller than the larger focus spot from an optical fiber. Since the focus spot is larger, the heat produced from the light dissipates through a larger area, lowering the localized temperature. This makes experimental data from a biological study less susceptible to skewing from the heat.

In terms of applications, counter-propagating fiber-based OTs have seen much use in biomechanical and physical studies, including but not limited to manipulation of micro and nanoparticles, cell sorting, and particle tracking [26, 29, 100-101]. Using the fiber-based optical tweezers, living yeast cells were trapped and manipulated [102]; mechanical properties of red blood cells and fibroblasts were measured [103]; and differences between regular and irregular cell elastic responses to optical forces were observed [104]. Among the wide variety of applications in which fiber optical tweezers are integrated, some of the most active applications are cell and polymer mechanical property measurements.

1.3.5 Limitations of Optical Fiber Tweezers

Although some fiber-based optical tweezers improved on certain limitations of objective-based optical tweezers, they still have some limitations in applications. For instance, in Berthelot et al's article in 2014, they pointed out that insufficient optical power from the near-field fiber optical tweezers, in conjunction of with potential photothermal inducing properties, has limited fiber optical tweezers' full application in moving nanoparticles in three dimensions [105].

In Ti et al's work in 2017, they recognized that fiber-based optical trapping is limited by the shape of the particle one is trying to trap [106]. As explained in the last section, fiber-based optical trapping relies on the scattered light from the particle. If the particle is spherical, the scattered light depends only on particle's displacement; if the particle is not spherical, orientation of the particle can influence the scattered light as well. In the latter case, a strong trap is hard to establish. Trapping non-spherical particles is difficult for fiber-based trapping systems.

Another drawback pointed out by Ti et al's work was the short working range of the system [106]. A smaller distance between the tips can generate greater sensitivity in position detection. The fiber tips are rather close to each other (80 microns), and they are extremely close to the particle being trapped (tens of microns). This hinders the system's capability to trap particles deeper in the 3D matrix. Ti et al suggested developing a stiffer set of fiber holder to allow penetration deeper in the matrix without damaging the fibers. However, it is still a working progress.

Other than the performance drawbacks, there is the need to align the fibers, as misaligned fibers unevenly distribute optical forces on particles, making optical traps much harder to realize. Uneven optical forces can unintentionally manipulate the particle the user is trying to trap. For example, a slight misalignment can cause unwanted rotation on a particle which can decrease the

stability of the optical trap. Details regarding the alignment process and where error can occur will be discussed in our Methodology Chapter later. In addition to fiber alignment, the fabrication time for such a system is highly variable. The fabrication time for such a system requires a high level of detail and focus; any error can lead to a more time-consuming process. More specific details regarding the fabrication process and potential errors will also be discussed later in our Methodology Chapter. The benefits fiber optical tweezers provide over their objective-lens-based counterparts outweigh their limitations, leaving a potential for the advancement of non-invasive brain property measurement that is not possible with traditional objective-based tweezers. For this reason, we propose the use of fiber optical tweezers in this research.

1.4 Motivation

To reduce the commonality of brain injuries and remedy them more appropriately, understanding the properties and condition of the brain is crucial. Having the correct tools to identify the aforementioned is also of great importance. Properties of brain tissues have not been as comprehensively investigated as other parts of the body such as the skeletal system or blood vessels. Current technology provides noninvasive, *in vivo* brain property measurement, but lacks the resolution to evince the tissue structure. Additionally, the operation can be costly. *In vitro* experiments to obtain brain property measurements, though they have been developed over decades, yields a wider range of results due to the absence of vascular network pressurization and autolytic processes [21]. After reviewing different existing brain property measurement methods, a more thorough investigation is called for. The team discerns the need to integrate more feasible, affordable, and accurate tools and measurement approaches for this investigation. Recent advancements in micro and nano-scale mechanical property measuring techniques, specifically the inclined dual-fiber optical tweezers (DFOTs), have allowed further exploration to be possible. In

this MQP, we aim to develop a modular system implementing the inclined DFOTs to obtain preliminary mechanical stiffness measurements of grey and white matter in brains.

1.5 Summary

To get into a more holistic view of our goal in this project, in Chapter 2, we provide our experimental setup, including the fabrication of the modular system that will be used to measure mechanical brain properties, as well as the methodology to properly set up the experiment for precise measurement. In Chapter 3 we will discuss the mathematical theory that back our experimental procedures, followed by a discussion of the different codes we use to collect, process, and fit our experimental data. In Chapter 4, after discussing the underlying mathematical foundation and our data collection tools, we encompass our analysis and the findings. First, we present our findings through our experimental setup. We then integrate all our findings into one exhaustive analysis and make an analytical comparison between existing brain property measurements and our empirical results. Finally, in Chapter 5, we will discuss conclusions from our experiments using our innovative design, we will review its caveats, and we will make future recommendations for carrying out similar experiments in the future.

Chapter 2. Design and Fabrication of Modular Fiber Optical Tweezers

The goal of the modular fiber optical tweezers (MFOTs) is to eliminate the constant need of realigning the optical fibers used in fiber optical tweezers, create a portable and robust trapping system, and make the system as compact as possible. Fiber optical tweezers fabricated in the Optomechanics Lab were previously fabricated using two sets of mechanical stages, where each set can adjust an individual optical fiber's x-position, y-position, z-position, and rotational angle around the x-axis (see Figure A-8 in the Fabrication Guide). The degrees of freedom of this system limits the trapping stability of the fiber optical tweezers, in part because these components are heavy relative to the optical fibers. Overtime, movement of the system will be seen because of this weight and other vibrations, necessitating realignment of the fibers in the system. To help fix this problem, a compact modular fiber optical tweezers system with no extra mechanical components and a more robust fabrication method should be developed. Properly fabricated modular fiber optical tweezers can be used in more applications than traditional optical tweezers with its advantages, such as but not limited to portability, compatibility, and precision.

2.1 Design of Modular Fiber Optical Tweezers

Modular fiber optical tweezers have the same functionality as traditional fiber optical tweezers in that their main purpose is in generating 3-dimensional optical traps under the same principles outlined in Section 1.2.1. However, this novel system aims at replacing components in a traditional optical tweezers system that limit its widespread usage and integrality, including external devices like a position sensitive detector or quadrant photodiode that enable force sensing and the optical trap. At the same time, the MFOTs improve on DFOTs in that they have all the benefits of the DFOTs, but are much more stable and have less components. The MFOTs use two

permanently fixed and aligned optical fibers that are capable of generating 3-dimensional optical traps without further alignments throughout its use. The trap can be shifted anywhere in a testing medium simply by moving the common board instead of separately moving and recalibrating the two trapping fibers. Combining a fiber-based position detection unit with the MFOTs enables a mobilized optical trap spring constant measurement and position detection without cumbersome equipment like external high-speed cameras, for instance. This increases the affordability of the system and opens up many applications for which the MFOTs can play an impactful role. The final setup schematic of the DFOTs compared to the MFOTs is shown in Figure 2-1 below.

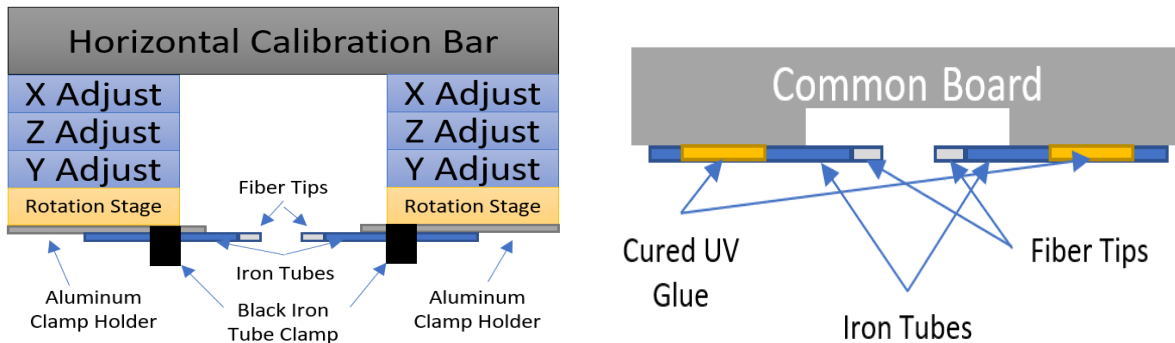


Figure 2-1: Schematic of view from above of DFOTs (left) compared to MFOTs (right).

2.2 Optimization of the Existing Fabrication Method of Modular Fiber Optical Tweezers

We worked primarily on refining the MFOT fabrication method because, previously, common board attempts had a success rate of approximately 50 percent; and when each attempt takes several hours, this is a large time sink. Even if the common board attempt was successful, the boards were seen to be susceptible to creep, meaning over time fiber and thus the light spot alignment would drift and the board performance - trap stability - would decay. For these reasons, we enhanced the old fabrication methods. The old method for fabricating a MFOTs system can be found in our lab's previous works [26-27, 107]; our new methods can be found in Appendix A.

In the next section, we will detail the main changes we made to the fabrication method of the MFOTs and how they have increased the success rate of fabrication.

2.2.1 Clamping Mechanisms for Fiber Tubes

Prior to our modifications, the mechanism used to hold the fiber tubes to the alignment modules was tape. Using tape, the fiber tubes were not held down sufficiently and overtime the tape would lose its adhesive strength and the fiber tubes would move, thus ruining the fiber alignment (see Figure 2-2).

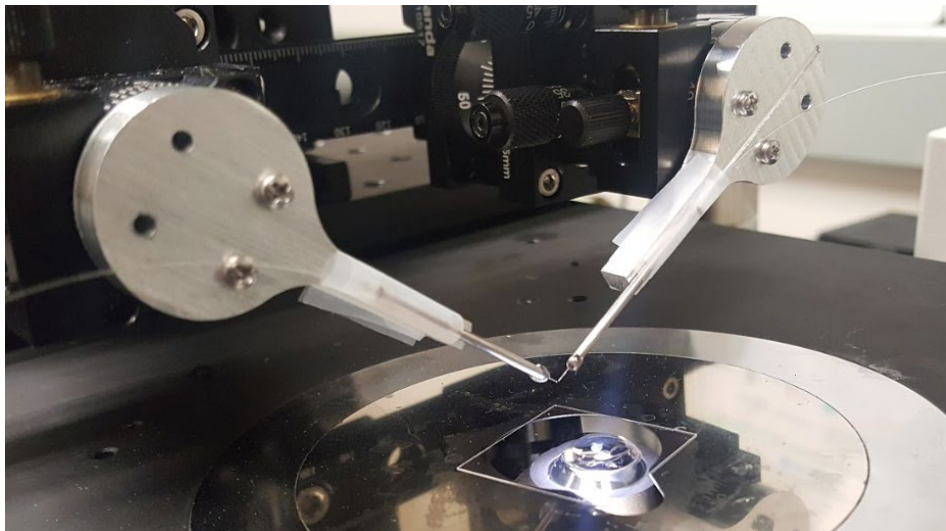


Figure 2-2: Tape holding the fiber tubes.

In addition, removal of the fiber tubes from the tape after transferring to the common board was very difficult, as trying to remove the tape would pull the tubes and induce unwanted forces that had the potential to misalign the fibers or even shear them off the common board. To solve these problems, it was recommended that we use a mechanical V-groove clamp that was controlled by screws. Figure 2-3 below shows this design. By using screws in the clamp, the amount of physical contact with the tubes was minimized and removing the tubes was more controlled and less violent. Using these clamps also increased the repeatability of mounting the fiber tubes, as the fiber tubes

are always pushed into the V-groove and are not able to create angles with the alignment module when applying tape.



Figure 2-3: V-groove clamp to hold fiber tube.

2.2.2 Rotational Stage

In the old fabrication method, the common board was moved in towards the fiber tubes; if misaligned with the tubes, only one of the tubes would move into the glue and would cure properly. If the board was moved further inwards to make contact with both fiber tubes, the board would further push the one fiber tube that was already making contact with the glue and ruin the light spot alignment. To solve this problem, a rotational stage, shown in Figure 2-4 below, was added to the common board transferring side of the system to help with aligning the common board with both fibers prior to transferring to the common board. When slowly moving the common board in towards the fiber tubes, we monitor which fiber tube moves first when the common board makes contact. With this knowledge, we know which direction to rotate the common board using the rotational stage such that both fibers move at the same time when touched by the common board. This helps keep the fiber tubes aligned during their transfer to the common board.

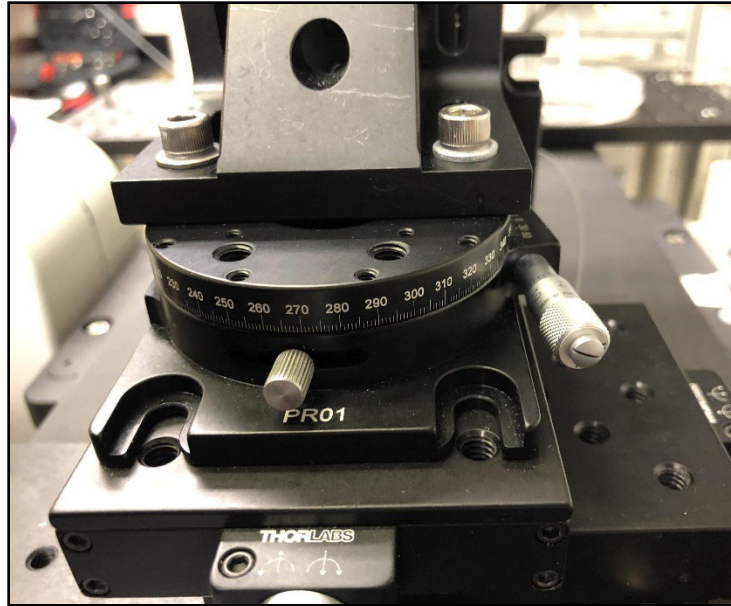


Figure 2-4: Rotational stage on the common board fixation module.

2.2.3 Adhesive for Fiber Tubes

We also modified the adhesive application method used when transferring the fiber tubes to the common board. In the previous fabrication method, a single layer of NOA-68T UV (Norland Products) glue was applied to the extrusions of the common board using a syringe. One of the issues with this was that the binding between the tubes and common board was not very strong, and over time - about two weeks - the alignment would decay, and light spots would get affected because of glue creep (see Figure 2-5). Through a UV glue test, it was discovered that the NOA-68T UV glue was not meant for adhesion to aluminum or other metals, but is quite strong when curing to other UV glue. To eliminate the effects of creep and better fix the tubes to the common board, we decided to use DYMAX OP-29-GEL UV Optical Adhesive (Fiber Optic Center) in place of the NOA-68T UV glue, as it better adheres to metals. We also chose to add a much more viscous layer of NOA-68T UV glue (Norland Products) over the cured DYMAX glue that would better secure the fiber tubes to the common board. Although this adds a few extra minutes to cure

time, the binding is much stronger; a creep test on a common board produced with this method verified that the alignment between the two fiber light spots was still present after a month.

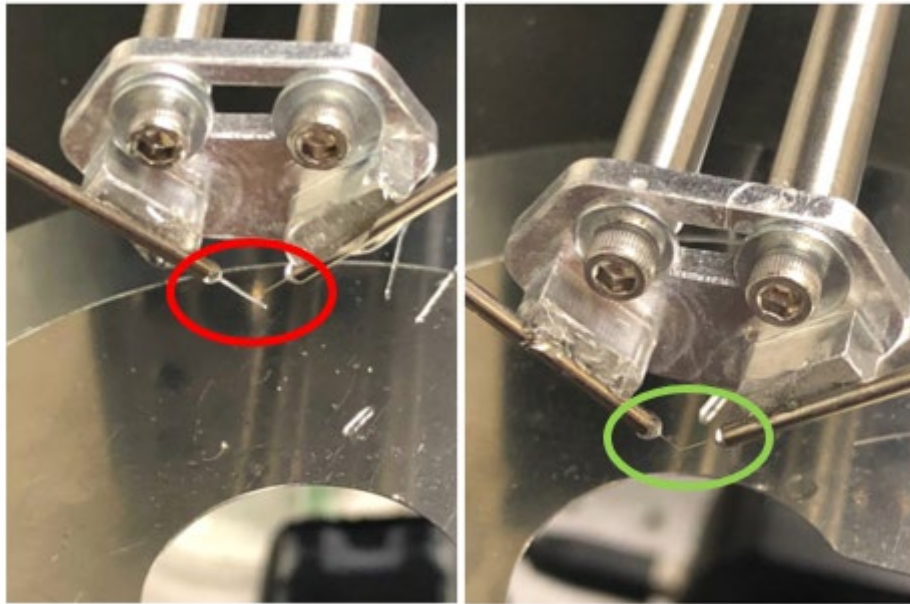


Figure 2-5: Fiber tips with creep (left) and without creep (right).

2.2.4 Common Board Design

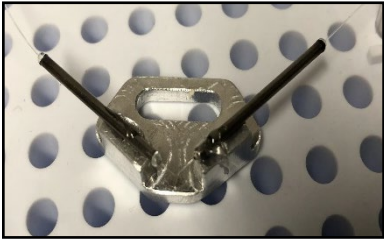
To measure the mechanical brain properties, we need a new experimental setup that is different from the optical trapping of beads setup. Relating to potential applications of this tool, a smaller design that is more compact is desired. If working on a sensitive, precise area of tissue, a smaller tool will allow for a more non-invasive surgery or procedure to be conducted. Therefore, we introduce a common board, whose goal is twofold.

- 1) To minimize the size of the board to increase its portability.
- 2) To measure the sample using a standardized device that does not require deep manipulation of the sample.

Transferring the DFOTs to a common board - creating a MFOT - is required to achieve these goals. We can then equip this MFOT onto our new mechanical stiffness measurement setup, or other measurement setups, to conduct experiments on biological tissues.

For the first iteration of the common board, it was unable to fit between the clamps on the alignment module and reach the fiber tubes due to its size. In order to fit the board under the alignment module, the second iteration of the common board was designed by Yao Shen, a Ph.D. student in the Optomechanics Lab. His new design conforms to the size restraints imposed by the aforementioned mechanical clamps. Hence, it was tested and verified as a part of our new fabrication method. Table 2.1 shows the full comparison between the two designs. The success rate of MFOT fabrication increased from about 50% to 75% with the incorporation of the modified fabrication method and the new common board design under a sample size of four attempts. This success rate increase is only with regards to problems being fixed by our method changes; for example, breaking a fiber during alignment is not considered, as we were not trying to solve this problem with our modifications. Ideally though, breaking a fiber would not occur.

Table 2-1: Comparison between the old and the new common board.

	Old Common Board	New Common Board
Design	 A photograph of the old common board, which is a rectangular metal plate with three circular holes and two long slots. It is shown with two black fiber tubes inserted into the slots.	 A photograph of the new common board, which is a smaller, more compact metal plate with a central hole and two long slots. It is shown with two black fiber tubes inserted into the slots.

Dimension (Length*Height*Width - Inch)	1.97*1.10*0.24	1.04*0.65*0.11
Pros	<ul style="list-style-type: none"> - Ability to trap beads - Good portability - Inexpensive - Securing with the three screw options is solid 	<ul style="list-style-type: none"> - Ability to trap beads - Good portability - Inexpensive - Smaller in size than old design - Easier to fabricate board - More consistent results noticed
Cons	<ul style="list-style-type: none"> - Not ideal size given our desired setup - Manufacturability - Harder to fabricate the board itself 	<ul style="list-style-type: none"> - Manufacturability - Slot for screws instead of screw holes

2.3 Experimental Setup of Modular Fiber Optical Tweezers

After preparing a modular system using our modified fabrication protocol, the system (common board in schematic) was integrated into the experimental set-up designed by Dr. Chaoyang Ti from the Optomechanics Lab. This set-up follows the schematic seen in Figure 2-6 below. Light is propagated from a fiber-coupled 974nm laser diode (AC 1405-0400-0974-SM-500, Eques) into a 3dB coupler, C1, (22-12798-50-23162, Gould Fiber Optics), as shown from stage LD to C1 in the system schematic. Each output of coupler C1 goes to another 3dB coupler (C2 and C3, respectively). The purpose of these two couplers is to split the light beams to the

trapping fibers (the red lines in the blue circle) while also giving the light reflected off the trapped particle a guide that leads to the balanced photodetector (PD) optical inputs (PDB450C, Thorlabs; PD1 and PD2). The bandwidth of the PD is 150 MHz which defines the bandwidth of our setup; to increase bandwidth, a different photodetector could be chosen. The signals collected by the PD are transmitted to a DAQ Box (NI USB-6361) which was connected to our lab's computer. ISCapture imaging software is used to monitor the experiment and view our sample under the objective lens. Fibers used in this experimental setup are SMF28 with an operating wavelength of 980 nm.

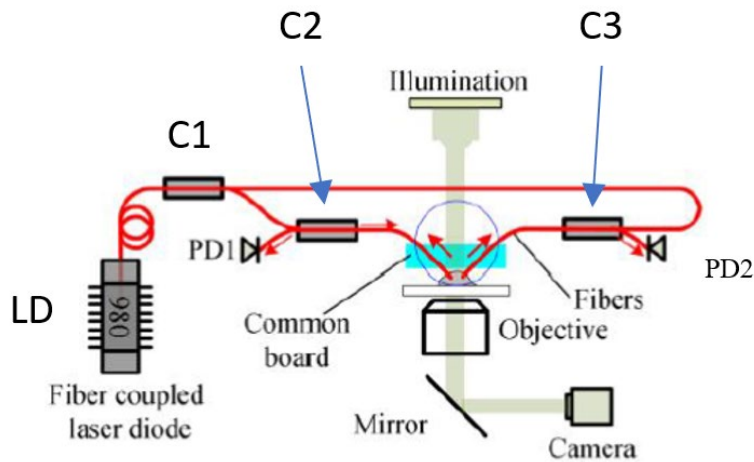


Figure 2-6: Schematic of Experimental Set-up of MFOTs [51].

2.4 Brain Experimental Setup and Working Principles

To achieve optical trapping on a biological tissue and to be able to observe it simultaneously, a three-component setup was built. This setup is comprised of a microscope module, an optical tweezer module, and a sample platform. The microscope module allows us to control the objective lens and thus view field that helps us facilitate optical trapping; the optical tweezer module controls the orientation and position of the MFOT that will provide the optical

trap; and the sample platform is used to hold our biological sample in place. Each module and its components are further discussed in the following sections.

2.4.1 Microscope Module

The microscope module allows us to maintain fine control of the microscope observation orientations and illumination locations. Through various orientation tests and combinations of objective lenses, it was determined that there are two viable ways to arrange the placement of sample, lens, and light source. Figure 2-7 below displays the two configurations.

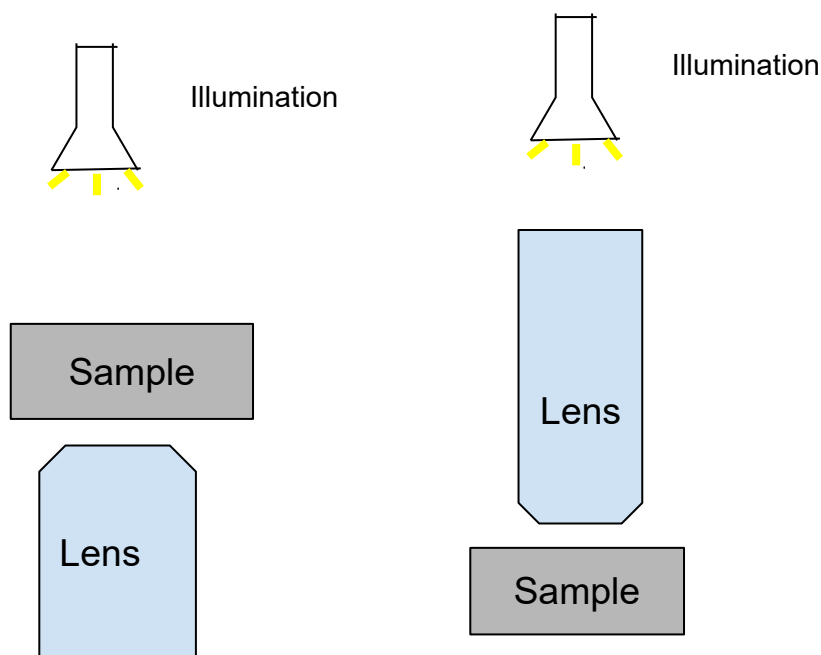


Figure 2-7: Microscope configuration A (left), configuration B (right).

Configuration A on the left is an inverted microscope setup. The light source illuminates the sample from a different side of the sample as the lens views the sample. Its advantage is that there is ample space above the sample for the optical tweezer to function. There will be no obstruction between the lens and the sample, so the small working distance of the objective will not impose spatial limitations on the optical tweezer setup. This is also the setup that we used in

the fabrication process for the DFOTs and MFOTs (see Appendix A). However, the lens observed the sample from the bottom, thus the light must penetrate through the biological sample for the microscope to collect light. This is the biggest restriction, as the sample must be sliced to a thickness of around 1mm to allow sufficient light to pass through. Additionally, to simulate measuring the mechanical properties of biological tissue, it would be unreasonable to assume tissue to be always thinly sliced and geometrically uniform on the surface - as such maneuvers will no longer be non-invasive. This configuration is also not ideal for outside-lab tests and experiments; if the system is being used to test stiffness of brain tissue in a patient, it is impossible to look from within the brain in an outwards radial direction with an objective.

Configuration B on the right is an upright microscope setup. The drawback of this setup is the working distance of the microscope - which limits the size and movement of the optical tweezer that would have to operate in between the sample and the lens. To correct this problem, we decided to use a 20X Mitutoyo Plan Apo Infinity Corrected long working distance microscope objective. This objective has a 20mm working distance that gives greater space to move the common board into the sample without hitting the lens. This setup is also able to eliminate the illumination problem mentioned previously and resembles a real-world measuring probe on the surface of a tissue more closely.

Configuration B was thus adopted for its many benefits over configuration A. The objective is fixed onto a set of optical stages, including translational stages in the x-direction and z-direction and a rotational stage for facilitate angular adjustments in the XY plane. Figure 2-8 below shows the microscope objective setup. The video output is recorded by a camera and exported to a computer, allowing us to monitor the movement of the objective. The light source is connected to the microscope objective.

2.4.2 Optical Tweezer Module

A pair of MFOTs is imperative to achieve optical trapping in biological samples. To allow sufficient degrees of freedom, several fine-tuned adjustment stages are used. These include translational stages in X-direction, Y-direction, and Z-direction, and a horizontal rotational stage to facilitate angular adjustments in the XY-plane. Figure 2-8 shows the optical tweezer module.

2.4.3 Sample Platform

Due to the sensitive nature of our desired brain experiment, a small amount of displacement or vibration of the sample will interfere with the performance of the optical trap. To minimize the external disturbance, the experiment will be executed on a vibration controlled optical table. Given the geometric position and the distance between the sample and the objective lens, the objective lens and the 3-D stage with the common board need to be lowered to make the brain sample observable. The brain sample will be placed on a glass slide. To get more degrees of movement of the sample, two unidirectional (X and Y) moving stages will also be placed under the glass slide. Figure 2-8 below shows the complete brain experiment setup.

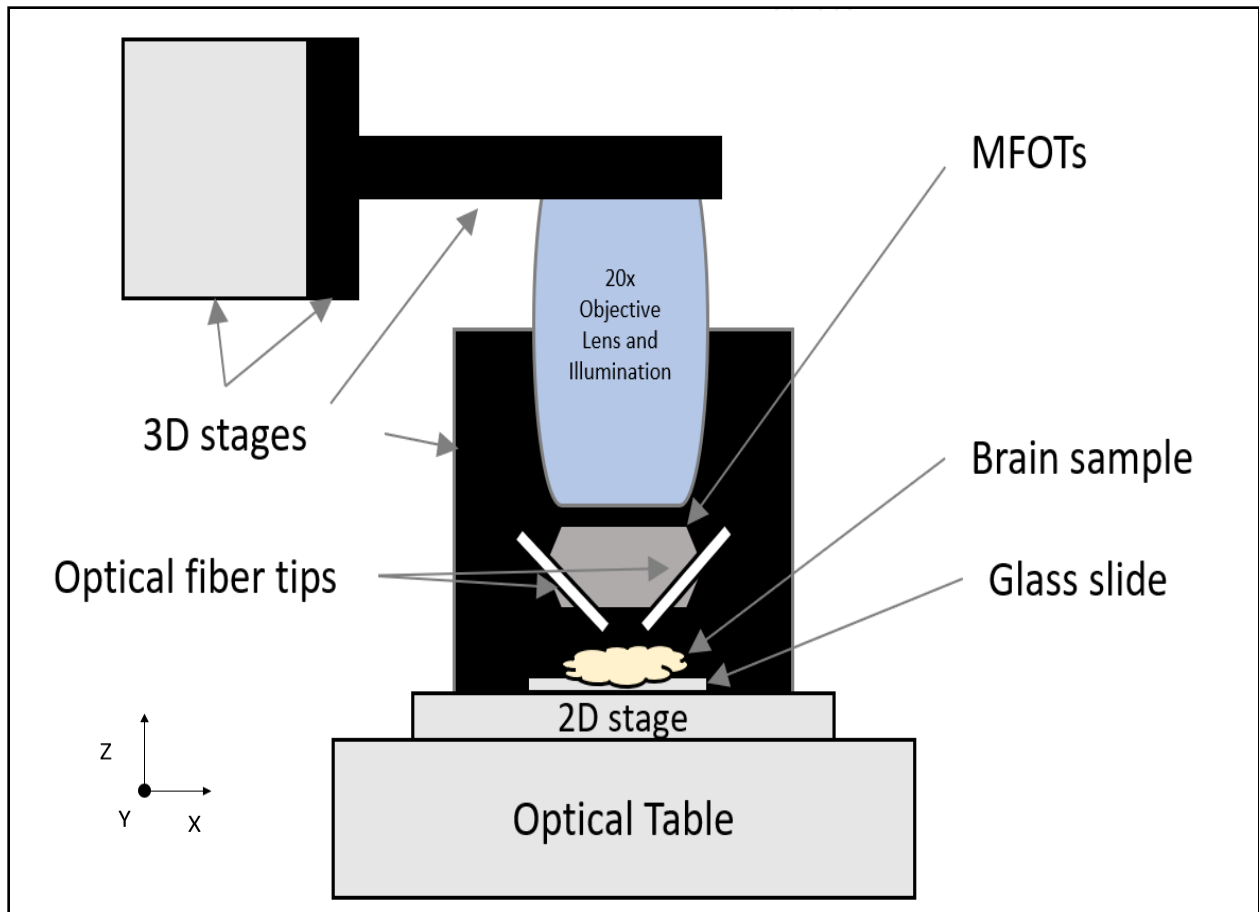


Figure 2-8: Complete Sample Platform Setup.

2.4.3.1 Adapter during experimentation

While conducting preliminary experiments, it was discovered that the screws on the back of a backing plate that held up the optical posts for the common board were too small for the holes they were inserted into (see Figure 2-9). This made the common board non-stationary and hard to control. Because of this movement, the backing plate, when moving in the negative z-direction would touch the microscope platform before the optical tweezers could trap a bead. With this discovery, an acrylic adapter piece was fabricated. The addition of the adapter plate solved the aforementioned problem.

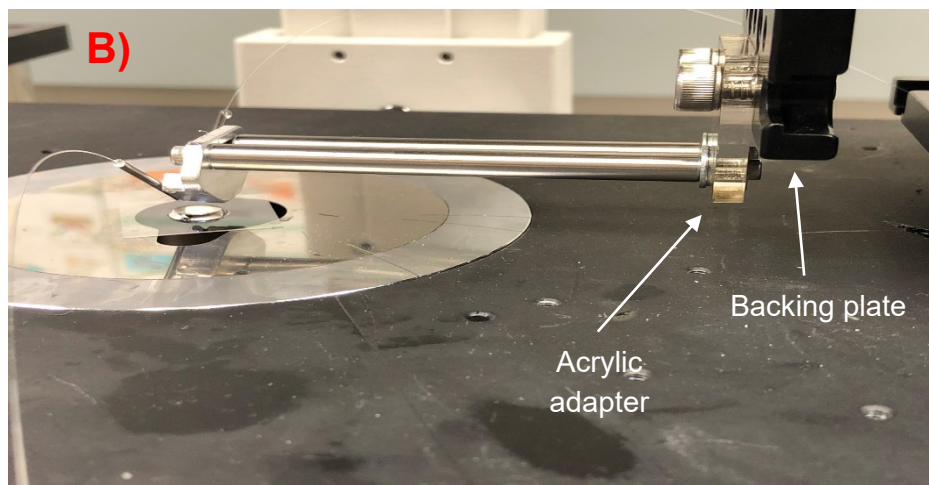
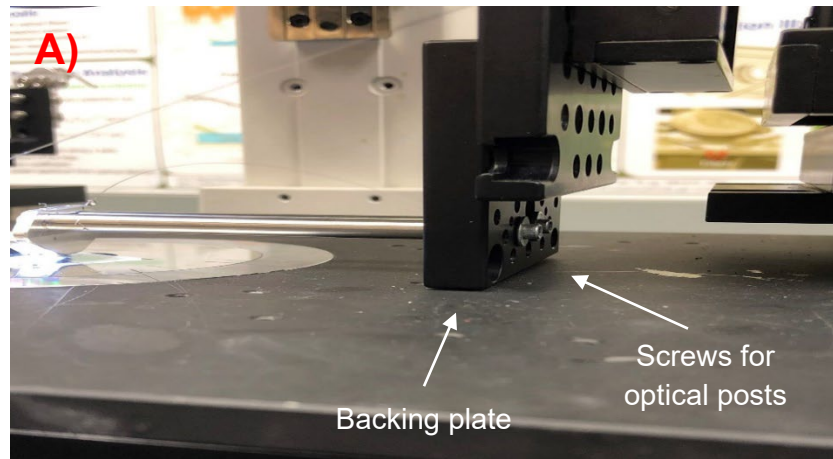


Figure 2-9: Old system with limited vertical travel range (A); New acrylic adapter piece allows greater vertical travel range (B).

2.4.4 Assembly

The microscope module, optical tweezer module, and sample platform together make up the brain measurement setup. The microscope module has one rotational and two translational degrees of freedom; the optical tweezer module has three translational degrees of freedom; the sample platform has two translational degrees of freedom. Combined together, this assembly can accommodate the needs necessary for an optical trapping experiment in a brain sample.

After optimizing the MFOT system design, fabrication methods, and experimental set-up, we can proceed with optical trapping experiments in biological samples. In the next chapter, we will discuss governing equations that allow us to calibrate mechanical stiffness of biological samples, as well as our data collection methods and post-processing of the data to realize meaningful results.

Chapter 3. Optical Trapping Experiments: Fundamentals, Procedure, and Data Analysis

The experimental procedure governs how we conduct all experiments to ensure consistent results. In addition, should anyone in the future want to execute similar experiments or improve on our method, they can cite this procedure. In this section, the brain sample preparation method, governing equations that allow us to calibrate stiffness measurements, and data processing will be discussed.

3.1 Governing Equations of Power Spectrum Analysis

To calibrate the optical trap generated by the optical tweezers, the power spectrum method was used [108]. Spring forces are defined as the forces being applied from the optical trap and the trap's surrounded medium. In this trap, the bead experiences confined Brownian motion for which a single-sided power spectrum can be generated. The Brownian motion is modeled by the Einstein-Ornstein-Uhlenbeck theory, which is described by the following equation.

$$m\ddot{x}(t) + \gamma_0\dot{x}(t) + \kappa x(t) = (2k_B T \gamma_0)^{1/2} \eta(t), \quad 3-1$$

where $x(t)$ is the Brownian particle's trajectory, γ_0 is the friction coefficient of the bead, m is the particle's mass, $-\kappa * x(t)$ is the harmonic force from the optical trap, and the right-hand side term is a random Gaussian process. The process models the Brownian motion occurring at the absolute temperature of the trap T . The friction coefficient $\gamma_0 = 6 * \pi * \mu * R$ is the Stokes drag coefficient that describes the drag force exerted on small spheres with minuscule Reynolds numbers, where μ is the viscosity of the medium and R is the radius of the trapped bead. A power spectrum representative of the trapped particle's displacement can thus be generated after Fourier transforming the time domain signal to the frequency domain using the following equation [25]

$$S_{xx}(f) = \frac{k_B T}{\pi^2 \gamma (f_0^2 + f^2)}, \quad 3-2$$

where k_B is the Boltzmann constant, T is absolute temperature, γ_0 is the Stokes drag coefficient, and f_0 is the corner frequency. The corner frequency, f_0 , is representative of the experimentally fitted curve and is integral in calculating the optical trapping spring constant defined by the following equation:

$$k = 2 * \pi * \gamma_0 * f_0. \quad 3-3$$

The spring constant of a cell or biological medium can be related to the generated optical trap. In particular, the force exerted on the micro-sphere by the optical trap is approximately the same as the force exerted on the micro-sphere from the biological medium, assuming the micro-sphere is moving against the biological medium. In mathematical representation, this is equivalent to equation 3-4 below.

$$F_{Trap} = k * \Delta x_{Trap} = F_{Biological} = k_{Biological} \Delta x_{Biological} \quad 3-4$$

F_{Trap} is the force exerted from the optical trap onto the micro-sphere; Δx_{Trap} is the distance between the center of the optical trap and the center of the micro-sphere; $F_{Biological}$ is the force exerted on the biological medium by the micro-sphere; $\Delta x_{Biological}$ is the distance the micro-sphere is moved along the biological medium; and $k_{Biological}$ is the spring constant of the biological medium. For our MQP's goal, $k_{Biological}$ will be the spring constant, or mechanical stiffness, of white and grey matter of bovine brain tissue.

3.2 Elastic and Shear Moduli Calculation

The power spectrum method provides the spring constant of the trap, but in order to compare to other works and published data we need to obtain elastic modulus and shear modulus values. For our MQP, we decided to use the indentation method outlined in Budday et al's study to find the elastic modulus of the brain tissue [17]. Budday et al used this method that was originally developed by Oliver and Pharr [107]. The indentation method defines an effective elastic modulus using the following equation:

$$E_{eff} = \frac{\sqrt{\pi}k}{2\sqrt{A}}, \quad \mathbf{3-5}$$

where E_{eff} is the effective elastic modulus, k is the spring constant, and A is the projected contact area under the indenter – for our circumstances, the contact area is the bead because the bead is being pushed into the brain tissue. Budday et al then declare $A = \frac{1}{4}\pi d^2$ for a circular contact area; for us, since the bead contact area is comparable to the largest cross section of the bead itself, we can also make this substitution, deriving equation 3-6.

$$E_{eff} = \frac{k}{d} \quad \mathbf{3-6}$$

The common assumption of incompressibility is then adopted (Poisson's ratio (ν) = 0.5), as the testing method does not quantify compressive features of the brain tissue. Through substitutions, Budday et al arrive at equation 3-7 that equates the elastic modulus of the sample to the spring constant and diameter of contact. Equation 3-7 will be used to find the elastic modulus of the brain sample.

$$E_{\text{smp}} = \frac{3}{4} \frac{k}{d} \quad \mathbf{3-7}$$

Using the elastic modulus and Poisson's ratio, the shear modulus, G , of the brain tissue can be calculated using equation 3-8. The brain tissue is assumed isotropic due to the micrometer scale of the experiments and little contact area between the bead and brain tissue.

$$G = \frac{E}{2(1 + \nu)} \quad 3-8$$

3.3 Data Processing

To collect data from the DAQ board, a LabVIEW program (tapering_no_home_new_7_PSD and PD together_good09282016.vi), which was created by Dr. Chaoyang Ti in his previous work [26], was used. This program connects to three channels of the DAQ board and records the signal from both inputs of the PD, as well as the difference between the two signals - RF signal. This difference is then amplified by the PD so it can be read by the DAQ. While data is being recorded, the program plots these signals, as well as a power spectrum, both in the time domain. To quantify the corner frequency of the trap, a Lorentzian transform on the RF signal from the PSD must be carried out, where each signal was recorded over a 5 second period of time under a sampling frequency of 10kHz. A Fourier transform from time domain signals to frequency domain signals is carried out using an intermediate MATLAB code called "Labcode.m"; the code requires the user to import the .txt file from the LabVIEW code and will automatically generate the frequency domain signal when run.

In the actual data acquisition and analysis, we gathered a set of data from regular trapping activity. Once the bead was trapped in the water solution stably, we opened the LabVIEW code and started to record position data in the time domain for approximately 10 seconds. During the recording process, we did not move the trapped bead so as to achieve relatively un-noisy data. Given the noisy data output from LabVIEW, we used another the MATLAB code (psfitting_real_lin5.m) to take the frequency domain signal and block it to transform the

exponential distribution to the Gaussian distribution, as well as to filter out noise and curve fit the data. Blocking also cuts down the number of points fitted by averaging, thus helping to reduce the noise in the fitting. An outlier filter was added to this code that can delete abnormally large recorded data that are not from the experiment – i.e. a surge from an outlet. It is up to the user to change the cutoff of the filter. More on this will be discussed in Chapter 4. Finally, a Lorentzian was applied by this code for the domain of .1-50Hz - optimized on an experimental basis - for which the spring constants were generated. The code output includes, among other parameters, the desired corner frequency and spring constant, allowing us to quantify the characteristics of the optical trap and medium.

3.4 Brain Sample Preparation

For our experiments, we used block of bovine brain donated from a local slaughterhouse. Each block was sliced thinly to a thickness of around 1mm using an exacto knife. Brain samples were prepared on 25x25mm² coverslips, where two drops of bead solution (prepared in the same way as in the fabrication protocol) were dropped on the sample. The sample was then left undisturbed for about 10 minutes to let the beads absorb into the sample due to gravitational forces. Not all beads will be slightly under the brain surface, but beads that appear close to the surface will be used for experimental purposes. This method mirrors that described in our lab's previous work on fiber optical tweezer force measurements in a polyacrylamide gel compartment [26].

3.5 Summary

With a proper experimental setup, a set of equations that governs the Brownian motion of the microspheres, equations modelling the optical trap generated by the optical fiber tweezers, a procedure for collecting and processing data, and a proper methodology for running our

experiments, we can calibrate the desired spring constant. By applying the previously discussed methods, and the experimental protocol for brain experiments in Appendix B, we are able to obtain accurate stiffness measurements of white and grey matter in brain tissue. With our collected data, we will be able to provide more accurate mechanical stiffness of brain tissue measurements that will bridge the gap in past and current brain property research.

Chapter 4. Results and Discussion

After fabricating the modular fiber optical tweezers, optical trapping experiments were first carried out on microspheres in water. This type of experiment was intended to calibrate our understanding of optical trapping, allow us to get familiar with trapping using the MFOTs, and go through the data processing procedure. This prepared the team for more complicated experiments where attempts were made to trap microspheres in a brain sample to quantify the mechanical stiffness of the brain tissue. In this section, collected and processed data from both beads in water experiments and beads in brain tissue experiments will be analyzed; after, their implications and physical meaning will be discussed.

4.1 Criteria to Determine Good Trapping Experiments and Faithfulness of Measured Data

After obtaining nearly one hundred power spectrum data sets, it is essential for both the authors and the readers to tell what data are qualified as “good data” and hence deserve detailed analysis and discussion. In the section, we will establish and elaborate on the features to define a good data set so that future users could execute similar experiments with hopes of good results. Typically, to achieve a good quality experiment, preparation of hardware and its function is mandatory. The criteria for the prerequisite of a successful bead-trapping is twofold:

- a) Existence of a 3D trap and the quality of the power spectrum data.
- b) Misalignment of light spots and spot size.

Existence of a 3D trap and the quality of the power spectrum data

The 3D optical trap itself is a potential energy well created by the interactions between the laser beams and a physical particle. As a result, the 3D trap itself is invisible, but the existence of the 3D trap can be visualized by monitoring the trapped particle. The most important feature to

look for, arguably, is that the bead is trapped in 3-dimensions during experimentation. Although experimental results can be obtained from a 2D trapped bead (on a substrate surface), the experimental results cannot be well modeled by the Lorentzian function, because of the existence of additional interactions between the bead and substrate. Therefore, a 3D trap is preferred for power spectrum data collection, and it also promises more accurate Lorentzian fitting. It is important to note that a signal keeps being generated by the LabVIEW code even if a bead is not trapped, as ambient light can be collected by the trapping fibers. This signal does not have any physical information about the trapping and should be overlooked. As a result, visually seeing a trapped particle move on the computer monitor is necessary before the data collection, to ensure the collected data can be described by the model in Section 3.1 and be fitted properly.

Misalignment of light spots and spot size

Since ensuring a 3D trap is generated for data acquisition, inspecting the light spots from the fiber tips is essential. If the light spots are misaligned, unwanted rotation of the particle being trapped could occur, generating unwanted noise in the collect light by the two optical fiber tips (see Appendix A for more information on how to properly align the fiber tips). On top of light spot alignment, the size of the spots is key in a meaningful experiment; thus spot size should be noted. If one fiber tip's light spot is considerably bigger than the other, there will be an uneven distribution of power over the bead that is trying to be trapped. This imbalance of force can cause particle rotation and create noise in the acquired data (see Appendix A for more information on light spot inspection).

After making sure hardware are all well prepared and the functionality of the MFOTs is confirmed, next stage is to collect the power spectrum data to determine the Lorentzian fitting curve, as well as the corner frequency and the spring constant of the trap. To process the data to

what we have seen in Dr. Ti's publication - our base comparison - the criteria of processing the data is also twofold:

- a) Observation and elimination of outliers in a data set.
- b) "Noise" cancellation.

Outliers in raw and processed data

Once a high-quality experiment has been executed, there are a number of key features to take note of in the raw data and processed data MATLAB outputs. The first feature to note is the absence of outliers in the collected data. As mentioned in Section 3.3, a singular outlier can completely skew the fitting of the data (see Figures 4-1 A and B). On a similar note, an outlier could make the collected data appear unreliable when in reality there is a good set of data hidden behind it. Such outliers can include surges from an outlet or external macro-vibrations; the outlet outlier corresponds to a power spike at around 60Hz - the utility frequency of the AC current through an electrical outlet. If a rather large outlier is seen, the newly added filter in the MATLAB code can be modified to remove this point, thus adjusting the fitting of the data.

Furthermore, a clear -2 slope in the tail end of the Lorentzian-fitted plot can be seen in a good data set. The slope of the power spectrum tail will be -2 in the logarithmic scale of both axes when frequencies collected are much greater than the characteristic corner frequency of the trap [51]. A different slope for higher frequencies indicates that the fitting scheme may not be entirely correct under the experimental circumstances, or the experiment itself was not carried out correctly and should be re-run (see Figure 4-1A).

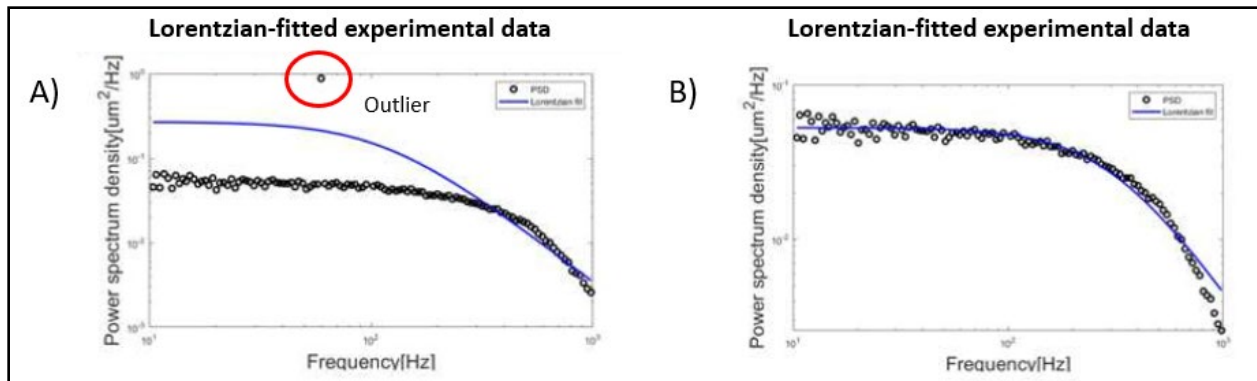


Figure 4-1: A) Lorentzian-fitted experimental data with outlier; B) Lorentzian-fitted experimental data with outlier removed.

Noise in the fitted data

Finally, the noise in the collected data should be noted. Noise can indicate an unstable trap or testing environment that may not be visible to the eye during experimentation. From the raw data, it is hard to see abnormal noise, as in a single experiment over 100,000 data points can be collected and displayed at the same time. The blocking functionality in the MATLAB code averages a set number of the points from the raw data together, reducing the total points displayed in a plot. The result of applying this method is a plot with reduced data noise for which the fitting can be applied effectively. Although the blocking functionality in the MATLAB code reduces some noise, relatively large noise after blocking is an indicator that either the block was too small and needs to be increased or the data itself is too noisy and blocking will not be effective (see Figure 4-2). In the latter case, the collected data and experiment itself are not of high quality and should be repeated. For the rest of this chapter, analysis will be carried out only for successful systems that were deemed high quality based on the criteria previously established.

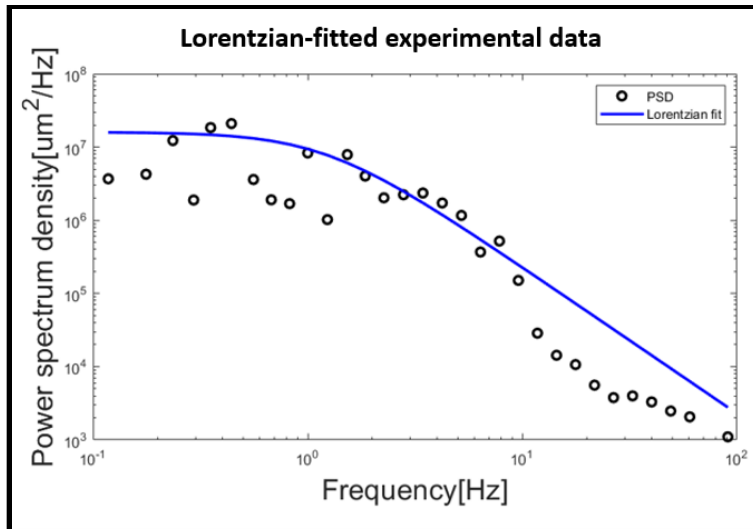


Figure 4-2: Excessive noise in the cropped data.

4.2 Experimental Results of Polystyrene Bead Trapping in Water

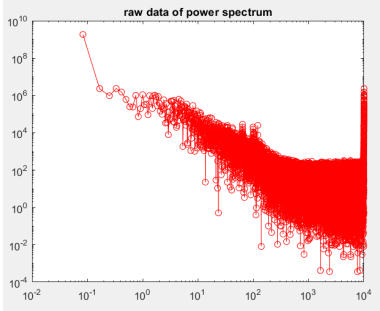
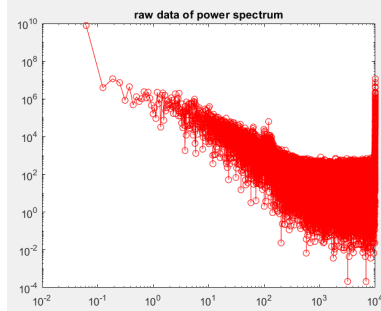
The first sets of data we collected were from experiments where 15.45-micron diameter beads were trapped in a surrounding medium of deionized water. Water-based experiments were carried out before more complex, brain-based experiments to allow us to familiarize ourselves with the experimental methodology. Over the course of the project, many water-based experiments were carried out, yielding a wide range of experimental results and helping us improve the quality of our experimental outcomes. The opportunity was also taken to collect experimental data during multiple MFOTs fabrication attempts. Some of the data we collected and fitted satisfy the criteria listed in the previous section and will be analyzed in more depth in this section. Due to the sheer number of experiments run, we will only review a select few successful experiments.

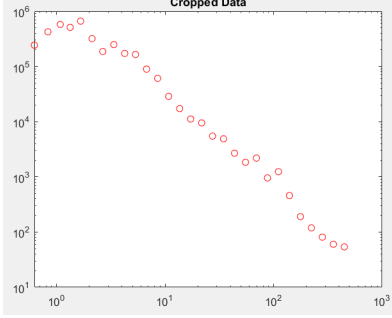
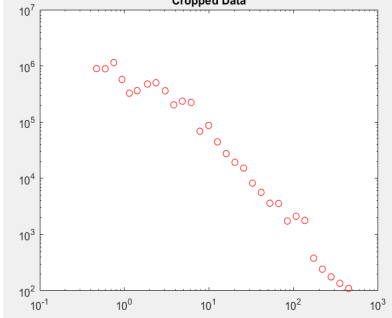
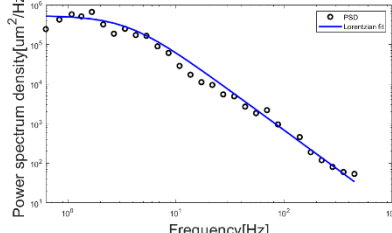
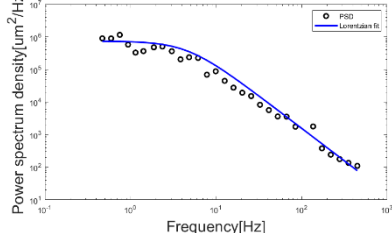
4.2.1 Meaningful Results from Water Experiments

Using the experimental methodology and data acquisition codes discussed in Chapter 2, many data sets were collected. For each set, the MATLAB codes mentioned in Chapter 2 were

run, providing raw displacement power spectrum, cropped displacement power spectrum, and Lorentzian-fitted frequency domain curves. Two examples of typical graphs and results from good quality experiments can be found below along with a discussion of their implications. For the Lorentzian-fitting curves, we discretize the domain of the plots from around 0.1 Hz to 100 Hz which is close to the natural frequency of the system. These experiments were run on the same trapped bead over the course of around 15 minutes.

Table 4-1: Results of experiments #1 & #2 in deionized water.

	Experiment #1	Experiment #2
Input current from the laser diode	400mA	600mA
Output power from each fiber tip	23mW	38mW
Raw power spectrum data		

Cropped power spectrum data		
Lorentzian fit of the cropped data		
Corner Frequency (Hz)	3.5869 ± 0.34354 Hz	4.6032 ± 0.3206 Hz
Spring Constant (pN/micron)	2.9207 ± 0.27973	3.74825 ± 0.26106

For two of the successful experiments mentioned in the table above, a 15.45-micron diameter polystyrene bead was trapped in all three dimensions with different power input from the laser diode and output from each fiber tip. Following the general guidelines for good quality experiment mentioned Section 4.1, we carefully controlled the light spots, alignment of fiber tips, as well as data processing. We can conclude the results of both experiments are precise base on the fact that Lorentzian fitting is almost directly on top of the experimental data points (see Lorentzian fit of the cropped data in Table 4-1). Additionally, there is a flat component to the fitting in the lower frequency domain and a -2 slope from the corner frequency to the higher frequency domain. From the magnitude of the spring constant, we can further conclude that the spring constant of the medium, deionized water.

4.2.2 Discussion

The results from the previously discussed experiments are consistent with the theory and make intuitive sense, as with a higher power input we expect a larger optical trapping spring constant to be generated. To expand on this expectation, more data from our numerous experiments can be combined to find the dependence of optical trap spring constant on input power in a DI water medium. To generate the experimental dependence seen in Figure 4-3 below, we trapped a 15.45-micron diameter polystyrene bead and modulated the power input from the laser diode. The same bead was trapped during the entire process. Power was modulated from 300mA to 1200mA and then back down to 300mA, in increment of 100mA, thus providing two sets of data per power rating. To create a dependence plot, corner frequencies and spring constants for each power rating were averaged together and plotted against input power from each fiber. As discussed previously, we expect a larger optical trapping spring constant as we increase input power to the fibers. Figure 4-3 below verifies this expectation.

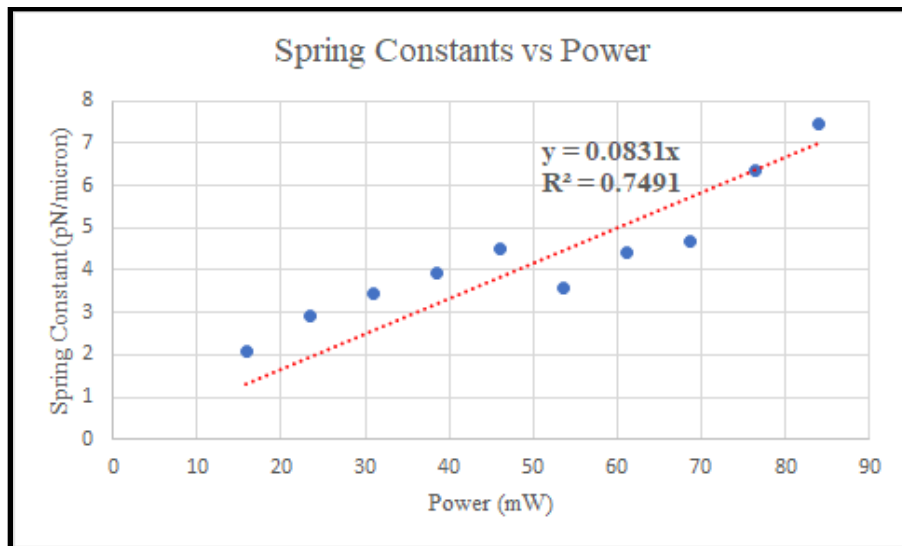


Figure 4-3: Spring constant dependency graph with trendline going through the origin.

The variation in data from about 53mW to 68mW can likely be explained by the temperature effects of the light inputs to the polystyrene bead. For the data points below the trendline in the Figure 4-3 above, before running the LabVIEW code to collect data, we let the trap sit undisturbed for a little while. This could have generated localized heating on the polystyrene bead surface. With more energy in the bead, the more movement the optical trap sees and thus the lower spring constant is found. It should also be noted that at around 53mW of power, we moved the MFOTs to verify the trap was still present; this may have influenced the spring constant from the optical trap. Other than these three different points, a near constant slope was calculated for the effects of input power on spring constant.

A key factor that contributes to these correlation plots is the separation distance between the two trapping fibers on the MFOTs. A smaller separation means that there is less distance for reflected light from the polystyrene bead to travel in order to be coupled back into the trapping fibers; thus more light is collected by the trapping fiber and a stiffer optical trap is generated. However, to shine the light onto the bead, we have to lower the tips due to higher interference between the tips and brain. By doing so, the bottom corner of the tip will stick into the sample, hence might cause potential damage to the MFOTs. Likewise, a larger separation means that there is more distance for reflected light from the polystyrene bead to travel in order to be coupled back into the trapping fibers; thus less light is collected and a less stiff optical trap is generated. Since the interference between the fibers and brain is lower, the corner of the tips won't touch the sample (see Figure 4-4 below). For the MFOTs used in collecting Figure 4-3's data, the trapping fiber separation was approximately 60 micrometers - almost half the fiber cladding diameter of 125 micrometers, which is the ideal separation. Given that fiber separation is such an influential factor, many iterations of the input power versus spring constant can be generated by changing this alone.

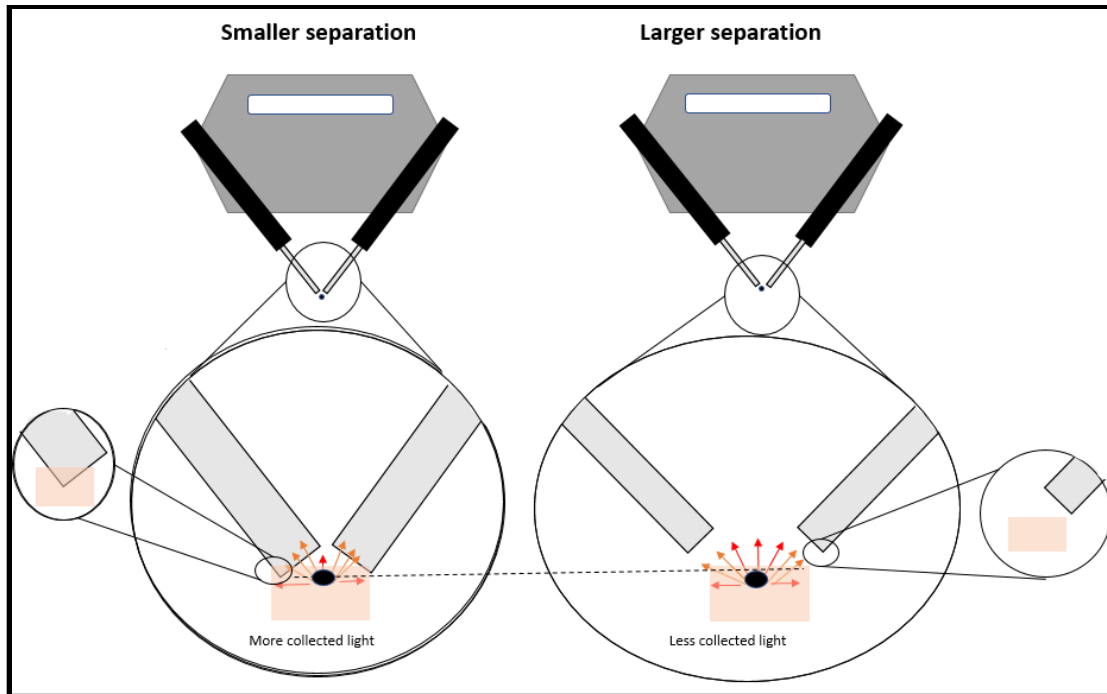


Figure 4-4: Effects of trapping fiber separation on coupled, reflected light. (Red arrows indicate uncoupled, reflected light; orange arrows indicate coupled, reflected light; the dotted line indicates reference height; the beige rectangular object indicates part).

4.2.3 Comparison to Previously Published Results Using Similar Systems

To validate the data we obtained from our experiments, we used Dr. Chaoyang Ti's results as a baseline. In his published research, Ti uses a similar experimental procedure for collecting and processing data to that of what we used. The comparison between the MQP's result and Dr. Ti's shows that both experimental results reside in a similar magnitude (see Table 4-2), hence proving the consistency of the experiment. Although only one of our results is compared here, many of our other sets reinforce our observation.

Table 4-2: Comparison to known results.

	MQP Team's Result 1	MQP Team's Result 2	Dr. Ti's Results [51]
Corner Frequency (Hz)	4.60 ± 0.34	5.40 ± 0.34	4.92 ± 0.28
Spring Constant (pN/ μm)	3.75 ± 0.26	4.40 ± 0.28	3.89 ± 0.22

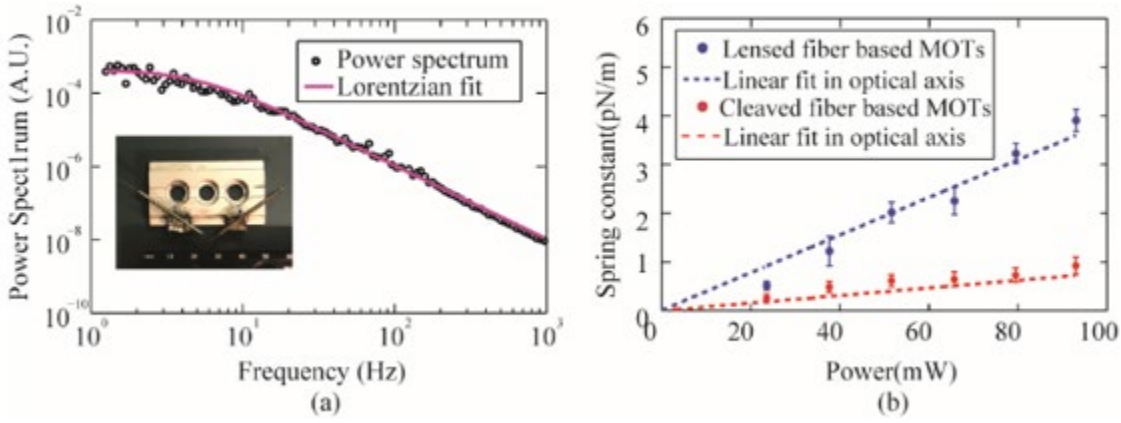


Figure 4-5: A) Dr. Chaoyang Ti's Lorentzian fitting for trapping a 15.45 micron diameter polystyrene bead in deionized water. B) Spring constant calibration as a function of power per fiber for lensed and cleaver fiber MFOTs [51].

In Figure 4-5 A, we can see that our results outlined in Table 4-1 in Section 4.2.1, especially the magnitude of the spring constant and the Lorentzian fitting curve, are comparable to those of Dr. Ti's. However, given the reasons mentioned in the previous section, parts of our experimental procedure likely differed from that of Dr. Ti's. As alluded to earlier, slight changes in experimental procedures or even setup of the MFOTs can lead to differences in collected and fitted data, which can explain some of the variation in our results compared to Dr. Ti's. Regardless of these differences, many of our experiments satisfied the general guidelines for a good quality experiment. Our results showed repeatability of the experimental procedure and stability of the

MFOTs. After proving the MFOTs is a reliable tool for measuring optical spring constants and after familiarizing ourselves with the system through various deionized-water-based experiments, we carried out trapping experiments on the more complex brain sample. Later, we will compare our obtained results from brain experiments to those from deionized-water-based experiments.

4.3 Results Obtained from the White Matter in Brain Sample Experiments

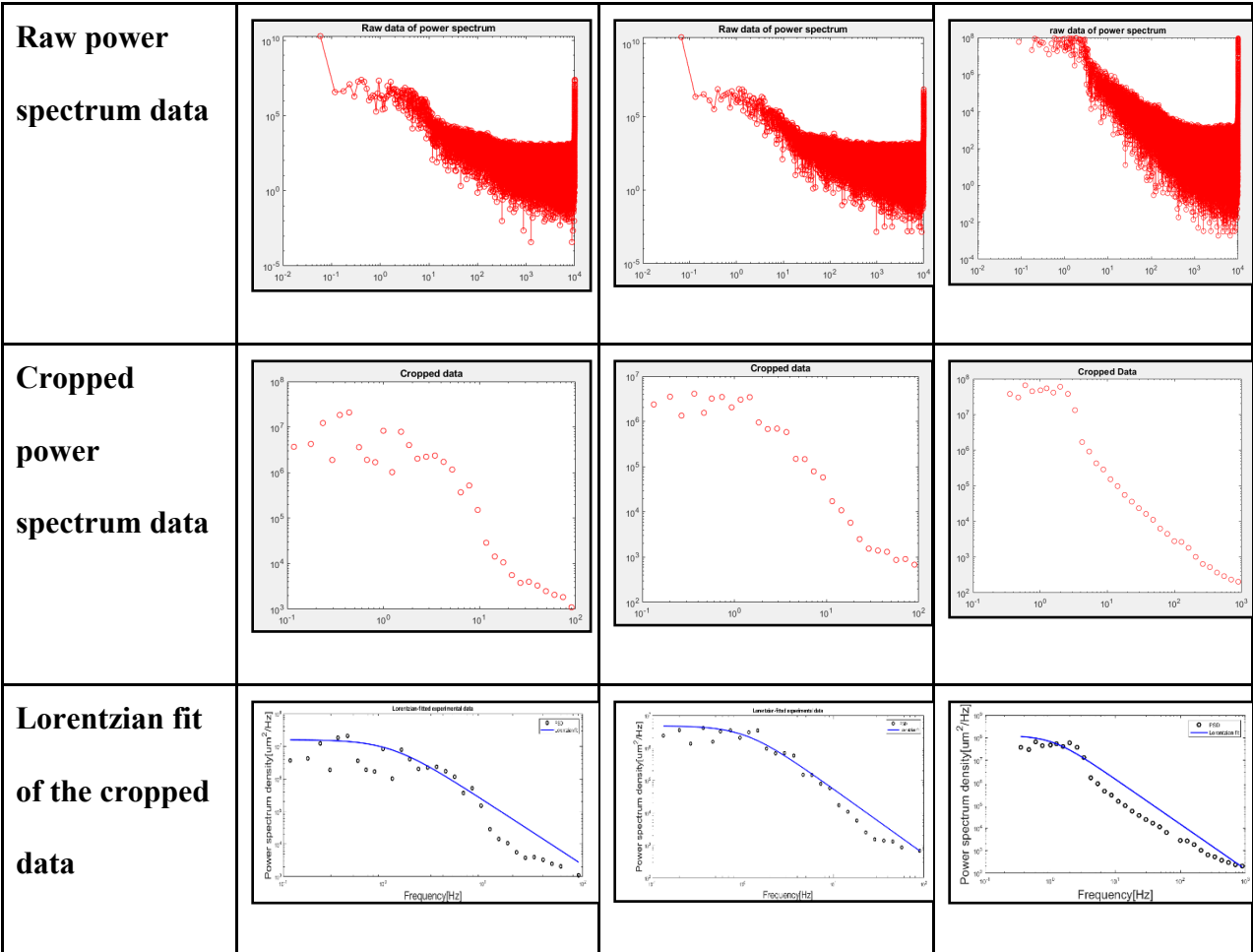
After numerous attempts to trap microspheres on the surface of the bovine brain sample, it was determined that meaningful data can be categorized into two main types, Type I and Type II. Much of the uncertainty the team has is due to the impairment of vision from the bead solution as it is dropped on the brain tissue surface; more about this will be discussed in the next chapter. For the following experiments, white matter of the brain was used for experimentation.

4.3.1 Type I Results from Beads-in-Water Experiments

Two common features from the data collected from brain sample experiments are a low corner frequency and a -2 slope at the higher frequency end of the Lorentzian fit, as described in Section 3.2.1. The figures in Table 4-3 display three sets of collected data that demonstrate such characteristics.

Table 4-3: Brain sample experiments - 1.

	Experiment #1	Experiment #2	Experiment #3
Current (mA)	1200-1	1200-2	1200-3
Power Output (mW)	83.8935	83.8935	83.8935



The fittings of these can be considered good per standards outlined in Section 4.1. Table 4-4 below summarizes the corner frequencies and associated spring constant results from the three experiments displayed in Table 4-3 above.

Table 4-4: Corner frequency and spring constant results from Type I data.

Experiment	Fc (Hz)	K (pN/micron)
1	1.1973 ± 0.12499	1546.7052 ± 161.4752

2	1.0691 ± 0.12638	1381.1742 ± 163.2664
3	1.8207 ± 0.13932	2352.1199 ± 179.9856

Type I results resemble those seen from water-based trapping experiments. Since clear microscope images are not available to us during brain experiments to judge whether the bead “trapped” was actually trapped on the surface of the brain, it is possible these data sets were collected when the targeted microsphere was trapped in the water above the brain surface. In addition, given the view from the low magnification 20X objective lens, we were unable to observe whether the bead was trapped or not (see Figure 4-6). In short, data sets of similar qualities could explain the close resemblance in terms of the optical spring’s performance. At the same time, not knowing the position of the bead makes us question the faithfulness of the optical trap and its data.

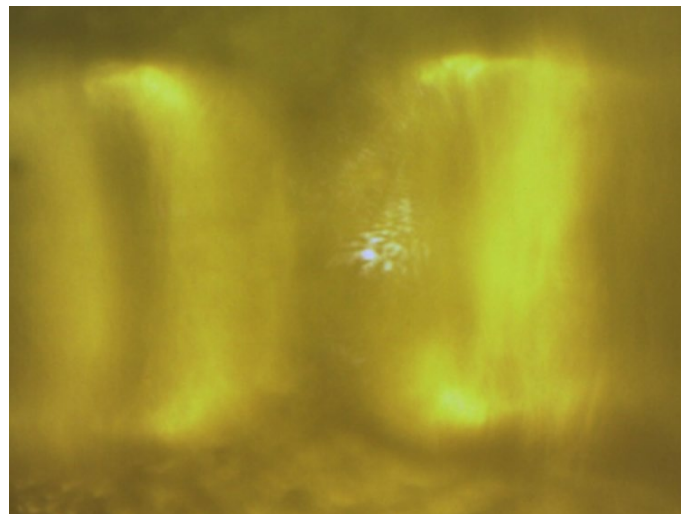


Figure 4-6: Vision of brain blocked by trapping fiber tips.

4.3.2 Type II Results from Beads-on-Brain Experiment

Another feature that was observed from many datasets was a secondary roll-off point. The red arrow in Figure 4-7 below shows a secondary roll-off corner, along with the plateau that was

missing from the Type I results. At lower frequencies, the data is more widely dispersed, of which we suspect is from external vibration in the laboratory room where these data were collected. At higher frequency ranges - 10Hz and onwards - the data is more condensed together and subject to less external noise. A higher roll-off frequency corresponds to a higher spring constant, which is intuitive when comparing the stiffness of brain tissue to water.

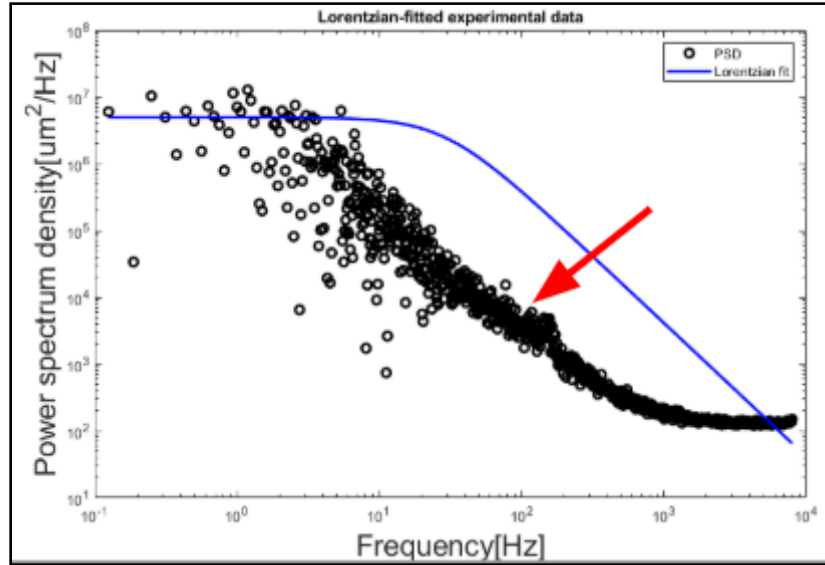
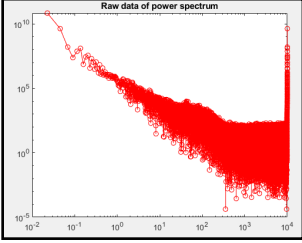
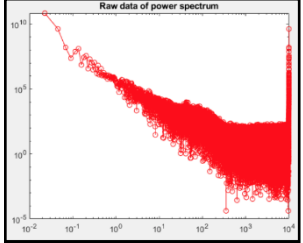
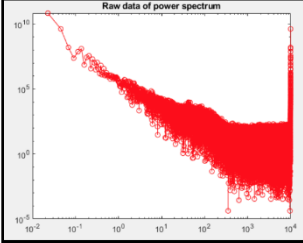
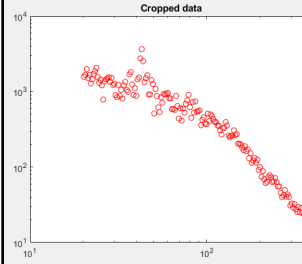
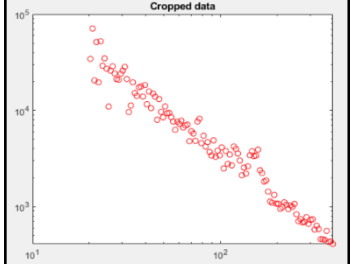
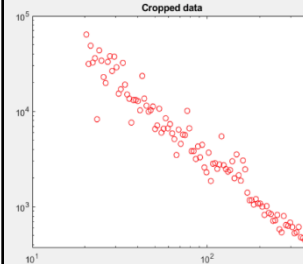
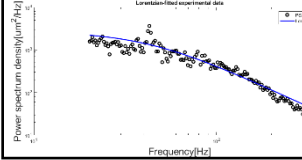
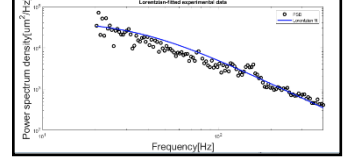
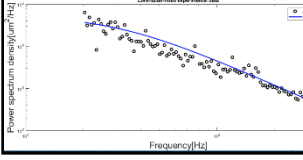


Figure 4-7: Secondary roll-off point at higher frequency.

After further analysis around these regions, a trend of higher corner frequency was observed in many sets of data. The fitting window - domain - of the next three sets of data displayed in Table 4-5 are all from 20Hz to 400Hz.

Table 4-5: Brain sample experiments -2.

	Experiment #4 (Good)	Experiment #5 (Unreliable)	Experiment #6 (Unreliable)
Current (mA)	700	1200-3	1200-4

Power Output (mW)	46.0685	83.8935	83.8935
Raw power spectrum data			
Cropped power spectrum data			
Lorentzian fit of the cropped data			

As we can see in the first column of Table 4-5 presented above, the data points are relatively close to the fitted Lorentzian curve. According to the criteria developed in Section 4.1, we can determine this data set to be accurate. In Section 4.4, we will be using this particular set of data to obtain elastic and shear moduli of white matter and comparing it to other known modulus measurements. Furthermore, the other two columns represent inaccurate data sets from brain experiments. The reason for classifying these sets as inaccurate are that there is an absence of the plateau in the low frequency domain, hence failing to be characterized as a good data set per our

criteria. Table 4-6 below represents the corner frequencies and the spring constants measured from experiments 4 to 6. Comparing to Table 4-4, the magnitude is significantly larger than those of experiments 1 to 3. We suspected the reason to be as the water dried up from adding the bead solution to the brain surface, we could more clearly see where the bead was on the brain surface under the 20X objective lens. Therefore, we could more precisely align the light from the trapping fibers of the MFOTs onto the bead, increasing the probability of trapping the bead.

Table 4-6: Corner frequency and spring constant results from Type II data.

Experiment	F_c (Hz)	K (pN/micron)
4	42.0068 ± 0.75182	54266.7387 ± 971.2439
5	34.9672 ± 1.2087	45172.6158 ± 1561.4436
6	30.3599 ± 1.2825	39220.6281 ± 1656.7921

Type II data seem to be more promising than Type I, as brain stiffness is intuitively much greater than that of water. For this reason, only Type II data will be used in further analyses and comparisons. With the results of Type II experiments outlined above, a comparison between results of existing models is warranted to verify the MFOTs ability to quantify the stiffness of brain tissue.

4.4 Comparison of Elastic and Shear Moduli Results Obtained by this Work to Published Results

To verify the ability of the MFOTs in obtaining accurate brain stiffness measurements, a comparison between published results from the literature is required. Since there is so much variation in brain stiffness data (see Sections 1.1.1 and 1.1.3), we want to see where our

measurements fall, potentially bridging the gap between different brain stiffness observations. Most published works find elastic modulus or shear modulus of different matter of brain tissue instead of spring constant, therefore, in the next few sections we will use these moduli for comparisons.

4.4.1 Elastic Modulus Measurements in this Work

Restating Table 4-6, we obtained somewhat consistent spring constants with values ranging from 39 to 55 nN/micron, although the lower two stiffness seem to have some error discussed previously. For this reason, all three sets can be used as a benchmark to show the promising capability of the MFOTs in quantifying brain tissue stiffness, but we will focus on the comparison between the one good set of experimental data from experiment 4 and the data listed in the background section. Using our experimental methodology, spring constant of the brain sample is obtained, but as mentioned previously, since published data on brain stiffness is in terms of elastic modulus and shear modulus, equations 3-7 and 3-8 from Section 3.2 must be applied to provide proper comparisons. With the derivation in Section 3.2, the elastic modulus of the sample can be found with equation 3-7, restated below.

$$E_{\text{smp}} = \frac{3}{4} \frac{k}{d}. \quad 4-1$$

The variable k is the spring constant obtained from the optical trap, the variable d is the diameter of contact with the sample, and E_{smp} is the elastic modulus of the sample. Taking the good data set (from experiment 4) as an example, k was found to be 54316 N/m and as discussed in Section 3.2 the diameter d is set to 15.45 micrometers. Solving for the equation above,

$$E_{\text{smp}} = .75 * (.054267\text{N}/\text{m}) / (15.45\text{micrometers}) = 2.634\text{kPa}.$$

The same equation can be used for the unreliable experiments 5 and 6. The calculated elastic moduli for these experiments are 2.192kPa and 1.904kPa, respectively. Experiments 4-6's elastic modulus are summarized in Table 4-7 below.

Table 4-7: Elastic modulus of white matter using MFOTs method for experiments 4-6.

Experiment #	Elastic Modulus (kPa)
4 - Good	2.634
5 - Unreliable	2.192
6 - Unreliable	1.904

4.4.2 Comparison to Published Work and Discussion

To aid in clarity of the comparison between published data and our own, the white matter half of the table from Section 1.1.2.1 that outlined indentation-method-obtained brain matter elastic moduli is reproduced below.

Table 4-8: Moduli of white matter of brain tissue using the indentation method [17].

White matter moduli (kPa)			
Indent	mean	±	std
#1	1.338	±	0.036
#2	1.633	±	0.036
#3	3.025	±	0.104

#4	2.140	±	0.052
#5	2.449	±	0.050
#6	1.387	±	0.049
#7	1.050	±	0.032
#8	1.928	±	0.038
#9	2.105	±	0.107
Overall	1.895	±	0.592

Comparing the good experiment stiffness value of white matter calculated (2.634kPa) to the white matter moduli mean column in Table 4-8 above, it can be seen that our measurement is relatively close to those seen in the literature. Measurements of white matter moduli means from this table range from 1.05kPa to 3.025kPa, of which our calculated elastic modulus falls within. Even when considering unreliable experiments 5 and 6, whose only negative traits are the lack of a plateau in the lower frequency domain, their elastic moduli also fall within this range. Although the experiments themselves are classified as unreliable, this shows that the use of MFOTs to obtain elastic moduli of brain tissue is very promising. In addition, the MFOTs method yielded somewhat repeatable values, indicating that our experimental procedure and processing methods for using the MFOTs to obtain stiffness measurements are appropriate. With this in mind, more careful execution of experiments can help prove that the MFOTs is a very accurate tool for measuring brain tissue stiffness.

4.4.3 Shear Modulus Measurements in this Work

To further add to the credibility of our brain stiffness results obtained from the MFOTs method, the comparison between our calculated shear modulus of white matter will be compared to those seen in other literature. Since the elastic modulus is known and from the literature a common assumption is incompressibility (Poisson's ratio (ν) = 0.5) we can calculate shear modulus [17]. To convert Elastic Modulus (E) to Shear Modulus (G), equation 3-8 from Section 3.2 is used. The rationale as to why we use this equation is explained in Section 3.2. Calculated elastic moduli from experiments 4-6 yields the shear moduli shown in Table 4-9 below.

Table 4-9: Shear modulus of white matter using MFOTs method from experiments 4-6.

Experiment #	Shear Moduli (kPa)
4	.878
5	.731
6	.635

4.4.4 Comparison to Published Work and Discussion

To aid in clarity of the comparison between published data and our own, the table from Section 1.1.2.1 that outlined indentation-method-obtained brain matter shear moduli is reproduced below.

Table 4-10: Average shear moduli of various regions of porcine brain using indentation method [16].

Shear modulus (Pa)		
Location	White matter	Grey matter
Posterior	949 ± 311	669 ± 137
Superior	1209 ± 600	816 ± 213
Anterior	925 ± 354	738 ± 3.2
Thalamus	943 ± 109	
Midbrain	955 ± 137	

Although the data in Table 4-10 above is representative of porcine brain tissue, we are able to make general comparisons between our bovine brain tissue data. It is unknown what part of the bovine brain our sample came from, so we cannot make a direct comparison between region and moduli; instead, we will compare using only the modulus values. Published results from Table 4-10 above give an absolute range of shear modulus of between 925-1209Pa, not taking into account uncertainties. Although the shear moduli we calculated are less than the lower bound of this range, taking into account uncertainties, our data - 878Pa, 731Pa, and 635Pa - seem to be comparable. Differences in data are likely due to inaccuracies in experimentation and the use of different kinds of brain as samples. More on this will be discussed in the next chapter.

4.5 Conclusions

After proving the repeatability of the MFOTs experiments and getting comfortable with the experimental procedures by means of water-based experiments, the next step was to conduct brain experiments. Using the same experimental procedures as in the water-based experiments, spring constant data was collected from beads manipulated on brain sample surfaces. This collected spring constant was then used in calculating elastic and shear moduli of the brain matter to provide sufficient comparisons to the literature. Obtaining similar elastic moduli to those published in the literature, in addition to the similarities of shear moduli discussed in Section 4.4.1, help prove the capability of the MFOTs to obtain accurate stiffness measurements. In addition, the MFOTs method yielded somewhat repeatable values, indicating appropriate experimental procedure. Upon further optimization of the experimental procedure, the difference in data will likely decrease and show a similar level of consistency as seen in water-based trapping experiments. We will discuss drawbacks in our system and potential methodology modifications that could improve the quality of brain experimental results in the next chapter.

Chapter 5. System Limitations and Future Development

Although our comparisons between our results and those seen in the literature are comparable, the team recognizes that there is room for improvement, especially in the brain experiments, as this is the first attempt of using fiber-based optical tweezers in such biomechanical applications. Although the team obtained hundreds of data sets throughout the year, there are limited number of data sets to support the claim that the MFOTs method of obtaining brain stiffness is robust. Particularly, there are one set of power spectrum distribution data that can be fitted well by a Lorentzian and two sets of data with reasonable but questionable Lorentzian fitting, with the fitting quality determined by the criteria detailed in Chapter 3. That said, the consistency and usefulness of the system should be further confirmed by collecting more data with better fitting quality and repeatability. The following sections discuss several limitations with the experiment that the team deems as significant and can serve as a foundation for future works. By tackling these problems, the repeatability of the measurements can be expected to improve. Furthermore, measurement uncertainties are likely to be reduced, resulting in more accurate, reliable results.

5.1 Location of the Sample and its Preparation

A commonly overlooked, important piece of information about the experimental procedure is the origin of the sample - what part of the brain was the sample taken from. Different sections of the brain will provide different stiffness results. Since the sample of brain we received did not have locational labeling, the most accurate location the team can get is assumed. Figure 5-1 shows the entire brain sample as the team received it. Regardless, the team tried to avoid this problem by measuring general white matter brain stiffness, as it can be found in many locations of the brain. The same argument of locational uncertainty can still be made, but comparing white matter

stiffness to white matter stiffness is a better comparison than comparing tissue stiffness from the frontal lobe to the cerebrum. Knowing the part of the bovine brain our sample came from will allow for a better comparison between the team's results and those from the literature.



Figure 5-1: Bovine brain sample as received

Another influential factor on the quality of the experiments and the brain mechanical property results is the way that the sample was prepared. The team followed our lab's general guidelines for preparing brain samples - the sample was cut to be about one cubic centimeter in volume and was cut with a scalpel knife such that the sample was flat on its surfaces. Having a flat surface to work with during experimentation is very helpful, as it gives more working room for the MFOTs and makes trapping beads on the surface much easier. This, however, was proven difficult to accomplish without sufficient biological lab equipment, as the brain tissue is much softer and free-forming than anticipated. Figure 5-2 A) shows the brain sample after dividing it into many pieces, and Figure 5-2 B) shows one sample that roughly satisfies the requirements outlined above.

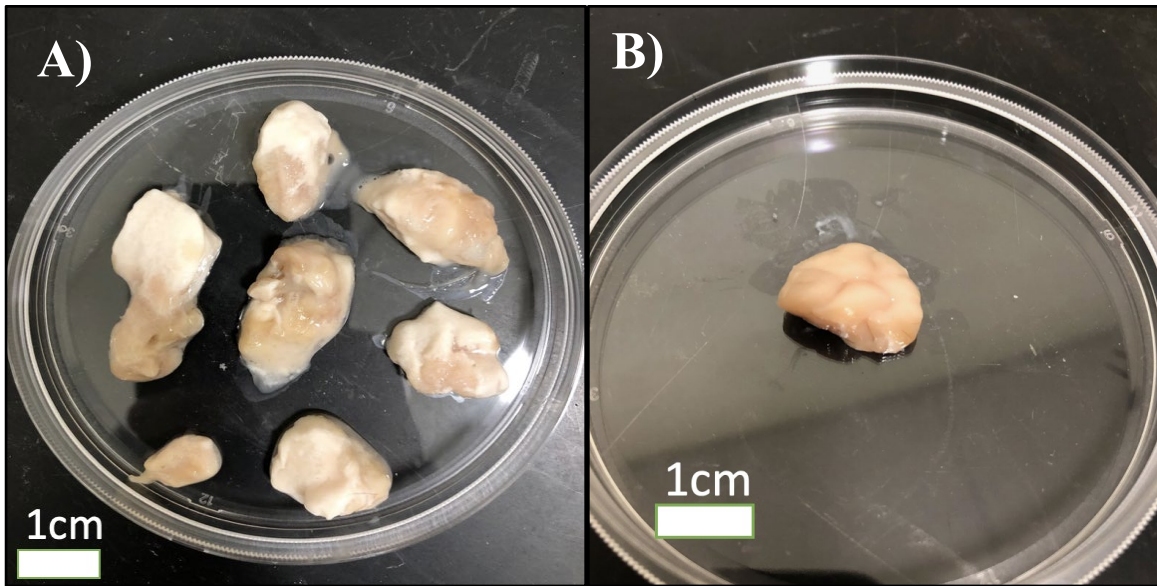


Figure 5-2: Brain samples after being cut (A); brain sample in appropriate dimension (B)

For future work on biological samples, detailed information on the sample being used should be collected before the experiment either from the department the sample is taken from or the distributor of the sample. In terms of equipment, using a lab-grade tissue slicer is recommended, as it can produce samples with a more defined shape and less standard deviation of size. Having a lab-grade slicer will also help streamline the experimental procedure and make experimentation more consistent. Better consistency means taking away modifications the team must carry out during experimentation as a result of non-uniform samples.

5.2 Impaired Vision during Experimentation

The first iterations of our brain experiments used the same methodology as in the PS beads in a deionized water medium trapping experiment. Modifications were made during experimentation, as the team was unsure how well the experimental methodology would transfer and mesh with the brain sample environment. Such modifications that were made include orienting the objective lens and MFOTs above the brain sample and how to trap beads on the brain.

The objective lens was decided to face downwards over the brain sample, as magnifying through the brain sample with our lab equipment was not feasible. This orientation gave enough working space between the objective lens and the brain sample for the MFOTs to be applied. The downside to this orientation is that the MFOTs occupy considerable space in the view field of the objective lens, thus obstructing the vision of the brain sample and blurring the image seen through the microscope camera - not ideal under any experimental circumstances.

This impaired vision makes experimentation extremely difficult, as a large part of the fine adjustments and trapping process using the MFOTs are based around images seen from the microscope camera. To temporarily solve this problem, a multi-step process was implemented. First, a bead on the surface or slightly below the surface of the brain was identified. Then, the MFOTs were moved using alignment stages until the system was above the bead in focus; the fiber tips appear blurry because of the vertical position differential between the MFOTs and the brain sample surface. Once the MFOTs and bead were aligned in the same X and Y frame, the position of the bead on the computer monitor was marked. The objective lens was then raised such that the fiber tips were in focus. After, the geometric center of the gap between the fiber tips was aligned with the marker on the computer monitor. This was followed by refocusing on the bead and turning on the laser diode. The MFOTs' were then lowered, resulting in the cross-section of the fiber light beams intersecting the bead.

In future efforts to alleviate this problem, other researchers can look into orienting either the MFOTs or the objective lens in such a way as to reduce the blocking effect. One potential orientation that one could take is to have a bi-axial setup for two objective lenses, with each observing the sample from different angles to the sample surface. This may increase the movement capabilities of the MFOTs while providing different angles to observe the experiment. A problem

with this method, however, is that using another objective is costly, and focusing on a bead on the sample surface from an angle other than perpendicular to the surface is very difficult, as the majority of the brain surface would be out of focus.

Aside from physical orientation, one can look deeper into image processing to construct three-dimensional topological maps of the brain tissue surface, which would be very helpful to users of the MFOTs system. Having a map of the brain surface, ideally a real-time-updating map, would help users track down beads near the surface of the brain, making the search portion of the experiment more time efficient. The map would also help users better align the MFOTs with the bead, taking away the need to confirm the alignment between the light spot intersection and the position of the bead beneath, as well as it would caution the users to aberrations of the brain surface like hills and valleys. Eventually, it would be optimal to automate the aforementioned alignment process using the 3D topology concept, completely eliminating manual alignment to the bead.

5.3 Limitations of the Polystyrene Beads

Polystyrene beads are common, useful objects in optical tweezers experiments. They play an integral role in stiffness calibration and are commonly used in deionized water based experiments. However, the usefulness of the PS beads decays during brain experiments, as vision of the embedded beads on the brain sample surface goes away when bead solution is added, as the bead color cannot be discerned against a background of brain tissue. This leaves the position of the beads on the brain surface unknown until the liquid part of the bead solution evaporates, making trapping beads difficult under normal experimental conditions very difficult. In addition, waiting until the solution dries up allows for heat from the microscope illumination and fiber tips to manipulate the mechanical properties of the sample, causing unwanted variation in stiffness data. Since vision of the beads on the sample surface is imperative during experimentation, other

bead options, ones that can be seen during experimentation, must be considered. Replacing regular PS beads with fluorescent beads are a potential solution. Fluorescent beads are similar to regular PS beads but illuminate under certain excitation wavelength. Bangs Laboratories, the manufacturer of the PS beads used in our experiments, sells many different fluorescent color beads that illuminate under various wavelengths of light. Using fluorescent beads with an appropriate excitation source can allow the bead's exact position on the sample to be indicated via the bead's emission despite the blurriness caused by the bead solution. This means that waiting for the liquid part of the bead solution to dry up, and giving time for the mechanical properties of the sample to change via localized heating, goes away.

The team purchased both 4-micron diameter and 15-micron diameter fluorescent polystyrene microspheres (dragon green color) from Bangs Laboratories to test our aforementioned methodology. Solutions of approximately 6000:1 water to beads were created and stored for present and future experimentation. The smaller beads, because they weigh less, are less susceptible to sinking far into the brain sample and serve as good indicators of the top surface and contour of the brain sample. The larger beads serve as the trapping beads, replacing the original PS beads from water-based experiments. This new bead solution was applied to the brain sample in the same way as the PS bead solution. Following the data sheet provided by Bangs Laboratories, the team tried exciting the fluorescent beads using different light sources, encompassing the beads' excitation wavelength of between 480-520nm. However, the team found there was no ample excitation source for the fluorescent beads available in the lab to further pursue this idea; therefore, the green fluorescent effect was not observed under the objective lens. Nevertheless, further investigation can be carried out using either different, more powerful

excitation sources or colored fluorescent microspheres as the targeted trapped bead to solve the bead vision problem.

5.4 Thermal Effects on Brain Mechanical Properties during Measurement

Heat serves as a major obstacle during experimentation, as it plays a key role in changing the shape of the brain sample and its mechanical properties. Heating of the sample occurs because of light shining on the sample from both the microscope illumination and the fiber tips. Implications of heating effects and modifications to experimental methodology to mitigate them will be discussed in this section.

5.4.1 Sample Thermo-deformation

By heating the sample, firstly, its shape becomes dynamic, introducing many logistical problems during experimentation. For example, when the sample changes shape, the microscope camera image becomes non-stationary, necessitating constant realignment between the MFOTs, the bead in the sample, and the objective lens. In addition, changing the shape of the sample can restrict the movement capabilities of the MFOTs relative to the sample. Particularly, valleys and peaks can form on the surface of the sample as moisture in the sample evaporates. Such aberrations may come into contact with the fiber tips, contaminating the MFOTs and potentially destroying their trapping ability. From a logistical stance, these problems make data collection difficult and should have been mitigated. However, given the time constraints on the MQP, this was an accepted hurdle. One potential solution could be the implementation of a moisturizing system that dispenses water on the sample to keep the sample hydrated during experimentation under the thermal loads of the light sources. The application of water droplets, however, may disturb the orientation of the beads on the brain sample. As such, this solution may be more difficult to realize.

A more likely solution is to create a mold for the sample to sit in so the sample conforms to the shape of the mold even when it dries up.

5.4.2 Sample Moisture Loss

Taking a step back, one needs to look at the sources of heat in the trapping system. Although the light from the fiber tips is relatively intense, the illumination for the confocal microscope leaves an even larger thermal footprint, as it directs focused light and heats up a larger area on the surface of the brain sample. More on the light from the fiber tips will be discussed later in this section. The microscope light source causes the moisture content of the sample to dry out very quickly - on the order of 10-15 minutes - therefore making the brain mechanical properties dynamic. Figure 5-3 below displays the localized heating of the brain sample resulting from the objective light source. As the sample dries out, the stiffness and modulus of the sample increases. Collecting data on a dry sample is not representative of the actual stiffness of a brain in a human and carries less physical significance. To help monitor the moisture content of the sample, moisture sensors could be applied during experimentation. In addition, a real-time LabVIEW program could be developed to control dispensing water droplets onto the sample, replenish for the moisture loss.

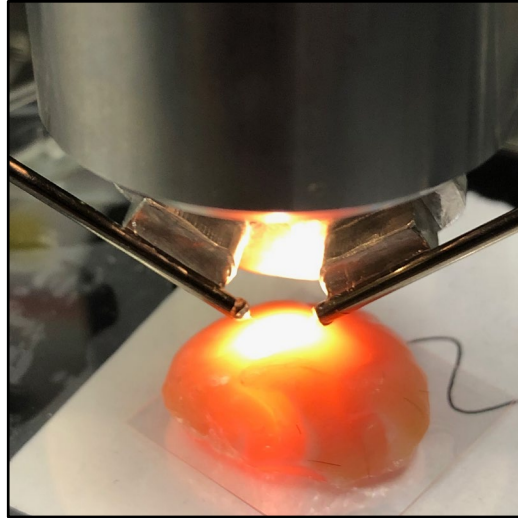


Figure 5-3: Localized heating during the experiment.

5.4.3 Evaporation of Bead Solution

In addition to the brain sample drying effects, the bead solution evaporates rather quickly, since we only apply a small volume of bead solution to the sample - around 10 microliters. Therefore, an experimental window of about 10-15 minutes by which results must be obtained is common based on our observations. As the solution dries up, trapping becomes much more rigorous as the surrounding trapping environment turns from liquid solution to solid brain matter. One way to combat this issue is to automate a bead solution dispensing system that replenishes the bead solution at a rate that the solution dries up. For the team's experiments, given time restraints, careful planning of the experiment was considered to optimize trapping of the beads under thermal effects while the solution was still present.

Due to the vision constraints discussed in Section 3.6.2, sufficient lighting must be provided to improve microscope imaging quality. For this reason, the light sources cannot be removed, although other light sources such as LEDs that emit less intense, divergent light can be

considered. Such light sources may help mitigate thermal effects on the mechanical stiffness of the brain sample and prolong the duration bead solution present on the sample.

5.4.4 Thermal Effects Summary

As mentioned earlier, another source of heating comes from the outputs of the fiber tips. Depending on the output setting of the laser that we set for our experiments, between 0.05W and 0.2W of laser power was being scattered into the brain sample from each fiber tip. The high power directed over a small surface area of about 8-10 microns can cause the bead solution to dry up faster, and in some cases inflict serious local mechanical damage to the biological sample. In addition, thermal effects seem to occur at a much faster rate when compared to the thermal effects from the microscope illumination. This means that although the sample as a whole can be in the testing environment for between 10-15 minutes, specific points on the sample can be only be interrogated for around 7-10 minutes based on our observations, further cutting down experiment time.

Figure 5-4 compares a brain sample before and after an experiment which lasted about half an hour. The dehydration effect was particularly conspicuous on the surface of the sample, as can be seen by a plastic shell-like layer formed on the surface of the brain sample. The sample displayed in Figure 5-4 shows the combined effects from those described in Sections 5.4.1 through 5.4.3, which included sample deformation and dehydration, and bead solution evaporation. Under an optimized experimental design, the brain sample would not exhibit such effects and could be tested on for a much greater amount of time. Taking into account thermal effects to form a more accurate experimental model may also be a way to incorporate such large influential factors on mechanical property measurements.

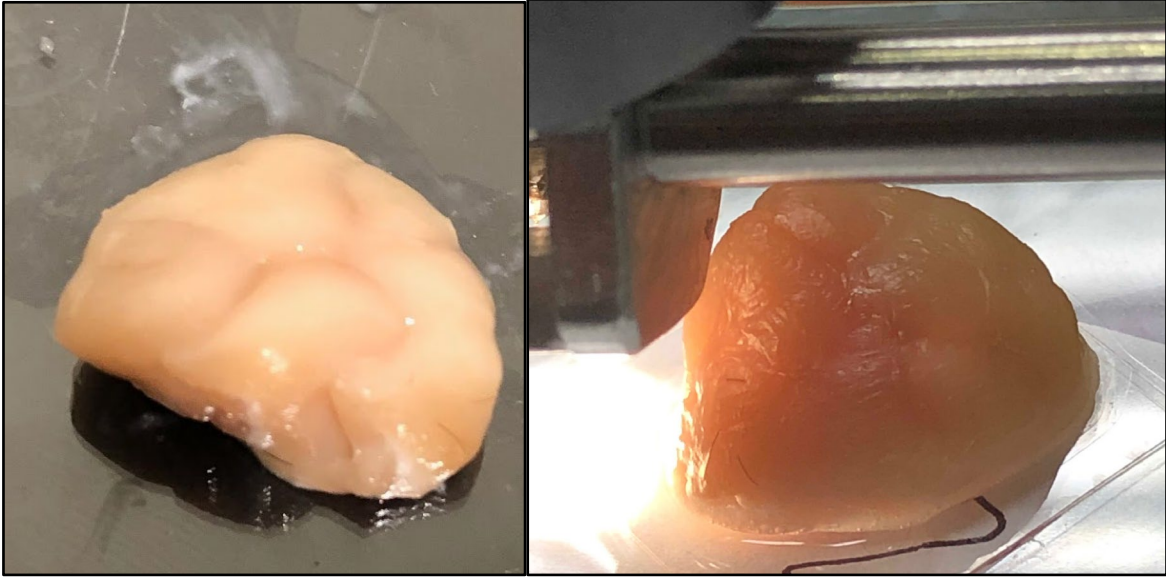


Figure 5-4: Moist brain sample before experiment (left); Surface-dehydrated brain sample after experiment (right).

Chapter 6. Conclusion

The team worked on optimizing the mechanical design of the modular fiber optical tweezers (MFOTs) to make the system more efficient and the fabrication process more reliable. To make fabrication more efficient and reliable, the team integrated new UV glue for fixing optical fibers in metal tubes and new V-groove holders for the metal tubes to assist in the fiber tip and light spot alignment process. Employing such changes, the team fabricated upwards of ten functional modules with a much greater success rate in a shorter time frame than the previous fabrication methodology. The team took this new method and authored a MFOTs fabrication guide for new Optomechanics Lab users that outlines the more reliable fabrication procedure. The optical traps created by the MFOTs the team fabricated were first calibrated in a medium of water before using them for more complex brain sample experiments. By testing the MFOTs in water first, the team gained exceptional hands-on experience and familiarity with the system that served as ample preparation for more difficult brain sample experiments. During the brain experimental process, system optimization measures were carried out to tackle various limitations, such as working distance of the objective lens, sample preparation and holding, and MFOTs orientation. As a result of integrating such changes and applying the new experimental procedure to brain samples, the team obtained three reliable data sets for white matter brain mechanical stiffness that agree with published results. To the best knowledge of the team, this project is the first to successfully use fiber optical tweezers for brain property measurements. This project enables a tool to provide a better fundamental understanding of brain mechanical properties that can be applied to traumatic brain injury diagnosis, design of better sports protective gear to prevent such brain injuries, and medicine.

It is promising to see that the MFOTs can collect stiffness measurements that are on the same magnitude as those results from many other studies. Due to the limitations in the system and lack of repeatable, reliable results collected, the project outcome does not yet provide sufficient proof that fiber optical tweezers used in this project have been calibrated to carry out the task of measuring brain stiffness. The team puts the highest value of their work on the fact that although their experimental results are not golden-standard, their results open doors for other researchers to a feasible optical tool in biomedical applications to further study and apply.

This year-long project has given an invaluable opportunity for the team of Mechanical Engineering students to work in an optical laboratory with cutting-edge optical and lab equipment. The team was able to apply their knowledge from their undergraduate coursework in solving physical hardware issues and standardizing the fabrication and calibration procedures of MFOTs to achieve the first ever white matter brain property measurements using fiber optical tweezers. This multi-disciplinary project also taught the team to work in the crossroads of Mechanical Engineering, Biomedical Engineering, Biology, and Optics. The project's educational value has gone beyond the understanding of the principles behind the laboratory experiments and has provided indispensable knowledge that the team will take into their professional careers.

Acknowledgments

We would like to extend our gratitude to Yao Shen, Yundong Ren, Mucheng Li, and Dr. Chaoyang Ti for their non-stop guidance, assistance in experiments, and insightful conversations throughout the duration of the MQP. We have learned so much from you all, and we appreciate the time we have spent with you. We wish you the best of luck in your future endeavors.

We extend our thanks to Professor Songbai Ji from the Biomedical Engineering Department at WPI. Without his willingness to provide bovine samples for our testing, this MQP would not have been able to execute experiments and achieve brain property measurements.

We would also like to express our deepest gratitude to Professor Yuxiang Liu for being a wonderful MQP advisor throughout the course of our MQP. His excitement towards our work, expertise, professional advice, research advice, and guidance were instrumental to the success of our MQP. He has been an excellent mentor that was always available to discuss our progress and to work through problem resolution with us. We appreciate all of the time we have collaborated with Professor Liu.

Finally, we would like to acknowledge our families for their constant encouragement throughout this project and our undergraduate careers. Despite being in different locations for the majority of our undergraduate careers, we always felt their support and love. Without them, we would not be where we are today and our success would not have been possible. Thank you.

References

- [1] What are the Causes of TBI? (n.d.). Retrieved October 17, 2018, from <http://www.traumaticbraininjury.com/understanding-tbi/what-are-the-causes-of-tbi/>
- [2] Clark, M., & Guskiewicz, K. (2016). Sport-Related Traumatic Brain Injury.
- [3] Duguid, J. R. (2001). *U.S. Patent No. 6,314,586*. Washington, DC: U.S. Patent and Trademark Office.
- [4] Veazie, W. (2014). *U.S. Patent No. 8,756,719*. Washington, DC: U.S. Patent and Trademark Office.
- [5] Alzheimer's Association. (n.d.). Alzheimer's Facts and Figures Report. Retrieved September 20, 2018.
- [6] BrightFocus. (2017, June 22). The Progression of Alzheimer's Disease. Retrieved September 20, 2018.
- [7] DementiaCareCentral. (2018, August 22). Alzheimer's Disease 101: How is the Disease Diagnosed and How is it Treated?
- [8] Johnson, C. L., & Telzer, E. H. (2017, September 1). Magnetic resonance elastography for examining developmental changes in the mechanical properties of the brain. Retrieved September 20, 2018.
- [9] US Centers for Disease Control and Prevention. (2017, April 27). Traumatic Brain Injury & Concussion. Retrieved from https://www.cdc.gov/traumaticbraininjury/get_the_facts.html.
- [10] Shihai Cui, Haiyan Li, Xiangnan Li, and Jesse Ruan, (2015, June 15), "Effects of the

- Variation in Brain Tissue Mechanical Properties on the Intracranial Response of a 6-Year-Old Child,” *Computational and Mathematical Methods in Medicine*, vol. 2015, Article ID 529729, 10 pages.
- [11] Finan, J. D., Sundaresh, S. N., Elkin, B. S., Mckhann, G. M., & Morrison, B. (2017). Regional mechanical properties of human brain tissue for computational models of traumatic brain injury. *Acta Biomaterialia*, 55, 333-339. doi:10.1016/j.actbio.2017.03.037.
- [12] Zhang, L., Yang, K. H., & King, A. I. (2004). A Proposed Injury Threshold for Mild Traumatic Brain Injury. *Journal of Biomechanical Engineering*, 126(2), 226-236. doi:10.1115/1.1691446.
- [13] Galford, J. E. & Mcelhaney, J. H. A viscoelastic study of scalp, brain, and dura. *J. Biomech.* 3, 211–221 (1970).
- [14] Zhang, W., Liu, L., Xiong, Y., Liu, Y., Yu, S., Wu, C., & Guo, W. (2018, January 19). Effect of in vitro storage duration on measured mechanical properties of brain tissue.
- [15] Vappou, J., Breton, E., Choquet, P., Goetz, C., Willinger, R., & Constantinesco, A. (2007). Magnetic resonance elastography compared with rotational rheometry for in vitro brain tissue viscoelasticity measurement. *Magnetic Resonance Materials in Physics, Biology and Medicine*, 20(5-6), 273-278. doi:10.1007/s10334-007-0098-7.
- [16] Van Dommelen, J. A. W., Van der Sande, T. P. J., Hrapko, M., & Peters, G. W. M. (2010). Mechanical properties of brain tissue by indentation: interregional variation. *Journal of the mechanical behavior of biomedical materials*, 3(2), 158-166.
- [17] Budday, S., Nay, R., de Rooij, R., Steinmann, P., Wyrobek, T., Ovaert, T. C., & Kuhl, E. (2015). Mechanical properties of gray and white matter brain tissue by indentation. *Journal of the mechanical behavior of biomedical materials*, 46, 318-330.

- [18] Johnson, C. L., Schwarb, H., D.J. McGarry, M., Anderson, A. T., Huesmann, G. R., Sutton, B. P., & Cohen, N. J. (2016). Viscoelasticity of subcortical gray matter structures. *Human Brain Mapping, 37*(12), 4221-4233. doi:10.1002/hbm.23314.
- [19] Amer, N. M., & Meyer, G. (1992). *U.S. Patent No. 5,144,833*. Washington, DC: U.S. Patent and Trademark Office.
- [20] Guertler, C. A., Okamoto, R. J., Schmidt, J. L., Badachhape, A. A., Johnson, C. L., & Bayly, P. V. (2018). Mechanical properties of porcine brain tissue in vivo and ex vivo estimated by MR elastography. *Journal of Biomechanics, 69*, 10-18. doi:10.1016/j.jbiomech.2018.01.016.
- [21] Chatelin, S., Constantinesco, A., & Willinger, R. (2010). Fifty years of brain tissue mechanical testing: from in vitro to in vivo investigations. *Biorheology, 47*(5-6), 255-276.
- [22] Prange, M. T., & Margulies, S. S. (2002). Regional, directional, and age-dependent properties of the brain undergoing large deformation. *Journal of biomechanical engineering, 124*(2), 244-252.
- [23] Takhounts, E. G., Crandall, J. R., & Darvish, K. (2003). *On the importance of nonlinearity of brain tissue under large deformations* (No. 2003-22-0005). SAE Technical Paper.
- [24] Nicolle, S., Lounis, M., & Willinger, R. (2004). *Shear properties of brain tissue over a frequency range relevant for automotive impact situations: new experimental results* (No. 2004-22-0011). SAE Technical Paper.
- [25] Svoboda, K., & Block, S. M. (1994). Biological applications of optical forces. *Annual review of biophysics and biomolecular structure, 23*(1), 247-285.
- [26] Ti, C., Thomas, G. M., Ren, Y., Zhang, R., Wen, Q., & Liu, Y. (2015). Fiber based optical

- tweezers for simultaneous in situ force exertion and measurements in a 3D polyacrylamide gel compartment. *Biomedical optics express*, 6(7), 2325-2336.
- [27] Liu, Y., & Yu, M. (2009). Investigation of inclined dual-fiber optical tweezers for 3D manipulation and force sensing. *Optics express*, 17(16), 13624-13638.
- [28] Neuman, K. C., & Block, S. M. (2004). Optical trapping. *Review of scientific instruments*, 75(9), 2787-2809.
- [29] Ashkin, A. (2000). History of optical trapping and manipulation of small-neutral particle, atoms, and molecules. *IEEE Journal of Selected Topics in Quantum Electronics*, 6(6), 841-856.
- [30] Kuo, S. C., & Sheetz, M. P. (1992). Optical tweezers in cell biology.
- [31] Ashkin, A. (1997). Optical trapping and manipulation of neutral particles using lasers. *Proceedings of the National Academy of Sciences*, 94(10), 4853-4860.
- [32] Wang, M. D. (1999). Manipulation of single molecules in biology. *Current opinion in biotechnology*, 10(1), 81-86.
- [33] Mehta, A. D., Finer, J. T., & Spudich, J. A. (1998). [37] Use of optical traps in single-molecule study of nonprocessive biological motors. In *Methods in enzymology* (Vol. 298, pp. 436-459). Academic Press.
- [34] Jeney, S., Florin, E. L., & Hörber, J. H. (2001). Use of Photonic Force Microscopy to study single-motor-molecule mechanics. In *Kinesin Protocols* (pp. 91-108). Humana Press.
- [35] Bustamante, C., Bryant, Z., & Smith, S. B. (2003). Ten years of tension: single-molecule DNA mechanics. *Nature*, 421(6921), 423.
- [36] Pope, L. H., Bennink, M. L., & Greve, J. (2002). Optical tweezers stretching of chromatin. *Journal of Muscle Research & Cell Motility*, 23(5-6), 397-407.

- [37] Bryant, Z., Stone, M. D., Gore, J., Smith, S. B., Cozzarelli, N. R., & Bustamante, C. (2003). Structural transitions and elasticity from torque measurements on DNA. *Nature*, 424(6946), 338.
- [38] Schirber, M. (2018, October 04). Focus: Nobel Prize-Lasers as Tools. Retrieved February 8, 2019, from <https://physics.aps.org/articles/v11/100>
- [39] Nobel Prize History. (n.d.). Retrieved from <https://www.infoplease.com/nobel-prize-history/>
- [40] “The Nobel Prize in Physics 1922”. Nobel Foundation. Retrieved 9 October 2008.
- [41] Block lab at Stanford University. (2015). Retrieved September 25, 2018, from https://blocklab.stanford.edu/optical_tweezers.html.
- [42] Charon, N. W. et al. Morphology and dynamics of protruding spirochete periplasmic flagella. *Journal of bacteriology* 174, 832-840 (1992).
- [43] Arneborg, N. et al. Interactive optical trapping shows that confinement is a determinant of growth in a mixed yeast culture. *FEMS microbiology letters* 245, 155-159 (2005).
- [44] Ignatovich, F. V. & Novotny, L. Experimental study of nanoparticle detection by optical gradient forces. *Review of scientific instruments* 74, 5231-5235 (2003).
- [45] Svoboda, K. & Block, S. M. Biological applications of optical forces. *Annual review of biophysics and biomolecular structure* 23, 247-285 (1994).
- [46] Neuman, K. C., Chadd, E. H., Liou, G. F., Bergman, K. & Block, S. M. Characterization of photodamage to *Escherichia coli* in optical traps. *Biophysical journal* 77, 2856-2863 (1999).
- [47] Liang, H. et al. Wavelength dependence of cell cloning efficiency after optical trapping. *Biophysical journal* 70, 1529-1533 (1996).
- [48] Vorobjev, I. A., Liang, H., Wright, W. H. & Berns, M. W. Optical trapping for chromosome

- manipulation: a wavelength dependence of induced chromosome bridges. *Biophysical journal* 64, 533-538 (1993).
- [49] Neuman, K. C. & Nagy, A. Single-molecule force spectroscopy: optical tweezers, magnetic tweezers and atomic force microscopy. *Nature methods* 5, 491-505 (2008).
- [50] Ashkin, A. History of optical trapping and manipulation of small-neutral particle, atoms, and molecules. *IEEE Journal of Selected Topics in Quantum Electronics* 6, 841-856 (2000).
- [51] Ti, C. (2018). Fiber optical tweezers: development, characterization, and applications (Unpublished doctoral dissertation). Worcester Polytechnic Institute, Worcester, MA.
- [52] Ignatovich, F. V. & Novotny, L. Experimental study of nanoparticle detection by optical gradient forces. *Review of scientific instruments* 74, 5231-5235 (2003).
- [53] Arneborg, N. et al. Interactive optical trapping shows that confinement is a determinant of growth in a mixed yeast culture. *FEMS microbiology letters* 245, 155-159 (2005).
- [54] Dufresne, E. R., Spalding, G. C., Dearing, M. T., Sheets, S. A. & Grier, D. G. Computer-generated holographic optical tweezer arrays. *Review of Scientific Instruments* 72, 1810-1816 (2001).
- [55] Neuman, K. C. & Nagy, A. Single-molecule force spectroscopy: optical tweezers, magnetic tweezers and atomic force microscopy. *Nature methods* 5, 491-505 (2008).
- [56] Seol, Y., Carpenter, A. E. & Perkins, T. T. Gold nanoparticles: enhanced optical trapping and sensitivity coupled with significant heating. *Optics letters* 31, 2429-2431 (2006).
- [57] Liu, Z., Guo, C., Yang, J., & Yuan, L. (2006). Tapered fiber optical tweezers for microscopic particle trapping: fabrication and application. *Optics express*, 14(25), 12510-12516.

- [58] Constable, A., Kim, J., Mervis, J., Zarinetchi, F., & Prentiss, M. (1993). Demonstration of a fiber-optical light-force trap. *Optics letters*, 18(21), 1867-1869.
- [59] “Optical Fiber”. *www.thefoa.org*. The Fiber Optic Association. Retrieved 9 October 2018.
- [60] Fiber Optic Tech. (n.d.). Retrieved September 9, 2018, from <http://teresahuang.blogas.lt/introduction-to-several-groups-of-fiber-optic-patch-cables-48.html>.
- [61] K. Lewotsky, “Fiber optics” In K. L. Lerner & B. W. Lerner (Eds.), *The Gale Encyclopedia of Science* (5th ed.). Farmington Hills, MI: Gale. (2014).
- [62] Britannica, T. E. (2018, May 17). Refractive index. Retrieved from <https://www.britannica.com/science/refractive-index>
- [63] Fiber Optics - Fiber Classifications. (n.d.). Retrieved September 9, 2018, from <http://science.jrank.org/pages/2702/Fiber-Optics-Fiber-classifications.html>
- [64] Woodward, B., & Oliviero, A. (2014). *Cabling - The Complete Guide to Copper and Fiber-Optic Networking* (5th ed.). Indianapolis, IN: Sybex.
- [65] Zhang, K. (2016, September 13). Single-mode Fiber vs. Multimode Fiber: Which to Choose? Retrieved September 9, 2018, from <http://www.fiberopticsshare.com/single-mode-fiber-vs-multimode-fiber-choose-2.html>.
- [66] Dispersion, scattering and other unfavourable physical phenomena that may take place in optical fiber. (2015, November 14). Retrieved September 9, 2018, from <http://itbundle.net/archives/210>.
- [67] Total Internal Reflection. (n.d.). Retrieved September 9, 2018, from <https://www.physicsclassroom.com/class/refrn/Lesson-3/Total-Internal-Reflection>.
- [68] Kushwaha, P. (2017, July 17). For a total internal reflection, why should light pass from a

- denser medium to a rarer medium? Retrieved September 9, 2018, from <https://www.quora.com/For-a-total-internal-reflection-why-should-light-pass-from-a-denser-medium-to-a-rarer-medium>.
- [69] Seven Advantages of Fiber Optic Cables Over Copper Cables. (2016, September 26). Retrieved September 9, 2018, from <https://blog.tripplite.com/7-advantages-of-fiber-optic-cables-over-copper-cables/>.
- [70] The Advantages and Disadvantages of Fiber Optic Transmission. (2018, August 14). Retrieved September 9, 2018, from <https://www.fs.com/the-advantages-and-disadvantages-of-fiber-optic-transmission-aid-431.html>.
- [71] Fazilleau, M. (2017, January 23). Fibre Optic PCs are Safer in High EMI Areas. Retrieved September 9, 2018, from <https://www.tinygreenpc.com/blog/optical-fibre-immune-to-electromagnetic-interference/>
- [72] Lee, B. (2003). Review of the present status of optical fiber sensors. *Optical fiber technology*, 9(2), 57-79.
- [73] Immunity to Electromagnetic Interference Archives. (2013, August 1). Retrieved September 9, 2018, from <http://www.fiber-optical-networking.com/tag/immunity-to-electromagnetic-interference>.
- [74] Harris, T. (2001, May 08). How Wiretapping Works. Retrieved October 2, 2018, from <https://people.howstuffworks.com/wiretapping.htm>.
- [75] Stewart, P. (2014, July 09). Why is Fast Ethernet connection limited to 100 meters? Retrieved September 9, 2018, from <https://learningnetwork.cisco.com/thread/38395>.
- [76] Single Mode Fiber Distance, Diameter, Speed, Bandwidth Basis. (2012, September 8).

- Retrieved September 9, 2018, from <https://community.fs.com/blog/single-mode-fiber-how-much-do-you-know.html>.
- [77] Copper vs. Fiber - Which to Choose? (n.d.). Retrieved September 9, 2018, from <https://www.multicominc.com/training/technical-resources/copper-vs-fiber-which-to-choose/>.
- [78] Bowyer, C. (2016, October 12). Copper VS. Fibre: Battle of the Bandwidth. Retrieved September 9, 2018, from <http://pacificdatacom.com.au/copper-vs-fibre-battle-of-the-bandwidth/>.
- [79] Giallorenzi, T. G., Bucaro, J. A., Dandridge, A., Sigel, G. H., Cole, J. H., Rashleigh, S. C., & Priest, R. G. (1982). Optical fiber sensor technology. *IEEE transactions on microwave theory and techniques*, 30(4), 472-511.
- [80] Culshaw, B., Stewart, G., Dong, F., Tandy, C., & Moodie, D. (1998). Fibre optic techniques for remote spectroscopic methane detection—from concept to system realisation. *Sensors and Actuators B: Chemical*, 51(1-3), 25-37. doi:10.1016/s0925-4005(98)00184-1.
- [81] Liu, T., Wei, Y., Song, G., Hu, B., Li, L., Jin, G., . . . Wang, J. (2018). Fibre Optic Sensors for Coal Mine Hazard Detection. *Measurement*, 124, 211-223. doi:10.1016/j.measurement.2018.03.046.
- [82] Dakin, J. P. (2002). Evolution of highly-selective gas sensing methods using correlation spectroscopy.
- [83] Choi, Y., Abbas, S. H., & Lee, J. (2018). Aircraft integrated structural health monitoring using lasers, piezoelectricity, and fiber optics. *Measurement*, 125, 294-302. doi:10.1016/j.measurement.2018.04.067.
- [84] Poeggel, S., Tosi, D., Duraibabu, D., Leen, G., McGrath, D., & Lewis, E. (2015). Optical

- fibres pressure sensors in medical applications. *Sensors*, 15(7), 17115-17148.
- [85] Abiomed.com. (n.d.). Retrieved October 2, 2018, from <http://www.abiomed.com/>.
- [86] Pinet, É. (2011, May). Pressure measurement with fiber-optic sensors: commercial technologies and applications. In *21st International Conference on Optical Fiber Sensors* (Vol. 7753, p. 775304). International Society for Optics and Photonics.
- [87] Hashemian, H. M., Black, C. L., & Farmer, J. P. (1995). *Assessment of fiber optic pressure sensors* (No. NUREG/CR--6312). Nuclear Regulatory Commission, Washington, DC (United States). Div. of Systems Technology; Analysis and Measurement Services Corp., Knoxville, TN (United States).
- [88] Shepard, R.L., and Thacker, L.H., "Evaluation of Pressure Sensing Concepts: A Technology Assessment," ORNLEM-12296, Oak Ridge National Laboratory, September 1993.
- [89] Ghoname, S. (2013, December 17). Biomedical Optical Sensor. Retrieved October 2, 2018, from <https://www.slideshare.net/sherifghoname/biomedical-optical-sensor>.
- [90] Kim, Y., & Neikirk, D. (n.d.). Fabry-Perot Based Pressure Transducers. Retrieved October 2, 2018, from http://weewave.mer.utexas.edu/MED_files/MED_research/F_P_sensor_folder/FP_pressure_sensor.html.
- [91] Zeiss, C. (n.d.). Coherence of Light. Retrieved October 3, 2018, from <https://www.zeiss.com/microscopy/us/solutions/reference/all-tutorials/light-sources/coherence-of-light.html>.
- [92] Fabry-Perot Cavity. (n.d.). Retrieved October 2, 2018, from <http://fiso.com/section.php?p=94&>.
- [93] Wei, M. T., Yang, K. T., Karmenyan, A., & Chiou, A. (2006). Three-dimensional optical

- force field on a Chinese hamster ovary cell in a fiber-optical dual-beam trap. *Optics Express*, 14(7), 3056-3064.
- [94] Liu, Y., & Yu, M. (2009). Multiple traps created with an inclined dual-fiber system. *Optics express*, 17(24), 21680-21690.
- [95] Taguchi, K., Ueno, H., Hiramatsu, T. & Ikeda, M. Optical trapping of dielectric particle and biological cell using optical fibre. *Electronics Letters* 33, 413-414 (1997).
- [96] Tam, J. M., Biran, I. & Walt, D. R. An imaging fiber-based optical tweezer array for microparticle array assembly. *Applied Physics Letters* 84, 4289-4291 (2004).
- [97] Collins, S. D., Baskin, R. J. & Howitt, D. G. Microinstrument gradient-force optical trap. *Applied optics* 38, 6068-6074 (1999).
- [98] Smith, S. P., Bhalotra, S. R., Brody, A. L., Brown, B. L., Boyda, E. K., & Prentiss, M. (1999). Inexpensive optical tweezers for undergraduate laboratories. *American Journal of Physics*, 67(1), 26-35.
- [99] Guck, J. et al. The optical stretcher: a novel laser tool to micromanipulate cells. *Biophysical journal* 81, 767-784 (2001).
- [100] Xin, H., Liu, Q., & Li, B. (2014). Non-contact fiber-optical trapping of motile bacteria: dynamics observation and energy estimation. *Scientific reports*, 4, 6576.
- [101] Tam, J. M., Biran, I., & Walt, D. R. (2004). An imaging fiber-based optical tweezer array for microparticle array assembly. *Applied Physics Letters*, 84(21), 4289-4291.
- [102] Constable, A., Kim, J., Mervis, J., Zarinetchi, F. & Prentiss, M. Demonstration of a fiber-optical light-force trap. *Optics letters* 18, 1867-1869 (1993).
- [103] Guck, J., Ananthakrishnan, R., Mahmood, H., Moon, T. J., Cunningham, C. C., & Käs, J.

- (2001). The optical stretcher: a novel laser tool to micromanipulate cells. *Biophysical journal*, 81(2), 767-784.
- [104] Guck, J. et al. Optical deformability as an inherent cell marker for testing malignant transformation and metastatic competence. *Biophysical journal* 88, 3689-3698 (2005).
- [105] Berthelot, J. et al. Three-dimensional manipulation with scanning near-field optical nanotweezers. *Nature nanotechnology* 9, 295–299 (2014).
- [106] Ti, C., Ho-Thanh, M. T., Wen, Q., & Liu, Y. (2017). Objective-lens-free Fiber-based Position Detection with Nanometer Resolution in a Fiber Optical Trapping System. *Scientific reports*, 7(1), 13168.
- [107] Oliver, W. C., & Pharr, G. M. (2004). Measurement of hardness and elastic modulus by instrumented indentation: Advances in understanding and refinements to methodology. *Journal of materials research*, 19(1), 3-20.
- [108] Berg-Sørensen, K., & Flyvbjerg, H. (2004). Power spectrum analysis for optical tweezers. *Review of Scientific Instruments*, 75(3), 594-612.

Appendix A: Protocol for MFOTs Fabrication

This appendix intends to serve as a step-by-step guideline for Optomechanics Lab users to fabricate a modular fiber optical tweezers (MFOTs) system.

I. Fiber end face processing

The objective of step I is to prepare two good fiber tweezer tips to be used for trapping.

1. Fiber Cleaving

- a) Start from a SMF-28 fiber with a length of approximately 1 meter.
- b) Strip the fiber tip from one end by about 2cm and clean it gently with Kimwipe soaked by isopropanol.
- c) Use the golden fiber holder from the splicer (see Figure A-1) and associated mechanical cleaver to cleave the fiber, creating a perfectly flat fiber end. The specific fiber holder and cleaver combination will ensure appropriate extrusion length for step I-2 and I-3, if it is desired to execute these steps.

2. Check fiber cross section (Optional)

- a) Carefully transfer the fiber holder on to the angular localizer (AL). AL's sliding block has magnets to fix the fiber holder in place.
- b) Use the micrometer knob to move the block away from the camera first. Then slowly slide the block towards the camera. Make sure the fiber enters the ferrule without excessive bending (shown in Figure A-1)

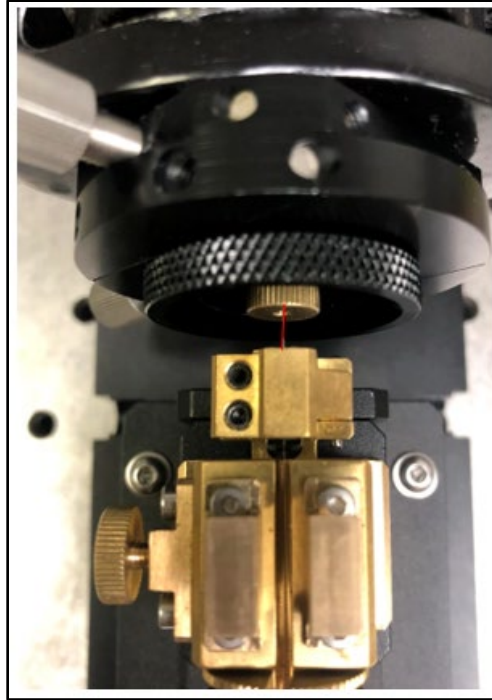
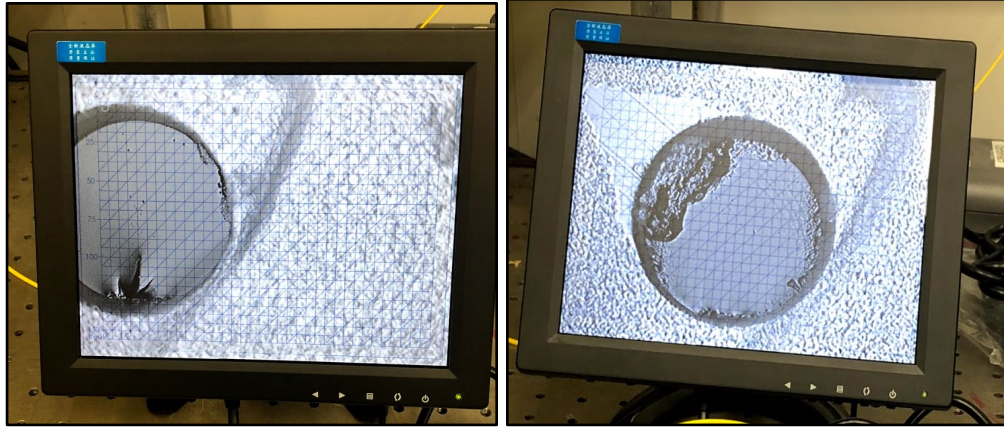


Figure A-1: Minimal bending when inserting the fiber into the ferrule.

- c) Slowly push the fiber holder inwards towards the camera using the micrometer knob until a clear, in-focus image of the fiber cross section is seen (shown in Figure A-4).
- d) Check for cracks, chipping, or digging on the cross section. The standard is that there should be no defect on the surface except for defects that are less than one monitor grid resolution away from the perimeter of the fiber end face. See Figures A-2 & A-3 for unacceptable fiber end faces and Figure A-4 for a good end face.



Figures A-2 & A-3: Typical bad end faces of fibers on the AL monitor.

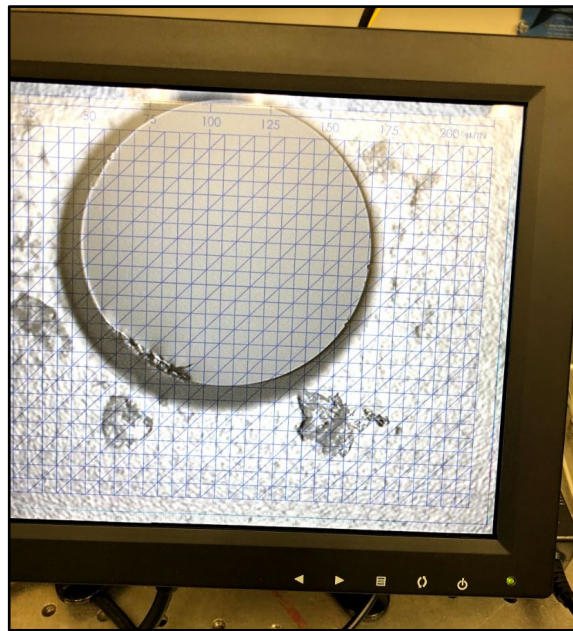


Figure A-4: Good end face of a fiber.

- e) Optional step: If any debris is observed in the image, gently remove the ceramic ferrule inside the golden knob and rinse it with isopropanol. Repeat steps I-2-a-I-2-d.

3. Check fiber cut quality by sidewall images on the splicer

- a) After obtaining a cleaved fiber, with or without use of the angular localizer, carefully place the fiber holder onto the magnets in the automatic fusion splicer, then close its lid.
- b) The screen will show the cut quality. If no warning is generated and the fiber seems to have no aberrations, then this fiber end face is suitable for use as a fiber tweezer tip. Two fibers with such tips are needed in later steps. If the end section was not good, re-cleaving the fiber and repeat steps I-1-a to I-1-c, at minimum, is needed.
- c) If two fibers are placed in the splicer at the same time, DO NOT press the splicer button! This will fuse two good end faces together, which is not the goal of this phase. In this phase, good fiber tips for the fiber tweezers are desired.

Section note: this step will take rather long to finish if the angular localizer is used, so if it is desired to use this tool, have two team members do Section I procedures independently at the same time (two golden fiber holders are available for use). It is also acceptable to skip the angular localizer steps altogether and just use the fusion splicer image to verify good fiber tips.

II. Installation of prepared fibers onto the alignment system

The objective of step II is to set up the trapping system. This step has three phases:

- 1) Installing the fiber into the iron tubes to alleviate any micro vibrations the fiber may experience during use.
- 2) Fixing the tubes to the alignment module to aid in aligning the light spots from the fibers.
- 3) Splicing the fiber ends to the coupler system to provide power.

1. Insert fiber into steel tube

- a) First, cut the steel tube into 25mm long sections using a Dremel 4000 drill. It is helpful to clamp the tube down before cutting to make a cleaner cut. Optional: insert a fiber into the tube before cutting it to help prevent the steel from melting and closing its hole.
- b) Carefully insert the fiber into a steel tube (1/16 x 0.025 wall, 304 steel - Part number 51755K19 from McMaster-Carr) from the un-cleaved fiber end. DO NOT insert from the good surface, this will ruin all progress from Section I, as scratches and other aberrations will be introduced to the cleaved fiber end face.
- c) Pull the steel tube up the fiber so that approximately 4mm of the fiber (the end with a good surface) is outside the iron tube (see Figure A-5).



Figure A-5: 4 mm of fiber extrusion from the tube.

2. UV glue on both ends of steel tube

- a) Check the 4mm extrusion using a caliper and then apply enough UV glue from the syringe on the end of the steel tube facing the good fiber end face so the end face of the tube is covered with the glue.

- b) Use the UV light source to cure the bead of glue for about 10 seconds, rotate the tube to ensure even and solid curing.

WARNING: UV EYE PROTECTION/GLOVES REQUIRED

- c) Apply UV glue on the other end of the steel tube and repeat b).

3. Fix tubes onto alignment module.

- a) Use a 2mm hex-head socket screwdriver to loosen the tube holder on the alignment system. Rotate the height adjust knob to the top position to avoid collision between the tip and microscope platform.

- b) Place a steel tube with finished fiber on the black clamp seen in Figure A-6, make sure the top end of the tube sits flush with the holder piece and the tube lay flush in the clamp's V-groove. This step can be made smoother if two members on the team can work together; one screwing in the clamp screws and the other installing the tubes.

Note: The aluminum holders on the alignment module are fixed at 55 degrees below the x-axis.

- c) Repeat b) for the other steel tube.
- d) Fix the alignment module on the lab platform. The screwdriver used here is a ¼-inch hex-head socket screwdriver. The end set up should look like that shown in Figure A-6.

4. Splicing the fiber ends to the coupler outputs

- a) Cleave the free end of the fibers in the clamps as well as the coupler outputs using the fiber holder, as described in I-1.

- b) Place both fiber holders in the splicer, checking the cut quality. If there are no defects with either fiber tip, proceed with splicing by simply pressing the splice button (looks like a “play” button on the fusion splicer).
- c) Carefully tape down the spliced portion onto a piece of cardboard, fully covering the stripped part of the fiber with tape. A better option for this step is to use the fiber-recoater to re-apply buffer to the fiber.
- d) Optional: if the fiber-recoater is desired to be used, place the newly spliced fibers onto the recoater, with the splicing interface in the middle of the recoater, and set the length of material and cure time desired to 40mm and 20 seconds respectively. Follow the instructions displayed by the recoater to recoat the fiber.

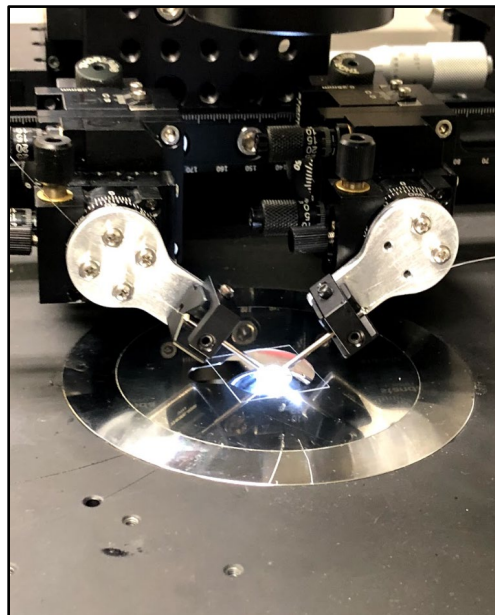


Figure A-6: Final setup for bead-trapping.

III. Fiber and light spot alignment to enable the optical trap

The objective of step III is to align the two fiber’s light spots and generate an optical trap.

1. Preparing the microscope and bead solution

- a) Fill around half of a 25mL beaker with DI water, adding 0.02mL of 15-micron diameter polystyrene beads (Bangs Laboratories, Inc.) to the DI water using a micro-pipette. The beads should have a density of 2.0g/cm^3 . These beads uniform in geometry and density, serving as appropriate samples to use in optical trapping experiments.
- b) Homogenize the solution using the ultrasonic shaker for a duration of 10 minutes. This reverses bead aggregation.
- c) While the bead solution is shaking, put a drop of Nikon Type A immersion oil on the 100x objective lens of the Nikon microscope.
- d) Put a clean cover glass on the microscope stage and add about 3 drops of DI water on top of it using a standard pipette; then add a few drops (between .05 and .15mL) of the shaken bead solution to the droplet.
- e) Rotate the lens focus knob to the bottom safe position (see Figure A-7).

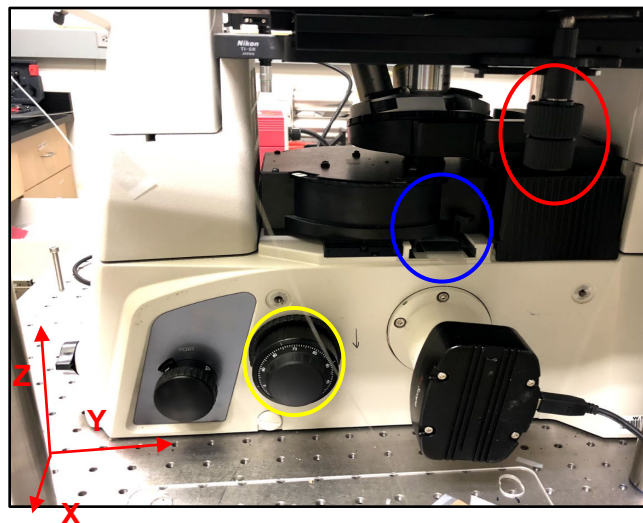


Figure A-7: Side view of the microscope (yellow circle: lens focus knob; blue circle: filter; red circle: stage planar motion knob).

2. Alignment under 10x objective lens

- a) Note the axes orientations in Figure A-7 above.
- b) Find the edge of water and focus on it by moving the microscope stage using the stage planar motion knobs (see Figure A-7's red circle). Once the water edge is in focus, move the stage such that the objective now looks into the water droplet. Verify that the droplet contains beads.
- c) Move the whole alignment module towards the focus of the objective lens to find the fiber tips. Try to hover the tips over the water and observe a shadow on the monitor, which signifies the tip is on top of the lens. When the fiber shadow is found, rotate the lens focus knob upwards and move the alignment module downwards until the fiber tips are in focus. Adjusting both the lens focus knob and alignment module takes practice. **Be careful not to hit the stage with the objective lens.**
- d) Check the quality of the tips. If either fiber tip shows a significant defect that means it was damaged during the transfer process. Re-doing section I for the defect fiber is not required at this step, as re-doing section I need only be carried out if the light spots are not good (this will be addressed in step III-4).
- e) Fiber alignment module enables us to adjust the location in all three axes. It also features fine-tuner for rotational movement for the fiber in yz-plane, which are preset to certain values, they will NOT be used in alignment process. Figure A-8 shows all the knobs for individual fiber adjustment.

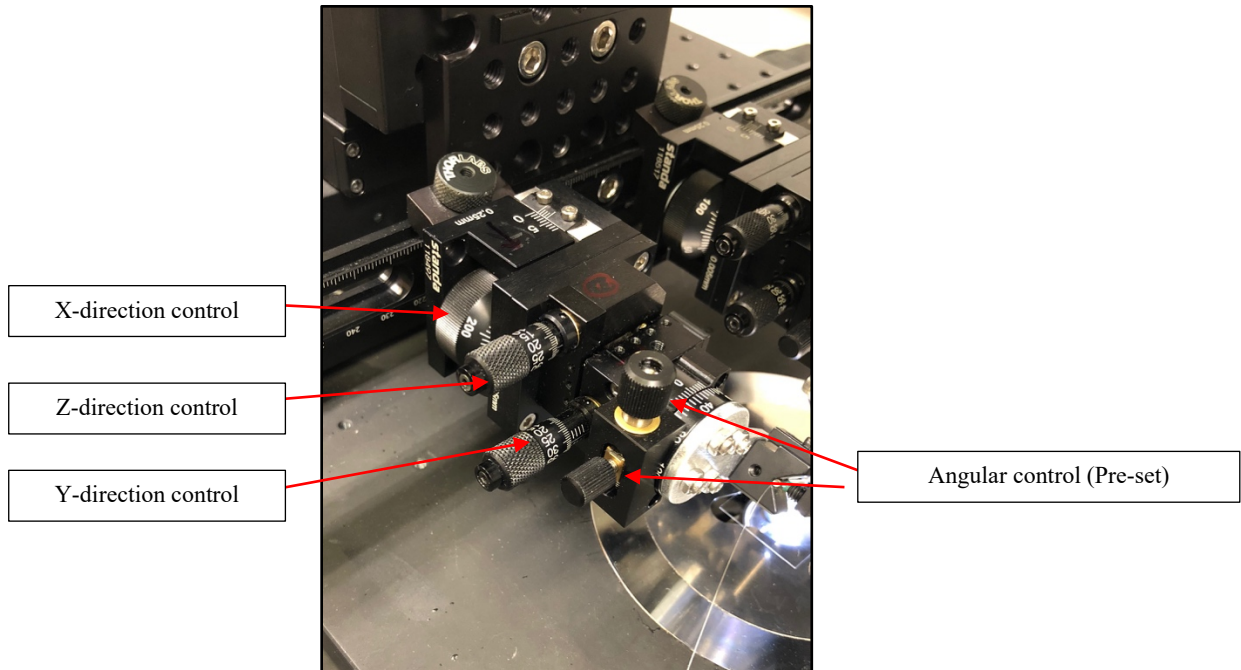


Figure A-8: Individual fiber alignment setup.

- f) Align the fiber properly under 10x magnification so the fibers are roughly in colinear. Ensure the fibers sit at around the same height (both top edges are in focus at the same time, for instance). Also, about half of the end face diameter should be the separation distance between the two fibers. Fine adjustment on each fiber can be carried out by altering the individual 3D adjustment knobs on the alignment module stage platforms (see Figure A-8 above). A proper alignment procedure is demonstrated in Figure A-9.

Start from a left picture where the fibers are misaligned. Move the two fibers closer towards each other in y-direction as black arrows show. Then move the two fiber in x-direction so they line up, as shown by the red arrows. It is crucial to align the

fiber tips as well as possible under 10x magnification and get them roughly on the same height level using the z-direction control knob.

- g) After aligning, return the object lens to its safe position; rotate completely downwards.

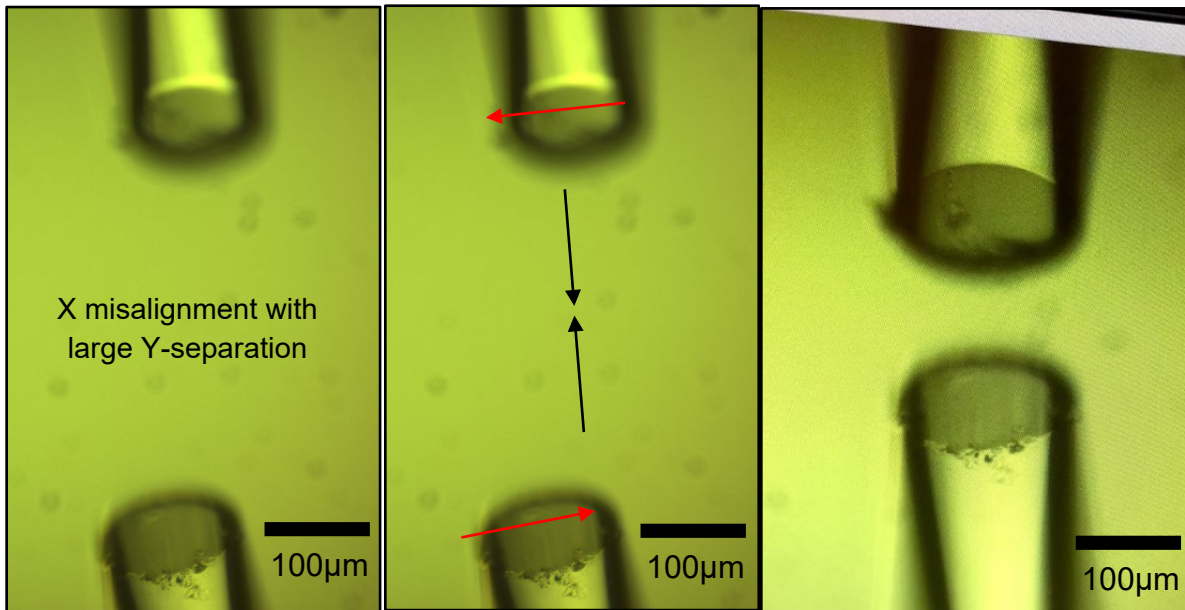


Figure A-9: Proper fiber alignment process under 10x.

3. Alignment under 40x objective lens

- a) Change to the 40x objective lens and repeat steps III-2-a) to d). The working distance of the 40x objective lens is shorter than the 10x working distance, so be very careful when focusing on the fiber tips. A proper alignment example is shown below in Figure A-10.

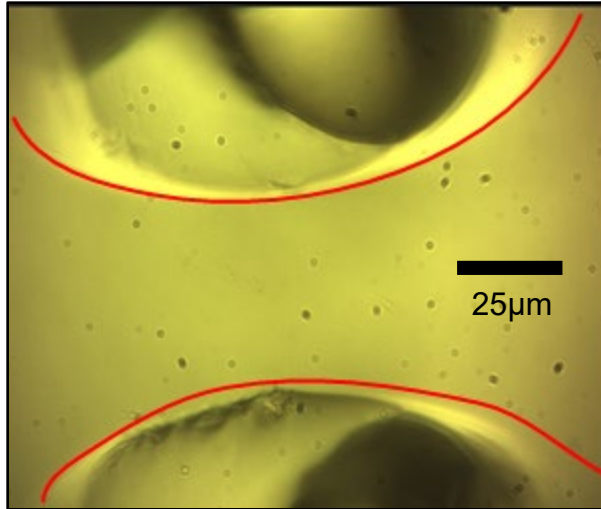


Figure A-10: Fiber alignment under 40x.

- b) After aligning, return the object lens to its safe position; rotate downwards completely.
4. Alignment under 100x objective lens
 - a) The working distance of 100x objective lens is very small, use the fine adjust knob ONLY.
 - b) Locate the fiber tips under 100x magnification by following steps III-2-a) to d).
 - c) After the tips are aligned, turn on the laser diode. EYE PROTECTION REQUIRED.
 - d) Move the whole alignment module upwards so that the light spot comes into focus (see Figure A-11).

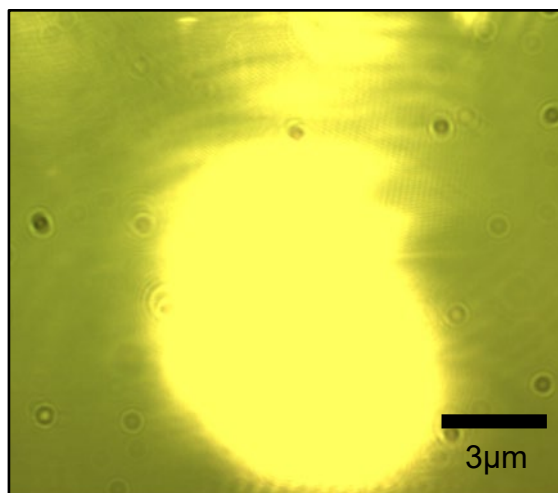


Figure A-11: Typical good light spot (coming from one fiber only).

- e) Check the quality of the light spots (Figure A-11). Ideally, they would be oval-shaped spots with similar size. Check intersection of two light beams, as well as before and after the intersection (Figure A-12).

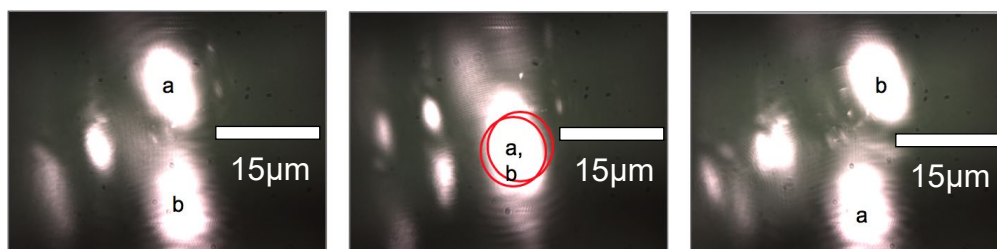


Figure A-12: Microscope images at different objective lens heights. Light spots above light intersection (left); at intersection (middle); below light intersection (right). The two spots move along the same straight line when moving the objective lens, indicating a good alignment.

5. Trapping of the bead

- a) Move the superposed light spot to the same height level as a bead, then shine the light on the bead. Insert the dichroic mirror filter to get rid of the light spot to see

only the beads. Horizontal trapping is achieved when x- and y-movement of the alignment module is followed by planar displacement of the bead. In a good trap, the bead movement will be sensitive to the movement of the alignment module with little lag.

- b) Slowly rotate the height adjustment for the whole alignment module. When z-movement of the whole alignment module is followed by the spherical bead moving out of focus successful three-dimensional trapping has been realized. In other words, the bead is successfully trapped in the z-direction when the bead on the screen gets blurry while moving the alignment module upwards or downwards (upward movement is recommended).

Note: For this step, it is helpful to have another bead in focus; the bead being lifted will become blurry while the other bead will remain focused - verifying the realization of the trap.

- c) Turn off the laser diode.

IV. Modular system assembly - transition and fixation of the aligned fibers onto a common board

The goal of this step is to transfer the aligned fibers to the common board, completing the fabrication of a modular system.

1. Aligning the common board module

- a. Attach a common board to the set of optical posts extending from the second set of 3D stages (see Figure A-13 a and b).

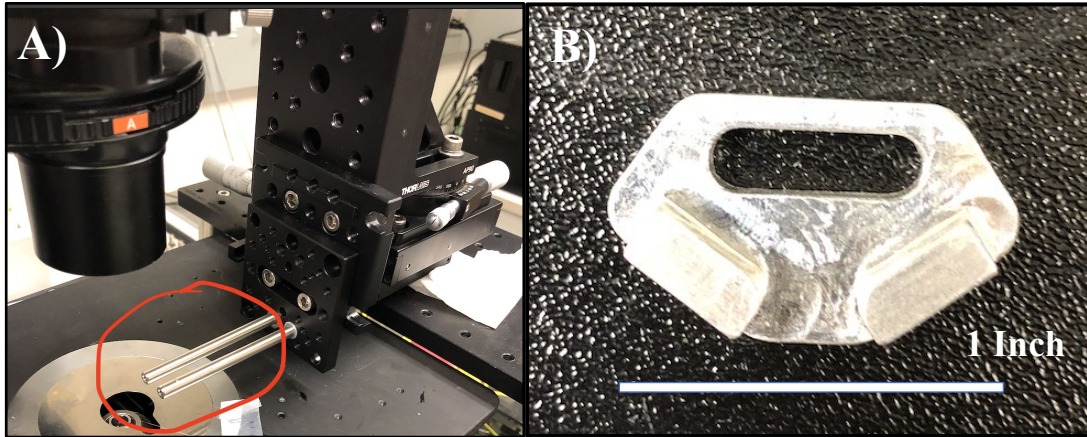


Figure A-13: A) optical posts where common board attaches to 3D stages; B) the common board.

- b. Slowly move the common board in towards the two aligned fibers while looking at the computer image under the microscope. Stop moving the common board in towards the fibers once contact is made with the fibers – there is movement of one of the fibers on the screen. This shows that there is a misalignment of the common board with the fiber tubes.
- c. Retract the common board from the fibers and adjust the angle the common board makes with the fiber tubes using its rotational stage (see Figure A-14).

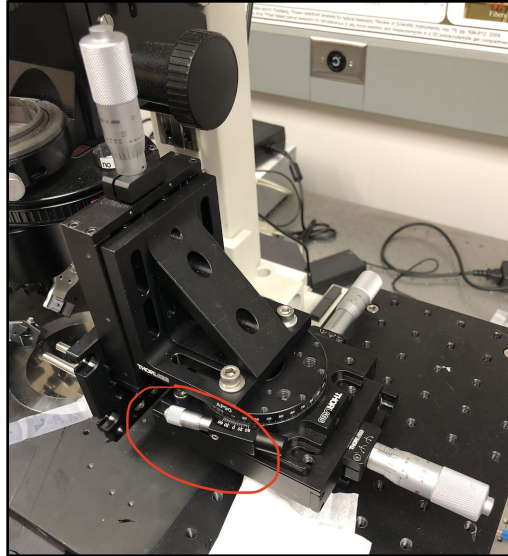


Figure A-14: Angular adjustment knob on the stage.

- d. Repeat steps b)-c) until both fibers move at the same time as a result of the common board coming into contact with them. This means the common board is aligned with the fiber tubes and the fiber tubes are ready to be transferred (see Figure A-15).



Figure A-15: Ideal trap should be preserved during the transfer process. The bead is 15.45 micrometers in diameter.

- e. Retract the common board from the fibers about 1-2cm and apply a layer (enough to fix the tubes onto the common board) of UV glue to the extrusions on the common board. It is helpful to use curved tweezers as applicators of the UV glue.
- f. Move the common board, slowly, into the fibers until the fibers touch the UV glue. To cure the glue, apply UV light for at least 5 minutes. **WARNING: UV EYE PROTECTION/GLOVES REQUIRED**
- g. Add more viscous UV glue to the top of the tubes to better fit the tubes to the common board, then cure the glue for a minimum of 3 minutes per fiber tube. A more viscous UV glue is required because it sticks well to both the aluminum common board and the UV glue from the syringe, creating a tighter bond between the two. It is recommended to use a toothpick to help spread the glue. A kimwipe to clean up excess glue is recommended. Note: do not let the UV glue fall into the bead solution below or let the glue get on the fiber tips. If the glue gets on the fiber tip, the whole procedure must be carried out again.
- h. Loosen the contact screw on the black clamp. Once the contact screw is no longer pushing the fiber tube into the V-groove of the black clamp, remove the tube holding clamps using the appropriate screwdriver to free the fibers from the tubes. Gently retract the common board, now with attached fibers, from the system.
- i. Test the system to see if it can perform 3D trapping. If it does not, then the experiment is deemed a failure and must be re-done.
- j. Unscrew the common board from the optical posts while holding down the common board (to avoid dropping it) and place in a safe, clean location until further use. BE

VERY CAREFUL NOT TO TOUCH THE TUBES OR FIBERS DURING THIS
STEP.

- k. The MFOTs have been successfully created.

Appendix B: Brain Experimental Procedure

This appendix intends to serve as a step-by-step guideline for executing brain experiments using the MQP team's fabricated modular fiber optical tweezers MFOTs. These steps are not concrete and can be modified as needed during experimentation, as experiments will likely differ. The fundamentals of this experimental procedure can be achieved by following the fabrication protocol in Appendix A.

I. Setting up the System

The objective of step I is to set up the MFOTs experimental system, enabling the trapping of beads on the brain surface. The system setup seen in Figure 2-8 and Figure B-1 should be emulated prior to running experiments, unlocking the trapping and data collection capability of the MFOTs. When all components are setup properly, and all optical components (laser diode, fiber couplers, MFOTs trapping fibers) are connected, the system is ready to be used. For these brain experiments, the brain sample should be shaped as best as possible like a 1 cm³ cube and placed in a petri dish. The petri dish should then be placed under the 20X long working distance objective lens. For mounting the MFOTs on the 3D stages, follow the visual seen in Figure 2-9B and below in Figure B-1.

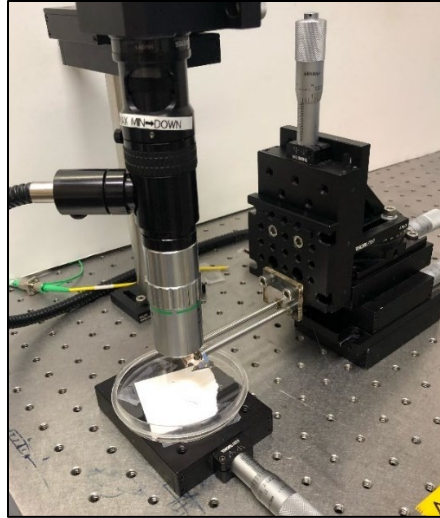


Figure B-1: Brain Experiment Experimental Setup.

II. Applying the Bead Solution

The purpose of this step is to outline the preparation of the bead solution and describe its application onto the brain sample. Comments of induced heating will also be discussed.

- A) Prepare the bead solution in the same way as discussed in Appendix A III.
- B) Using a microliter resolution pipette, collect approximately 5-10 microliters of beads solution and displace it on the top of the brain surface, ideally on a flat portion of the brain sample.
- C) Note: Throughout experimentation, the solution will dry up due to the induced heating from the microscope illumination and the laser outputs from the fiber tips of the MFOTs (more on this is discussed in Section 5.4.4). Because of this heating effect, bead solution may need to be reapplied periodically. This re-application will also help maintain the moisture of the brain sample, stabilizing its mechanical properties.

III. Alignment of the Bead on the Brain Surface, the MFOTs, and the Objective Lens

The goal of this step is to properly align all components of the system so trapping of the beads on the brain surface can be carried out. Aligning all components simplifies the trapping procedure greatly, and serves the same purpose as the alignment procedure outlined in Appendix A section III.

- A) Alignment of the optical fiber tips need not be carried out, as this has already been carried out in the fabrication of the MFOTs. First, identify a bead near the surface of the brain that will be trapped using the objective lens (see Figure B-2). To move the objective lens around, use the micron resolution 3D stages. Chosen beads for trapping should be slightly submerged into the brain surface to allow for ample light application onto the bead via the fiber tips of the MFOTs. With the bead identified, the objective lens and the bead have been aligned.

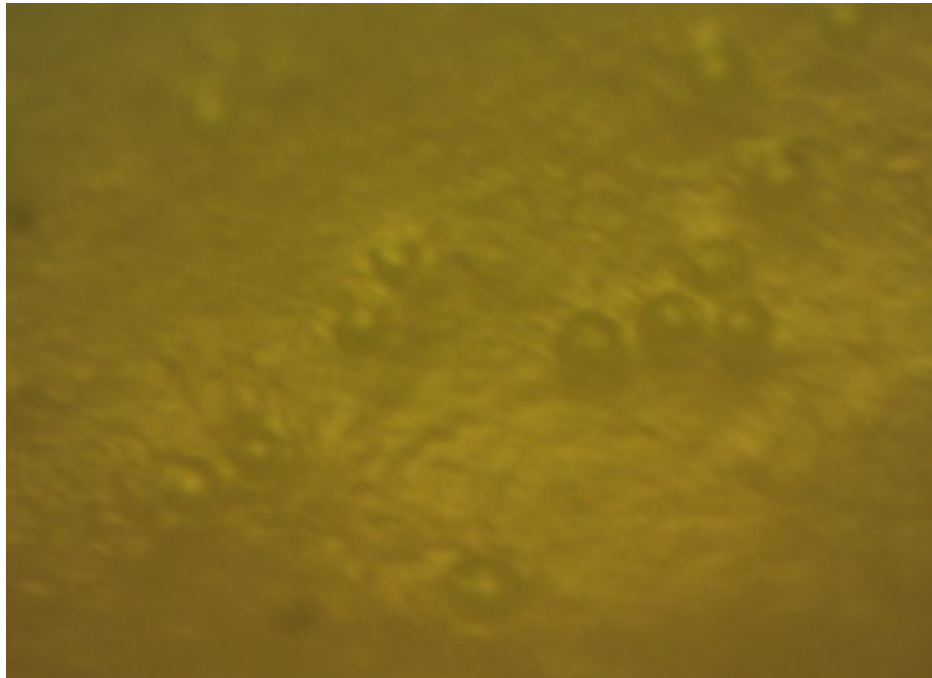


Figure B-2: Beads in the Brain Surface.

- B) This next step involves aligning the MFOTs with the objective lens and the bead on the brain surface.
- a. First, raise the objective lens about 50 microns upwards so that the focal plane potentially is in the movement path of the MFOTs' fiber tips.
 - b. Next, move the MFOTs until the MFOTs is under the objective lens. While moving the MFOTs, note if a shadow appears on the computer monitor that the microscope camera is attached to. This shadow results from the fiber tips blocking the microscope illumination and denotes that the fibers are out of focus with the objective lens. When the shadows are found, move the objective lens upwards and downwards until the fiber tips are focused on. Note: do not move the objective lens in the X and Y directions, as this will misalign the objective lens with the bead on the brain surface.
 - c. Once the MFOTs are in focus with the objective lens, the system is only misaligned in the Z-direction. To align in the Z-direction, move the objective lens downwards by about 5 microns (half a turn on the Thorlabs 1 dimensional translational stage). Follow this movement with a 5 micron downwards movement of the MFOTs, or until the MFOTs are back in focus with the objective lens. Repeat this same procedure until the bead on the brain is focused on by the objective lens.
 - d. When the bead is focused on by the objective lens, the MFOTs are very close to the surface of the brain. DO NOT move the MFOTs into focus of the objective lens when the objective lens is focused on the bead. Doing this may cause the fiber tips to come into contact with the brain sample, thus

contaminating them and risking the destruction of the MFOTs module. Therefore, once the bead is focused on with the objective lens, raise the objective lens back up until the fiber tips are focused on.

- e. With the fiber tips in focus, mark the geometric center of the gap between the two trapping fibers on the computer monitor with a piece of tape or a sticky note. This marker predicts the location of the intersection of the optical fiber tips' light beam outputs, and thus the approximate location of the optical trap.
 - f. Refocus on the bead in the brain sample surface with the objective lens. If the marker on the computer monitor falls over the bead in the brain sample, all components are aligned in the X and Y directions. After seeing the components are aligned, turn on the laser diode and set a power of between 300mA to 1200mA (lower power means less localized heating of the sample). Also initiate the LabVIEW data collection program described in Section 3.3.
- C) Move the MFOTs downwards until the light spots are seen shining on the bead surface as seen in Figure B-3 below.



Figure B-3: Light Shining on the Bead that is in the Brain Surface.

- a. With the light spots, and thus optical trap, engaged on the bead, turn on the LabVIEW program to record the backscattered light collected via the optical fibers. Record the data using the “record data” button on the front panel of the LabVIEW program. This program is described more in depth in Section 3.3.
- b. Note: Trapping of the bead is not required. As long as backscattered light is being collected by the optical fibers and the signal can be read via the LabVIEW code, meaningful results can be obtained. The reason trapping of the beads is not required is because the Power Spectrum Analysis Method described in Section 3.1 measures the thermal excitation of the Brownian motion of the bead inside the optical trap. Just by exciting the bead and its motion with the light from the fiber tips, meaningful data can be collected, and mechanical stiffness of the brain can be calibrated.

- D) Turn off all components of the system and properly dispose of the used brain sample after experimentation.

IV. Calibrating the Mechanical Stiffness of the Brain Sample

Once data has been collected via the LabVIEW program, further processing must be conducted to calibrate the mechanical stiffness of the brain sample. This step focuses on this post-processing methodology and program used to carry out the calibration.

- A) Using the MATLAB code described in Section 3.3 (Labcode.m), import the saved data file that was produced during experimentation and that was written by the LabVIEW code. Running this code saves the collected data as a .dat file, allowing for another MATLAB code (also discussed in Section 3.3 - psfitting_real_lin5.m) to further process it. Place the .dat file into the same folder as the psfitting_real_lin5.m code.
- B) Open the psfitting_real_lin5.m MATLAB code and input parameters discussed in Section 3.3; run the code. A dialog box should appear, allowing the user to select the .dat file that was created with the previous MATLAB code. Upon selecting this .dat file, the data will be processed, and a Lorentzian fit of the data will be generated. Important experimental parameters such as the diffusion coefficient, spring constant, and corner frequency will be calculated with this code which can be then plugged into equations 3-7 and 3-8 to solve for the elastic and shear modulus of the brain sample.